Geothermics 136 (2026) 103589

Contents lists available at ScienceDirect

Geothermics

journal homepage: www.elsevier.com/locate/geothermics

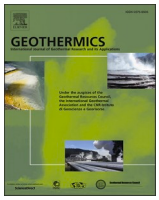

Improving borehole fracture characterization using oriented sidewall cores for geothermal assessment – an example in central New York State USA

Sean A. Fulcher [a,*], Teresa E. Jordan [a], Stephen E. Laubach [b], Sara J. Elliott [b], Valeria Nogales Herrera [c]

[a] Earth & Atmospheric Sciences, Cornell University, Ithaca NY 14853, USA
[b] Bureau of Economic Geology, Jackson School of Geosciences, The University of Texas at Austin, Austin, TX 78713, USA
[c] Delft University of Technology, Delft, CN 2628, the Netherlands

ARTICLE INFO

Keywords:
Fracture
Geothermal
Deep-direct use
Porosity
Sandstone
Scaling
Acoustic survey
Basement
Sidewall cores

ABSTRACT

In New York State and Pennsylvania, USA, Precambrian metamorphic and intrusive rocks and Cambrian to Lower Ordovician sedimentary rocks are reservoir targets for deep direct-use geothermal development. Evaluation of natural fractures and structures in the potential reservoir units at the Cornell University Borehole Observatory site was conducted through cross-scale evaluation of oriented sidewall cores, borehole image (BHI), and far-field acoustic survey data. Oriented sidewall cores in the basement complex (Cayuta Formation) reveal metasediments containing foliations, lineations, mineral-filled fractures, and breccia intervals. Basement sidewall core fracture data aid identification of fractures in BHI surveys riddled with borehole breakouts. In contrast, sidewall and image log data for the Cambrian-Ordovician sedimentary section show that open fractures are present and allow orientation and abundance to be estimated. At various depths sandstone and dolostone sidewall cores contain quartz-filled or carbonate-filled bed-normal and -parallel microfractures. Four subvertical microfracture sets, formed sequentially, strike NW-SE (F1), NE-SW (F2), N-S (F3), and WSW-ENE (F4). Microfracture set orientations F1, F2, and F4 match interpretations of acoustic fracture anomalies (open fractures) located tens of meters from the wellbore. In the uppermost Galway Formation sandstone, common microfracture apertures are 0.001 to 0.01 mm. The widest microfractures transition to quartz-lined and bridged open macrofractures. An open vertical macrofracture in Galway sandstone is observed in BHI surveys and a sidewall core, effectively ground-truthing the F4 fracture set. Based on comparison of core fractures with borehole image survey features, differentiation of natural from drilling-induced fractures reveals three sedimentary rock zones of elevated natural fracture frequency.

1. Introduction

Geothermal heat extraction from low porosity and permeability rocks depends on the effectiveness of fluid-rock heat exchange in natural or induced fracture systems (Moska et al., 2021; Liu et al., 2024). Efficient geothermal heat exchange is dependent on the permeability and surface area of preexisting natural or, for the case of an Enhanced Geothermal System (EGS), induced fractures (e.g. Ghassemi, 2012; Gee et al., 2021; Rangel-Jurado et al., 2023). A fundamental challenge for EGS development is cost-effective assessment of site-specific natural fracture attributes, as preexisting natural fractures affect reservoir stimulation and hydraulic connectivity (e.g., Pyrak-Nolte et al., 2015; Moska et al., 2021; Cao et al., 2022; Jin et al., 2024). Measurement of reservoir fracture attributes are commonly limited by small sample volumes and the non-optimal orientation of typical vertical wellbores relative to steep fracture dips, which are the most common fracture orientation in nearly flat-lying sedimentary rocks (e.g., Laubach et al., 2019). Identifying the presence and attributes of natural fractures and host rock is key for advancing the Cornell University Earth Source Heat (ESH) project.

The ESH project is a multiphase feasibility assessment of deep direct-use (DDU) geothermal energy for a district heating system capable of meeting the annual 240,000 MWt-hrs/yr space heating demand of the Cornell Ithaca campus (Jordan et al., 2016; Jordan et al., 2020). The ESH Well No. 1, also called the Cornell University Borehole Observatory (CUBO), is a 3 km deep geothermal research borehole intended to

* Corresponding author.
E-mail address: saf255@cornell.edu (S.A. Fulcher).

https://doi.org/10.1016/j.geothermics.2025.103589
Received 12 June 2025; Received in revised form 12 December 2025; Accepted 19 December 2025
Available online 20 January 2026

identify reservoir targets in the Corning-Ithaca Geothermal Play (CIGP) (Figs. 1, 2, 3) (Jordan et al., 2020). Early interpretation of Formation Microresistivity Image (FMI) and Ultrasonic Borehole Image (UBI) surveys from CUBO suggest moderately SE dipping fractures are present in some intervals while acoustic log interpretations show subvertical fractures occur 2-60 m away from the borehole at various depths (Fig. 4a,b) (Fulcher et al., 2023). Fractures in basement borehole images have complex patterns obscured by borehole breakouts and show variable orientations in either borehole image (BHI) surveys or the acoustic fracture survey (Fig. 4c,d) (Fulcher et al., 2023). Conflicting and incomplete fracture set data from the CUBO borehole image and acoustic surveys complicate reservoir assessment and development.

A common method to improve reservoir fracture characterization is integrating core, image logs, and/or acoustic surveys to bridge spatial data gaps and verify natural fractures. However, cross-referencing large-diameter core (c. 10 cm) and BHI surveys can only identify fractures which fully penetrate the well and may under-sample large fractures (macrofractures) (Nelson, 1982; Fernandez-Ibanez et al., 2018; Wennberg et al., 2023; Gale et al., 2023). Cores intercepting borehole fractures allow key attributes like kinematic aperture size, mineral fill, and porosity to be documented and for natural fractures to be distinguished from drilling-induced. BHI surveys commonly interrogate larger areas as they extend over greater borehole lengths than large diameter core intervals. BHI survey images display structural features as linear or planar resistivity contrasts or acoustic impedances. These features are interpreted as open or filled fractures, bedding planes, or other structural or textural features. Distinguishing between natural and drilling-induced fractures in BHI surveys is problematic without direct core evidence (Barton and Zoback, 2002; Chatterjee and Mukherjee, 2023; Gale et al., 2023). Acoustic borehole fracture surveys may reveal the depth and positions of large, open fractures, potentially at the borehole surface or at distances of tens of meters away from the wellbore (Morris et al., 1964; Hsu et al., 1987; Bolshakov et al., 2011; Bennett, 2019; Hati et al., 2021). The quality of acoustic far field fracture data depends on low borehole rugosity and homogeneous fluid composition (Kimball and Endo, 1998; Hornby et al., 1992). Consequently, without expensive large diameter core to verify fracture observations, BHI and acoustic survey observations are commonly incomplete or ambiguous.

To address fracture characterization issues in the CUBO well, we used oriented sidewall cores drilled from the CUBO open borehole face to identify natural macro- and microfracture populations, infer fracture orientation patterns, and document average fracture spacing. Microfractures are fractures with apertures ranging from 0.001 to 0.1 mm, requiring microscopy to detect (Anders et al., 2014). Analyzing microfracture populations allows some natural fracture attributes to be measured or inferred even in the absence of large fractures (Laubach et al., 2000; Hooker et al., 2009). For rocks having both micro- and macrofractures, microfracture sets can provide insights in brittle behaving and chemically resistant materials such as sandstones (Laubach, 1997; Hooker et al., 2014) and some crystalline basement rocks (Holdsworth et al., 2020). Wellbore microfractures sampled by sidewall cores can provide valuable fracture information about the number of sets, orientation, sequence, type of mineral fill on a 50 mm length scale (Laubach and Doherty, 1999; Laubach and Gale, 2006; Gomez et al., 2003; Gomez and Laubach, 2006; Gale and Gomez, 2007).

Some microfracture attributes such as the presence of open pore space and degree of mineral infill differ systematically from those of larger fractures. Microfractures tend to be sealed with mineral deposits. However, empirical evidence shows that above a specific kinematic aperture size, defined as the emergent threshold (Laubach, 2003),

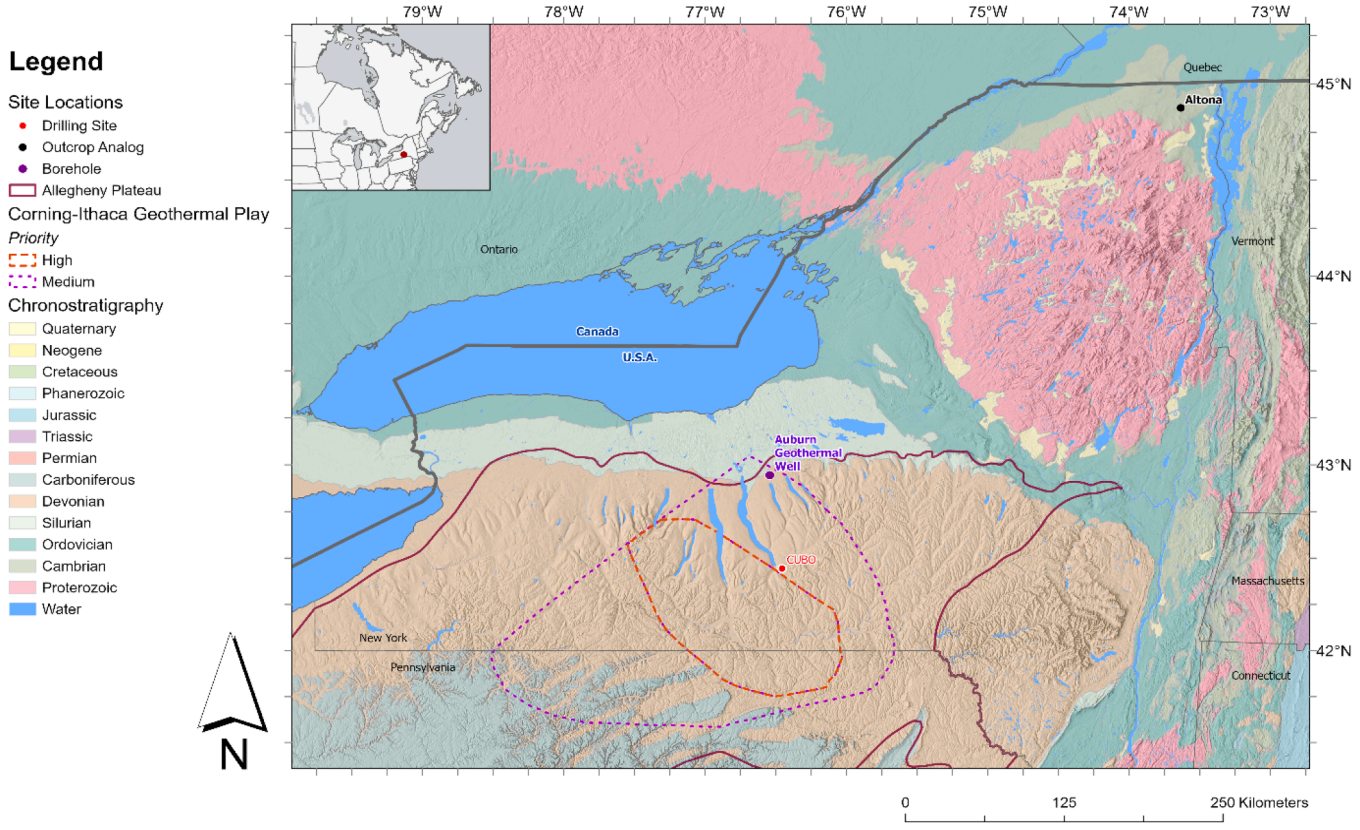

Fig. 1. Chronostratigraphic map of New York State compiled from USGS SGMC data (Horton et al., 2017), Ontario Geological Survey data (Ontario Geological Survey, 2024), and Ministère des Ressources naturelles et des Forêts (Ministère des Ressources naturelles et des Forêts, 2024). Locations shown of the CUBO site and two analog sites, the Auburn geothermal well and Potsdam Group at Altona, NY. Boundaries of priority zones of the Corning-Ithaca Geothermal Play (red dashed line, purple dotted line) show interpreted spatial extent of favorable conditions.

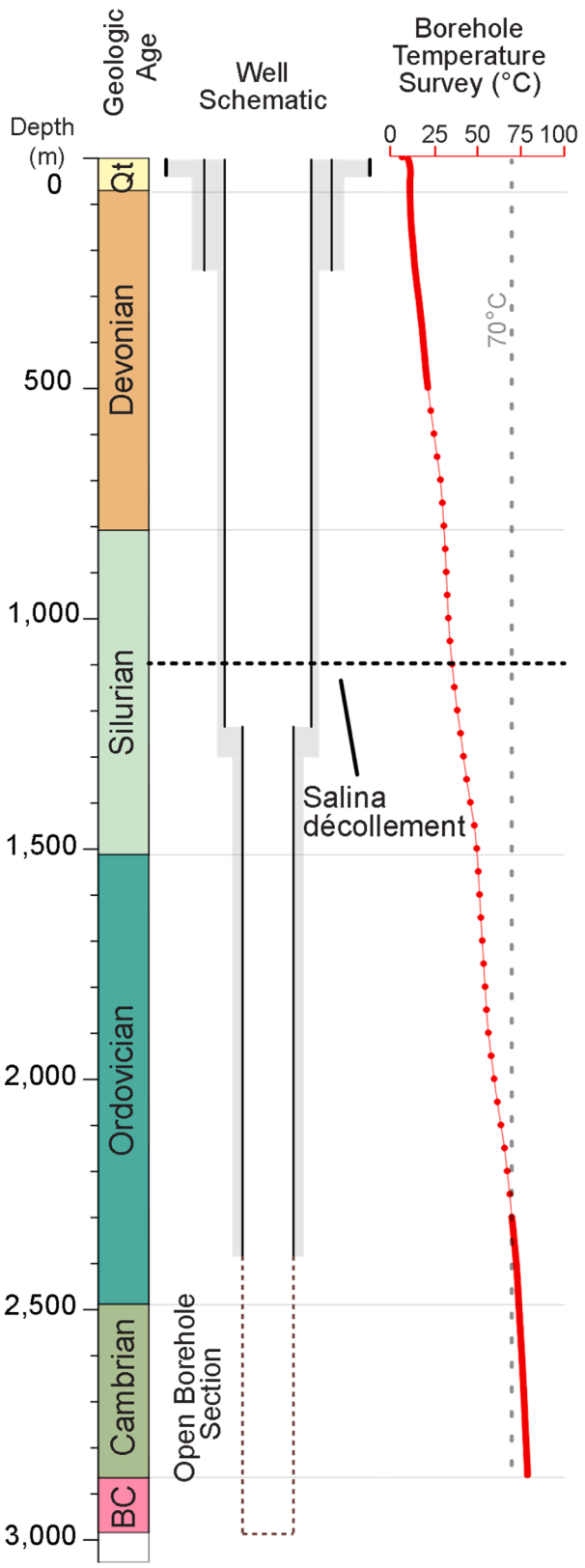

Fig. 2. Stratigraphic column of units intercepted by CUBO from Quaternary (Qt) to the basement complex (BC), with well casing diagram that shows the open borehole section and borehole equilibrium temperature survey from Fulton et al. (2024). The DDU project threshold of 70°C is also shown (gray dashed line).

fractures become open. Fracture mineral infills such as quartz in sandstone accumulate under sedimentary basin conditions governed primarily by thermal exposure (Lander and Laubach, 2015).

Here we show that basement sidewall cores document metamorphic fabrics and confirm polyphase deformation in the newly defined Cayuta Formation (Valentino et al., 2024). Within the basement, we found no simple pattern of fracture orientations and defined no fracture sets. Some fractures have attributes suggesting they may be post metamorphic, but these are filled with a variety of minerals. Basement sidewall core observations aid interpretation of BHI surveys allowing identification of breccia zones.

For Cambrian to Lower Ordovician Potsdam and Beekmantown strata, we show that lithologic data obtained from the dolostone and sandstone cores are consistent with regional rock properties as well as regional porosity and permeability findings (Kolkas and Friedman, 1999, 2007). Oriented sidewall core and wireline log observations allow cross-scale interpretation of fractures useful for geothermal development planning, complementing fracture interpretations in the Auburn Geothermal Well (Lynch and Castor, 1983; Hickman et al., 1985; Plumb and Hickman, 1985). Sidewall cores in Cambrian to Lower Ordovician sandstones reveal hundreds of quartz-filled microfractures (0.001 to 0.1 mm width) and two open and quartz-lined macrofractures (width 0.11 to 0.265 mm). Microfracture analysis defines the orientation, relative timing, and abundance of five fracture sets (F0 through F4) and suggests fractures in Beekmantown and Potsdam Groups form densely populated networks of small partly opened fractures hosting quartz and carbonate cements. Comparison of sidewall core fracture data with BHI surveys shows that many low resistivity fractures are likely drilling-induced fractures and leads to identification of three zones of higher natural fracture frequency.

Comparison of subsurface fracture attributes with overlying Devonian outcrop fracture data indicates systematic brittle deformation persists from the surface to a depth of 2,860 m, inclusive of Cambrian to Lower Ordovician units of the Allegheny Plateau. Comparison of subsurface fracture data to a sandstone outcrop analog about 350 km in distantance shows similar set orientation, sequence, and mineral fill.

2. Geologic setting

The CUBO site is located within the northern area of the Allegheny Plateau geomorphic province of the Appalachian Basin (Fig. 1), where igneous/metamorphic basement rocks are overlain by Cambrian, Silurian, and Devonian strata (Figs. 2 and 3) (Isachsen et al., 2000). Surface exposures of basement rocks and the lower Paleozoic reservoir targets are distant (>180 km or more), around the margins of the Adirondack dome (Fig. 1).

The ESH DDU geothermal project lies within the CIGP, a 24,000 square kilometer play area of the northern Appalachian Basin (Allegheny Plateau) having an average continental geothermal gradient (Blackwell et al., 2011) (i.e., 25.1°C/km CUBO borehole gradient) (Fulton et al., 2024) and a low seismic risk profile (Figs. 1 and 2) (Jordan et al., 2016). Interpolated bottomhole temperature data indicate viable geothermal heat of 70-90°C in the Ithaca area at depths of 2,500 to 3,000 m (Smith, 2019). Projected depths of those viable DDU temperatures are within the basement complex and Cambrian to Lower Ordovician stratigraphic units (Tester et al., 2023).

The basement intercepted by the CUBO borehole contains low-grade metasedimentary rocks defined as the Precambrian Cayuta Formation (Valentino et al., 2024). Cambro-Ordovician targets include Potsdam Group, Galway Formation, Little Falls Formation, and Tribes Hill Formation (Tester et al., 2023), which range among quartz-rich marine sandstones, dolomitic sandstones, and mixed carbonate rocks. The Cambrian to lowermost Ordovician section represents a 700 m thick target ranging in age from 477 to 510 Ma (Fig. 3). The stratigraphy at the CUBO site is described in Appendix A. Gas exploration and production data indicate basement rocks and lower Paleozoic sedimentary rocks

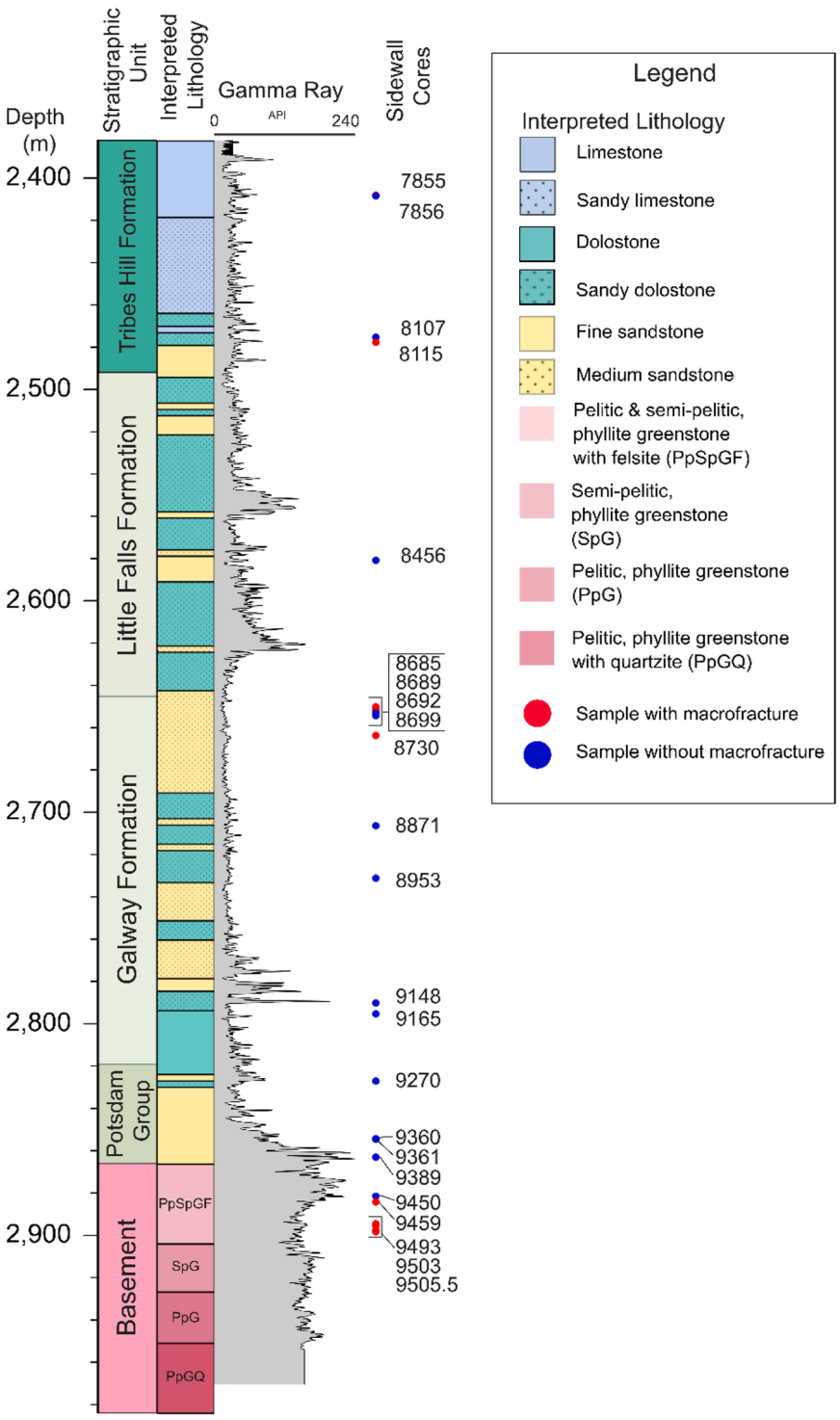

Fig. 3. Stratigraphic column of open borehole section with gamma ray log and locations of sidewall cores.

have low overall porosity (0 to ≤ 5%) and low matrix permeability (0.001 to 0.038 mD) (Kolkas and Friedman, 2007; Smith et al., 2010; Al Aswad, 2019).

The Cambrian to lowermost Ordovician of the CUBO open borehole section represents a 490 m thick target ranging in age from 477 to 510 Ma (Fig. 3). For Cambrian and Lower Ordovician strata, preserved thicknesses are compatible with gradual early Paleozoic burial in platform to passive margin settings (Smith et al., 2010), followed by later Paleozoic burial in a foreland basin. The foreland was affected by Taconic (~455-442 Ma), Acadian (~423-385 Ma), Neo-Acadian (366-350 Ma), Late Pennsylvanian (300-290 Ma), and Alleghenian (~280-260 Ma) shortening related to orogenic belts to the south and east (Robinson et al., 1998). The CUBO site is over 150 km north of the Allegheny structural front, yet low amplitude northeast-trending open folds exist near the CUBO site (Fig. 5) (Wedel, 1932; Engelder and Geiser, 1980). Here folds are considered detached below the Upper Silurian Salina evaporites at the Salina décollement (Scott, 1986; Mount, 2014). Consequently, structural features in the sub-décollement Potsdam and Galway Formation rocks may differ from those at shallower levels.

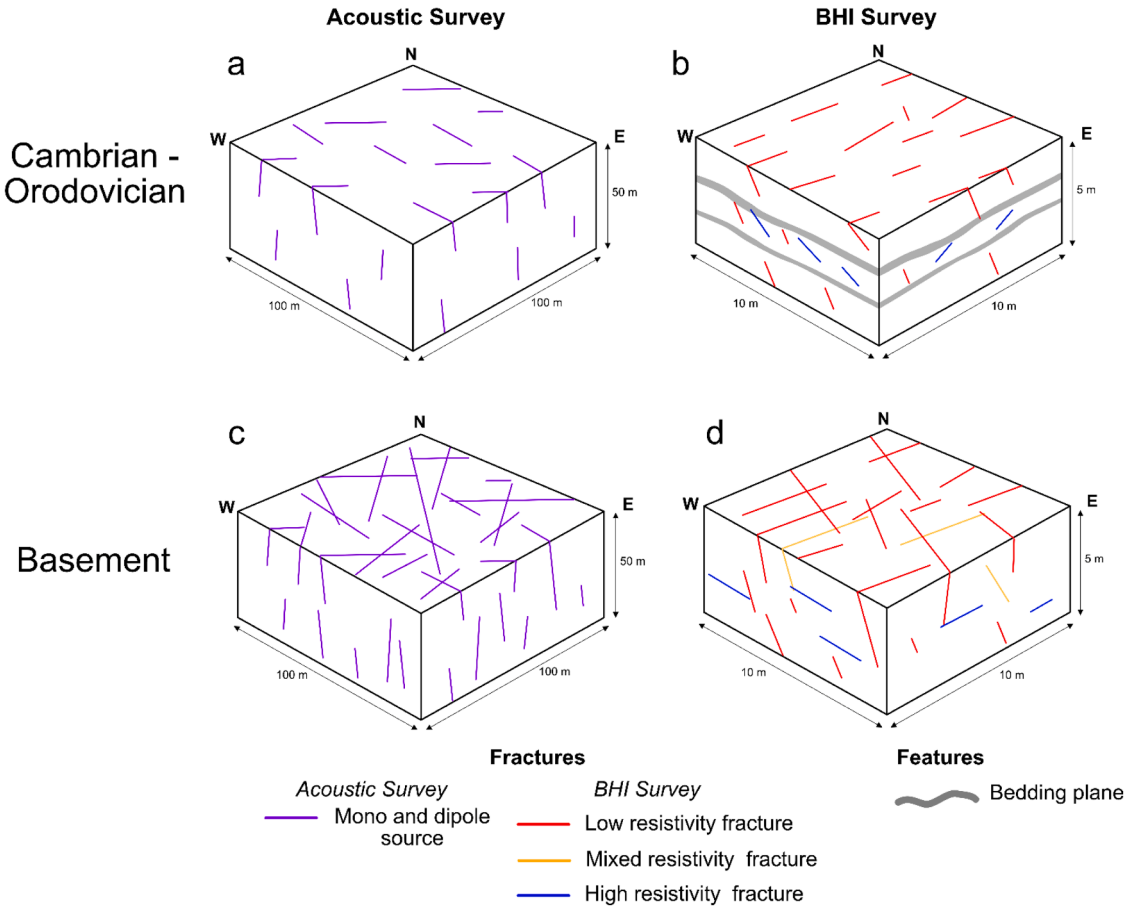

Fig. 4. Block diagrams of general fracture interpretations in the CUBO open borehole section based on Fulcher et al. (2023). a) Diagram of interpreted acoustic far-field fractures in the Cambrian-Ordovician section showing NW and E striking subvertical fractures. b) Interpreted fractures from BHI surveys in Cambrian-Ordovician section showing predominantly NE striking moderately dipping fractures. c) Far-field fracture interpretation of basement complex from acoustic fracture survey showing subvertical fractures with variable strike orientations. d) Fracture interpretation from BHI surveys in basement section of CUBO showing mainly subvertical and subhorizontal fractures.

Within the Allegheny Plateau, evidence of thermal exposure from maturity indicators or thermochronology is lacking for the Potsdam and Beekmantown Groups, yet there are sparse data for the overlying Ordovician units and shallow Devonian strata. In counties adjacent to CUBO, borehole samples of Ordovician strata overlying the Tribes Hill Formation have conodont alteration indices of 4.0-5.0, compatible with maximum temperatures of 190-300°C. For the Potsdam and Beekmantown Group targets, several hundred meters below the Ordovician conodont data horizons, temperatures likely reached 200-300°C (Repetski et al., 2008). Thus, burial and thermal history are uncertain but likely included deep burial and temperatures suitable for rapid quartz accumulation (>80°C; Taylor et al., 2022).

Allegheny Plateau regional fracture patterns for Devonian outcrops have been extensively studied (e.g., Engelder and Geiser, 1979, 1980; Engelder 1985), including near the CUBO site (Fig. 5). Around the margins of the Adirondacks, fractures are common in Potsdam Group outcrops (Engelder and Sbar, 1977) and although some likely result from near-surface processes (Li and Ji, 2021) some fractures have been described as possible subsurface reservoir analogs at localities about 350 km from the CUBO site (Fig. 1) (Forstner et al., 2024; Elliott et al., 2025). Near Ithaca, the current stress regime is between strike-slip and thrust faulting, with a northeast-southwest oriented maximum horizontal stress (SHmax) (Heidbach et al., 2019; Pinilla et al., 2023).

3. Methods and materials

Sidewall core sampling was undertaken to provide lithology, structural, and geomechanical data from target EGS reservoir formations. Previously, sidewall cores in hydrocarbon reservoirs have yielded accurate rock type (Hansen and Enderlin, 1991; Rourke and Torne, 2011; Neal et al., 2023), porosity and permeability (Koepf and Granberry, 1961) information and, for oriented cores, fracture orientations (Laubach et al., 2002) and kinematic aperture size distributions (size scaling) (Laubach and Gale, 2006).

3.1. Sidewall core sampling, orientation, and logging

Sidewall core sampling involves collecting small cores from the wellbore wall with a wireline-operated drill and sample retrieval mechanism that can collect tens to several dozens of cores from specific depths (Saucier and Sincock, 2023). Sample depths were selected after reviewing the BHI surveys to target specific lithological and structural features (e.g., textural changes, bedforms, and fractures). From the ESH No.1 open borehole, twenty-five XL-size (38.1 × 63.5 mm) cores were collected in a single wireline run using the Schlumberger (SLB) XL-Rock tool that sampled basement, Cambrian, and Ordovician units (Fig. 3, Table 1). Core depths range from 2,403 to 2,897 m (Fig. 3).

Sidewall cores are an unconventional way to collect fracture data and this application is only possible if cores are oriented. Orientation is not provided in standard sidewall core retrieval. Sidewall core orientation in our study followed a method described by Laubach and Doherty (1999) and Volonté et al. (2023), with improvements per our experience (Fig. 6) (Appendix B2).

The key unknowns are the core top direction and the azimuth.

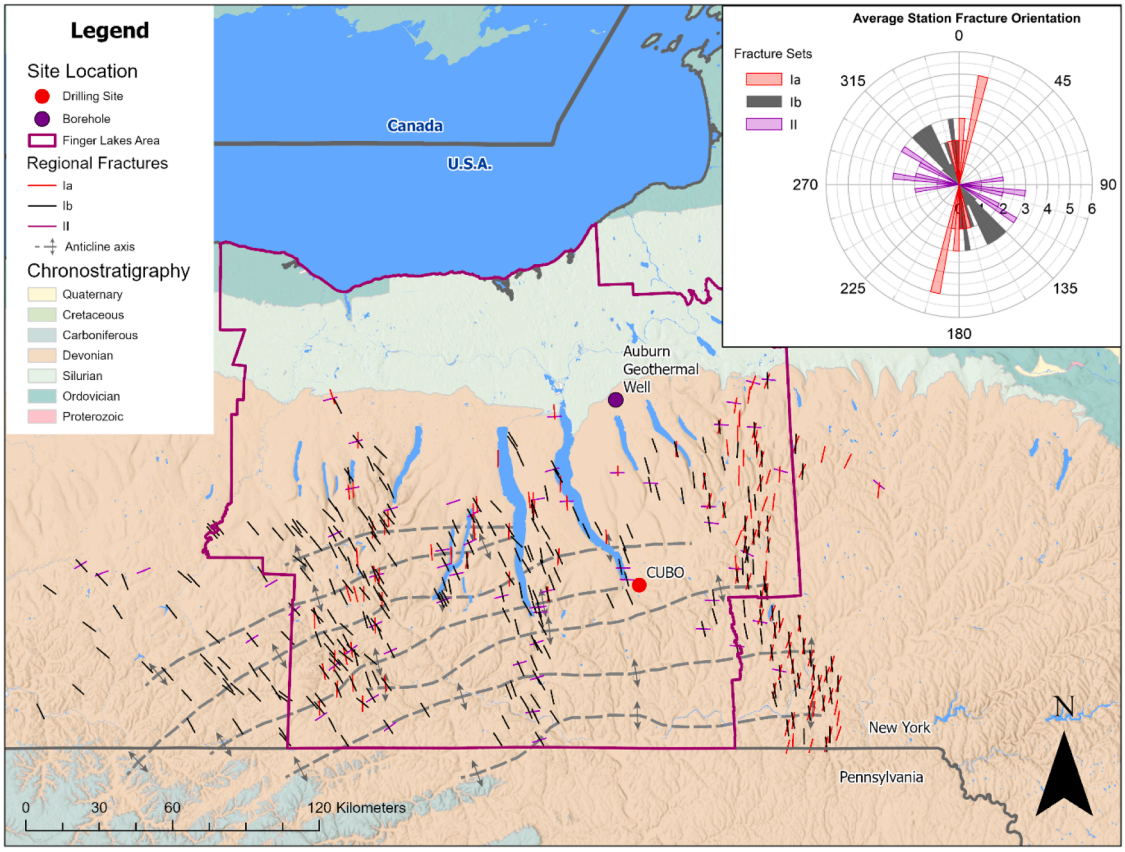

Fig. 5. Digital elevation model of north-central Allegheny Plateau with geologic structures observed at the surface: regional anticlinal axes after Wedel (1932), and sets Ia, Ib, and II fracture strikes after Engelder and Geiser (1980). Inset rose-diagram shows fracture set orientations in the Finger Lakes area from Engelder and Geiser (1980).

Table 1
Table of core depths, lithology, orientation, and occurrence of microfractures.

Sample	Depth (m)	Formation	Subunit	Lithology	Core Recovery (%)	Drilled Azimuth	Micro Fractures
7885	2,403.3	Tribes Hill Formation	-	Dolostone	107%	131.3°	Yes
7886	2,403.7	Tribes Hill Formation	-	Dolostone	107%	121.4°	Yes
8107	2,471.0	Tribes Hill Formation	-	Dolostone	83%	-	Yes
8115	2,473.5	Tribes Hill Formation	-	Dolostone	107%	39.2°	
8456	2,577.4	Little Falls Formation	-	Quartz arenite	101%	-	
8685	2,647.9	Galway Formation	Rose Run	Quartz arenite	99%	119.4°	Yes
8689	2,651.8	Galway Formation	Rose Run	Quartz arenite	72%	4.3°	Yes
8692	2,650.0	Galway Formation	Rose Run	Quartz arenite	76%	123.33°	Yes
8695	2,650.2	Galway Formation	Rose Run	Quartz arenite	104%	355.1°	
8699	2,652.1	Galway Formation	Rose Run	Quartz arenite	91%	129.7°	Yes
8730	2,660.9	Galway Formation	Yellowjacket	Dolostone	106%	134.4°	Yes
8871	2,703.9	Galway Formation	Yellowjacket	Dolostone	106%	299.5°	
8953	2,728.9	Galway Formation	Yellowjacket	Dolostone	98%	-	
9148	2,788.3	Galway Formation	M3	Dolostone	102%	129.7°	Yes
9165	2,793.5	Galway Formation	M3	Dolostone	99%	114.2°	
9270	2,826.2	Potsdam Group	Ausable Formation	Arkose	98%	-	Yes
9360	2,853.7	Potsdam Group	Ausable Formation	Subarkose	104%	86.8°	Yes
9361	2,854.0	Potsdam Group	Ausable Formation	Arkose	104%	82.1°	Yes
9389	2,862.3	Potsdam Group	Ausable Formation	Conglomerate	66%	93.2°	
9450	2,880.9	Unconformity		Metasediment	87%	126.5°	Yes
9459	2,883.1	Cayuta Formation	-	Phyllite	98%	166.0°	Yes
9493	2,893.5	Cayuta Formation	-	Phyllite	80%	153.3°	Yes
9496	2,894.4	Cayuta Formation	-	Phyllite	83%	148.1°	Yes
9503	2,896.5	Cayuta Formation	-	Phyllite	8%	136.1°	Yes
9505.5	2,897.3	Cayuta Formation	-	Phyllite	80%	262.8°	Yes

Although sedimentary structures like cross beds give top direction, such features are rarely interpretable in small cores (Laubach and Doherty, 1999). We identify core tops using features in the cores and on core ends created during drilling and core extraction (Figs. 6b,c,d,e,f). The azimuth of cores is ascertained by imaging the borehole wall with a BHI survey (e.g., FMI or UBI log) after the sidewall core run, noting the location of sidewall core holes visible in the wellbore wall (Fig. 7c). Because the images are oriented, the location of the core borings

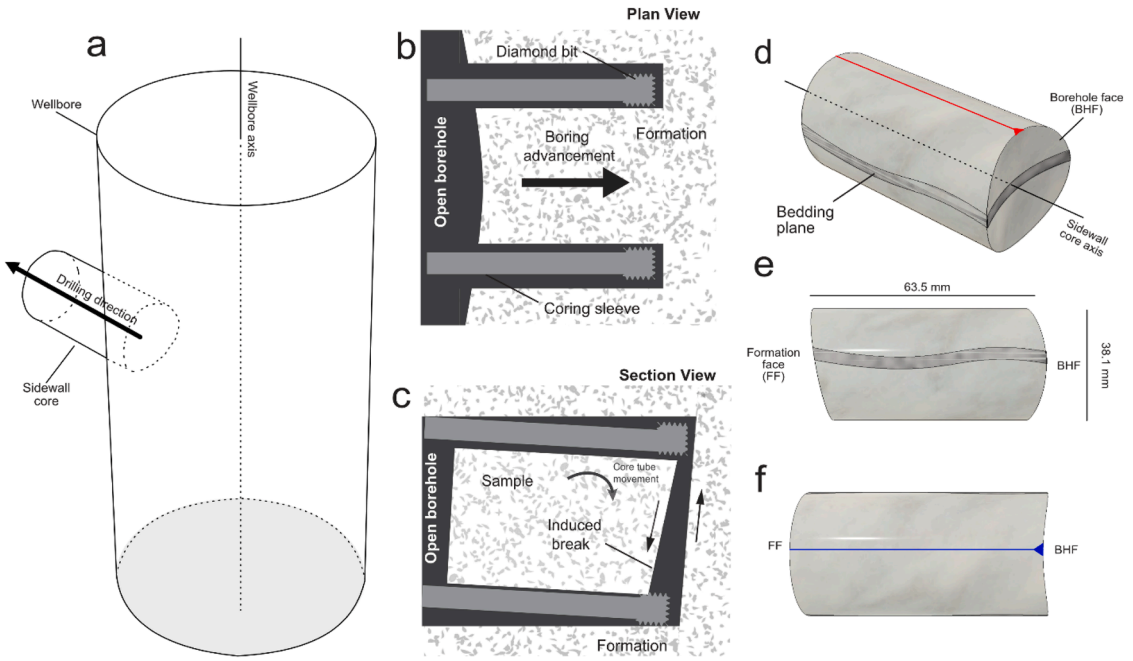

Fig. 6. Sidewall core orientation terminology and sampling procedure. a) Sidewall core location in wellbore showing drilling direction. (b) Planview of sidewall core drilling showing concave borehole face (BHF). (c) Cross-sectional diagram showing break of sample from formation induced by rotating coring sleeve downward after maximum drilling length is achieved. (d) Illustration of sidewall core with a bedding plane, top orientation line (red) and the curved BHF. (e) Schematic of sidewall core viewed horizontally depicting nominal XL sidewall core dimensions and angled formation face (FF). (f) Bottom view schematic of sidewall core showing concave BHF and bottom orientation line (blue).

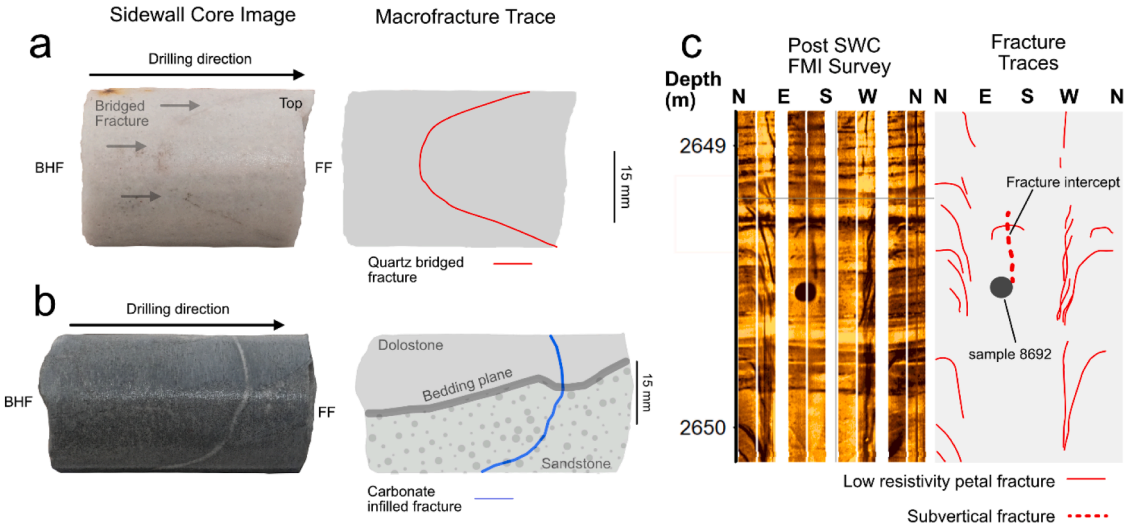

Fig. 7. Images of sidewall core samples that intercept a macroscopic fracture and the location in FMI survey of corresponding core. a) Side view of sample 8692 of quartz bridged macrofracture; left photo, right interpretation. b) Side view of sample 8730 subvertical macroscopic fracture with carbonate infill crosscutting bedding plane; left photo, right interpretation. c) FMI survey image (left) showing location of sample 8692 boring location and traces of linear features (right).

provides evidence of core azimuth. In Appendix B we describe how these azimuth values can be obtained with maximum precision.

Following sidewall core sampling, all cores were systematically photographed and logged to document rock quality dimension, recovery, competency, lithology, and structures using standard methods (Majoribanks, 2002). Fracture width measurement used a logarithmically graduated comparator (Ortega et al., 2006). We measured kinematic aperture and described any fracture porosity.

3.2. *Laboratory testing*

Oriented and logged sidewall core samples were analyzed for porosity, permeability, and internal structure by the Repsol Technology Laboratory in Madrid, Spain. Porosity and permeability analysis was completed using helium pycnometry. Micro x-ray computed tomography (MXCT) was completed at a 19 μm resolution. MXCT imaging of each sidewall core provided arrays of 2D images which were digitally interpolated to form 3D density voxel models using Dragonfly software. Rendered 3D density voxel models underwent fracture and feature analysis, including determination of fracture orientation measurements

and feature dimensions using digital measurement tools in Dragonfly software. Porosity was calculated from 3D density voxel models by creating pore space models for each sample using Dragonfly software.

3.3. Petrographic and microfracture analysis

Eleven cores containing fractures identified on MXCT images were selected for further analysis (Table 2). For basement rocks, four sidewall core samples were examined with transmitted light (TL) microscopy with sample 9459 undergoing scanning electron microscopy (SEM) analysis, focusing on lithology, fabric, and fracture morphologies.

Seven sandstones from Potsdam Group and Galway Formation sidewall samples were analyzed using TL microscopy while three samples of this suite were further analyzed using SEM and cathodoluminescence imaging (SEM-CL) (Table 2). SEM and SEM-CL analysis followed procedures specified in Appendix B2.3 to document host rock composition and textures, and also fracture locations, dimensions, and mineralization. Microfracture populations in thin sections were mapped in long, narrow image mosaics (1 × 30 mm) collected using multiple rows of panchromatic SEM-CL images (grayscale intensities) with magnifications ranging from 175× to 250× . Four mosaics are oriented bed-parallel and two are bed-perpendicular (Table 2). Quartz luminescence intensities and colors reflect trace chemicals and mineral lattice defects (e.g., Götze et al., 2001) and were used to document and sequence infill textures. Microfractures were classified by their shapes and crosscutting relations to grains and cement (Laubach, 1997). On bed-parallel scanlines, data for steeply dipping microfracture strikes, positions, apertures, and lengths were used for spatial arrangement analysis (Marrett et al., 2018) and aperture size-scaling inventory (Gomez and Laubach, 2006; Ortega et al., 2006).

3.4. Well surveys

Wireline logs including gamma ray, neutron porosity, density, borehole imaging, and acoustic were acquired by SLB wireline services in the open borehole section (2,377 to 2,984 m) to various depths (Fig. 3). From the log suite, we focus on analysis of BHI surveys and the acoustic fracture survey (Sonic Scanner). Additional details of the acoustic survey methods are provided in Appendix C3.

3.4.1. Borehole image (BHI) surveys and analysis

Four BHI surveys were completed: an acoustic televiewer (UBI) and three microresistivity image logs (FMI). The single UBI survey, using acoustic wave forms, provided 100% circumferential borehole image coverage. UBI distinguishes rock fabrics, fractures, and borehole wall rugosity as acoustic wave velocity/amplitude contrasts. The FMI surveys used a four-pad and four-flap setup with 192 button sensors for microresistivity image acquisition, covering approximately 80% of the open borehole circumference. FMI surveys were completed prior to and after sidewall coring and other formation tests to distinguish fractures, fabrics, and features at or near the borehole wall (<3 cm depth) as electrical resistivity contrasts.

BHI survey data files were provided by SLB in DLIS format and processed using AspenTech Geolog™ software. Data processing of FMI and UBI survey data followed a standard tiered analysis process consisting of speed correction, azimuthal referencing, and static and dynamic image rendering of resistivity data and sonic wave forms, respectively. FMI survey data processing required additional equalization of generated images prior to creating static and dynamic images. Equalization processing alters the generated speed-corrected static images by adjusting the standard deviation and mean of each column (resistivity button) based on a window size thereby enhancing the computed borehole image for structural feature analysis. This processing is standard for acquiring meaningful borehole image data for interpretation.

All four image surveys were analyzed for changes resulting from surveying and sidewall coring. Images generated from the UBI survey have overall low resolution and were used for comparison where applicable. FMI surveys have the most consistent high-quality images and were used for fracture classification.

Fractures identified in FMI surveys are categorized into three types based on resistivity signatures: low resistivity, high resistivity, and mixed-resistivity. Fractures traces were classified using an approach based on Fernandez-Ibanez et al. (2018) to categorize continuity, geometry, and dip angle. Fracture trace continuities were categorized based on the extent of borehole wall coverage in four categories: I (0 to 25%), II (25< to ≤50%), III (50< to ≤75%), IV (>75%). Trace geometries were also classified as having a partial, single, or multi sinusoidal (e.g. ski-sloped) geometry. Dip angles were measured and compared to sedimentary features, and dip angles less than 30° were flagged for

Table 2
Attributes of sandstone and basement sidewall cores referred to in analysis. Scanline attributes given for sandstones whose microfractures are fully documented.

Sample	Depth (m)	Formation	Subunit	Lithology	Thin Sections	Scanlines	Scanline Azimuth	Scanline Length (mm)	Macroscopic Natural Fractures
8685	2,647.9	Galway Formation	Rose Run	Quartz arenite	Bed Perpendicular	-	-	-	
8689	2,651.8	Galway Formation	Rose Run	Quartz arenite	Bed parallel	L1	4°	20.68	
						L2	94°	36.94	
					Bed perpendicular	L3	4°	11.90	
						L4	Vertical	37.70	
8692	2,650.0	Galway Formation	Rose Run	Quartz arenite	Bed parallel	L5	176°	25.64	Yes
						L6	123°	37.66	
8699	2,652.1	Galway Formation	Rose Run	Quartz arenite	Bed perpendicular	-	-	-	Yes
9270	2,826.2	Potsdam Group	Ausable Formation	Arkose	Bed perpendicular	-	-	-	
9360	2,853.7	Potsdam Group	Ausable Formation	Subarkose	Bed perpendicular	-	-	-	
9361	2,854.0	Potsdam Group	Ausable Formation	Arkose	Bed perpendicular	L7	82°	16.73	
						L8	Vertical	37.21	
9459	2,883.1	Cayuta Formation	-	Phyllite	Parallel to foliation	-	-	-	
9493	2,893.5	Cayuta Formation	-	Phyllite	Perpendicular to foliation	-	-	-	Yes
9496	2,894.4	Cayuta Formation	-	Phyllite	Perpendicular to foliation	-	-	-	Yes
9505.5	2,897.3	Cayuta Formation	-	Phyllite	Perpendicular to foliation	-	-	-	Yes

further review. These rules favor picking more continuous and steeper traces as fractures (Fernandez-Ibanez et al., 2018).

3.4.2. Acoustic survey

An acoustic fracture survey was conducted to identify far-field open fractures (reflectors) using oriented compression and shear wave analysis, also known as sonic imaging. Orientation and location of wave reflectors (true dip and azimuth) requires analysis of directionally acquired wave forms using 3D slowness time coherence (3D STC) of filtered arrival events from distal P-P, P-S, and S-S wave forms (Bennett, 2019). The coherence model assumes an elastic solid matrix and a viscous pore fluid as defined by Biot (1956a,b). Locations of far-field wave reflectors are determined by the reflection time and direction analysis using Alford rotation. Far-field wave analysis does not indicate lengths or apertures of features inferred from wave reflections. Signal-to-noise ratios are further improved using multi-shot techniques (repeated measurements) while traversing the borehole path.

For the CUBO acoustic fracture survey, the SLB Sonic Scanner tool was used to measure and orient reflected compression and shear wave velocities induced by monopole and dipole transmitters. The Sonic Scanner tool consisted of three monopole and two directional dipole transmitters spaced between an array of 13 onboard receiver stations composed of 8 circumferential hydrophones – resulting in a vertical survey resolution of 60 cm. Compression and shear wave data were processed by SLB using semblance processing (3D STC), SPI processing, and inversion techniques in Petrel software, which provided the orientations of structural discontinuities (e.g., fractures) as well as their radial distances and directions from the borehole. The quality of the acoustic analysis is diminished by multiple factors (Zhang et al., 2009; Kostek et al., 1998) including irregular borehole walls, deviations from a simple, uniform elastic solid, and complex fractures producing reflections. To assess the impacts of these effects on the quality of the reported fractures, raw and corrected shear velocities were compared and evaluated against tolerance criteria (Appendix C3).

4. Results

4.1. Sidewall core rock attributes

4.1.1. Basement rock attributes

Six basement sidewall core samples were collected in the upper portion of the basement complex from depths of 2,881 to 2,897 m, with core recoveries of 8 to 98% (Table 1). The shallowest basement sample is located 3 m below the Cambrian contact and is extensively altered and brecciated (Nogales Herrera, 2024) and is not further considered in this study. Basement sidewall cores are intermediate composition (SiO_2 ~ 52%) phyllites (Nogales, 2024) containing weak to moderate lineations and finely spaced foliation (Table 3). Transmitted light petrography of samples 9459 (2,883.1 m), 9493 (2,893.5 m), 9496 (2894.4 m) and 9505.5 (2,897.3 m) document fine-grained (50-300 μm) biotite, muscovite, chlorite, quartz, K-feldspar, and apatite in a spaced foliated matrix with 0.5-1 mm thick quartz domains (Figs. 8,9). An L1 lineation composed largely of 1 mm size biotite shows a rake and plunge of 107.6 and 60° in sample 9505.5 (Figs. 8,9). Pinitized 1-3 mm diameter porphyroblasts that pseudomorph a primary mineral are observed in samples 9459, 9493, and 9496 (Fig. 9). These pseudomorphs in samples 9493 and 9496 shows length orientation along inclined foliation planes. Inclusions of fine biotite in these pseudomorphed porphyroblasts are generally aligned subhorizontally and appear clustered in samples 9459 and 9496 (Fig. 9).

Basement sidewall core porosity ranges from 0.45 to 5.10 % (Table 3) while air permeability values were below 0.01 mD (0.002-0.009 mD) (Table 3). Open microfractures with 5-10 μm apertures occur in pinitized pseudomorphosed porphyroblasts of sidewall core 9496 and do not extend into the foliated matrix (Nogales Herrera, 2024). Porosity values provided by neutron porosity (NPHI) (Table 3) are between 12

Table 3
Host rock attributes from basement rock based on point count data (N; grain size; mineralogy; and fabric), laboratory tests (MXCT porosity, core porosity, permeability), and geophysical surveys (NPHI).

Sample	Depth (m)	Formation	Method	N	Grain Size (mm)	Major Minerals						Accessory Minerals			Fabric	Porosity			Permeability (air) mD
						Biotite	Muscovite	Quartz	k-feldspar	Chlorite	Pinite (pseudomorph)	Apatite	Zircon	Foliation	Lineation	NPHI[1]	MXCT Porosity	Core Porosity[2]	
9459	2,883.10	Cayuta Formation	Optical	325	0.05-1	35	28	22	2	5	5	2.5	0.5	mild	-	12%	1.68%	-	-
9493	2,893.47	Cayuta Formation	Optical	333	0.02-2	28.5	21.5	28	0.5	11	9	1	0.5	mild - spaced	L1	17.85%	0.003%	0.45%	0.001
9496	2,894.38	Cayuta Formation	Optical	367	0.05-3	28.0	25	25.5	1	10	7	3	0.5	mild - spaced	L1	15.25%	0.019%	5.10% 3.79%	0.006 0.009
9505.5	2,897.28	Cayuta Formation	Optical	310	0.05-1	31.0	27	26	2	12	-	1.5	0.5	mild	L1	14%	0.003%	1.18%	0.004

[1] Neutron porosity (NPHI) values are calculated from an initial limestone calibration from 6-inch intervals.
[2] Core porosity determined by whole core helium pycnometer testing by Repsol.

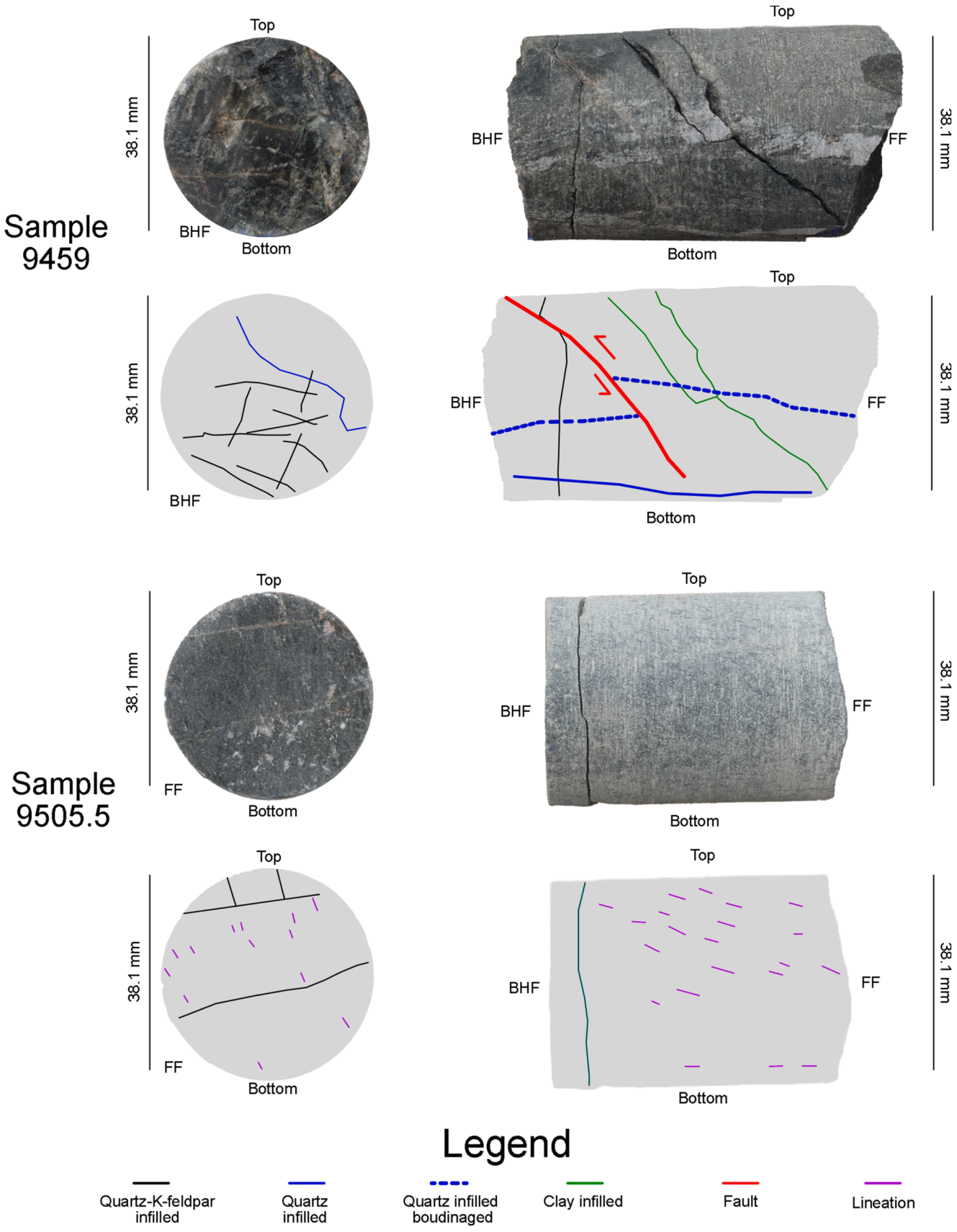

Fig. 8. Pairs of oriented photographs and illustrations of structural features of two basement sidewall core samples. For sidewall core 9459, the borehole fracture face (BFF) end is displayed. For core 9505.5, the fracture face (FF) is displayed. Core top and bottom orientations are indicated.

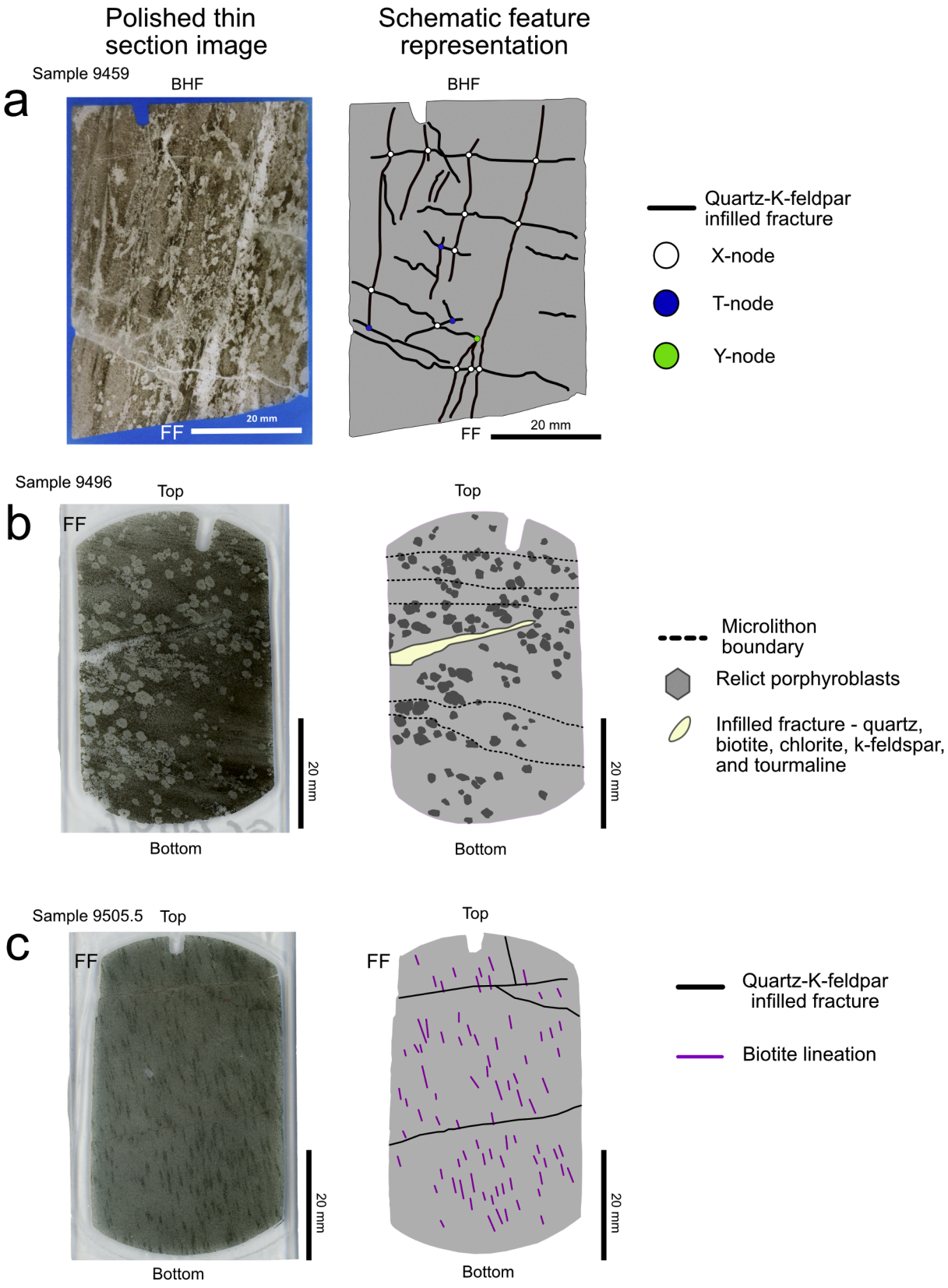

Fig. 9. Images and illustrations of lithologies and structural features from basement sidewall polished thin sections (PTS). Notched edges of samples indicate top of sidewall core. a) Brecciation textures (left) and fracture traces (right) from PTS that parallels the axis of core 9459. b) Oriented PTS image of sample 9496 showing quartz-dominated microlithons and porphyroblasts of pinite that pseudomorphs earlier coarse minerals. c) Oriented PTS of sample 9505.5 illustrating subvertical and subhorizontal quartz-K-feldspar infilled fractures overprinting biotite-rich lineations.

and 17.85%.

4.1.2. Cambrian-Ordovician rock attributes

Sidewall core composition from Cambrian to Lower Ordovician strata is generally sandstone or dolostone. Sandstone samples range in composition from quartz arenite to arkose and have sedimentary structures varying from massive to finely bedded. Seven sandstone sidewall cores containing fractures were examined using TL petrography – three sidewall cores are from the Potsdam Group and four are from the Galway Formation (Tables 2, 4). Three sidewall core samples from this suite were further examined by SEM techniques (Table 4). Sample depths range from 2,647.9 to 2,854 m (Table 4).

Core recoveries of Potsdam Group samples were high, ranging from 98% to 104% (Table 1). Potsdam Group sandstones are light to medium grey in color when dry, and are composed of moderately sorted, subangular to subrounded, 0.01 to 0.5 mm diameter detrital quartz and albite-microcline grains (Figs. 10 h, i) (Table 4). Thin (1 cm) dark planar beds contain higher K-feldspar and accessory mineral content (Fig. 10i). Detrital quartz content ranges from 60.1 to 70.2%, while the intergranular volume is between 11.5 to 12.3% (Table 4). Potassium feldspar content (2 - 28.6%) is significantly higher than in the Galway Formation samples. Interstitial clay mineral content, composed dominantly of fine grained dispersed illite, reaches 2.14 to 5.8% and is higher than in the Galway Formation (Table 4). Granular dolomite occurs sporadically as 5-30 μm subhedral grains (Table 4) (Figs. 10a,b,c).

Potsdam Group samples have quartz and minor dolomite cement (Table 4). Optically continuous quartz overgrowths and rinds are limited to larger grains. Dolomite cements are not common but more abundant in shallower Potsdam Group samples (9270 and 9360). A single generation of blocky quartz cement forms the predominant material infilling intergranular space in Potsdam Group samples (Fig. 10h). Potsdam Group core porosity, measured via helium pycnometry, ranged from 0.59% to 4.5%, and air permeability values varied between 0.004 to 0.032 mD (Table 4). Porosity provided by MXCT analysis are orders of magnitude lower than measured by NPHI and SEM methods (Table 4).

Galway Formation sandstones have core recoveries of 72% to 104% and have a light buff to white color when dry. Galway Formation sidewall cores are composed chiefly of well sorted, subrounded to well-rounded, 0.05 to 1 mm diameter detrital quartz grains (Figs. 10a,b,c, d,e,f,g) (Table 3). SEM point counts via energy-dispersive X-ray spectroscopy-(EDS) scanning measure a detrital quartz content ranging from 66.7 to 90% with a variable intergranular volume of 12.5% (sample 8685) to 28.8% (sample 8689) (Table 4). Granular dolomite (5-30 μm) containing anhedral minute pyrite is identified near pore spaces and between quartz grains. Accessory minerals are primarily fine grained illite (0.6 – 1.68%) occurring interstitially and as dispersed local grain coats (Figs. 10e,f).

In three Galway Formation samples, three types of quartz cements that formed sequentially are distinguishable by overlapping CL textures. The first forms 5 to 45 μm thick rinds around quartz grains (Figs. 10c,d, e). In the second, quartz cement forms small (5-10 μm) planar syntaxial growths adjacent to the grain rinds (Figs. 10c,d,e). The third quartz cement type occurs interstitially and as grain-bounding euhedral overgrowths impinging on pore spaces (Figs. 10e,f). Pore spaces are irregularly shaped and occur within interstitial grain spaces, between grain coats, and within the second and third types of quartz cement (Fig. 10d).

SEM analysis shows Galway sandstone porosity consists of 5-20 μm size irregularly shaped isolated pore spaces rimmed by illite and trace apatite (Figs. 10c,d,e). Total porosity from SEM analysis of Galway samples 8689 (2,648.4 m) and 8692 (2,649.3 m) is approximately 3-4% (Table 4). The primary porosity is composed of equant voids impinged by quartz cement (Figs. 10a,b,c,d,e). Galway Formation core porosity is consistent with SEM measured values ranging from 3 to 4.4% (Table 4). Permeability values of Galway Formation cores were at or below 0.050 mD (0.023- 0.050 mD) (Table 4).

Table 4
Host rock attributes from sedimentary rock using EDS and optical point count data (N; grain size; mineralogy; primary, secondary and total porosity; IGV), laboratory testing (MXCT porosity; core porosity; permeability), and geophysical surveys (NPHI).

Sample	Depth (m)	Formation	Subunit	Method	N	Grain Size (mm)	Detrital (% composition)					Cement (% composition)		Porosity (% void space)						
							Quartz	K-feldspar	Dolomite	Illite Clays	Accessory Minerals	Quartz Cement	Dolomite Cement	Primary Porosity	Secondary Porosity	Total Porosity	NPHI[1]	MXCT Porosity	Core Porosity[2]	IGV (%)	Permeability (air) mD
8685	2647.9	Galway Formation	Rose Run	Optical	323	0.05-1	84	-	3	-	0.5	11.5	-	1	-	1	1.09	0.173	2.44	12.5	0.023
8689	2651.8	Galway Formation	Rose Run	SEM - EDS	700	0.2-1	74.1	-	1.58	1.68	0.19	19.11	-	2.89	0.47	3.36	1.21	0.303	4.43	22.0	0.027
				SEM - EDS	700		66.7	-	3.2	0.6	0.4	25.07	-	3.7	0.3	4		0.216		28.8	
8692	2650.0	Galway Formation	Rose Run	SEM - EDS	700	0.05-1	71.8	-	4.03	1.12	0.05	19.6	-	3.01	0.36	3.37	1.20	0.036	3.66	22.6	0.050
8699	2652.1	Galway Formation	Rose Run	Optical	318	0.05-1	73.3	0.75	2.1	0.5	0.25	20.2	0.5	2.3	-	2.30	0.00	0.004	3.05	22.5	0.045
9270	2826.2	Potsdam Group	Ausable Formation	Optical	315	0.1-0.5	60.1	2	20.1	5.8	0.5	10	1	0.5	-	0.50	1.11	0.003	0.59	11.5	0.004
9360	2853.7	Potsdam Group	Ausable Formation	Optical	311	0.1-1	70.2	9.8	7.4		0.1	10.1	1.2	1	-	1.00	0.58	0.002	1.83	12.3	0.018
9361	2854.0	Potsdam Group	Ausable Formation	SEM - EDS	700	0.1-0.5	68.8	28.55	-	2.14	-	-	-	0.56	-	0.56	0.66	0.003	4.50	-*	0.032

[1] Neutron porosity (NPHI) values are calculated from an initial limestone calibration.
[2] Core porosity determined by whole core helium pycnometer testing by Repsol. IGV (intergranular volume) values are calculated from SEM and transmitted light petrography point count data.
* indicates IGV value not calculated.

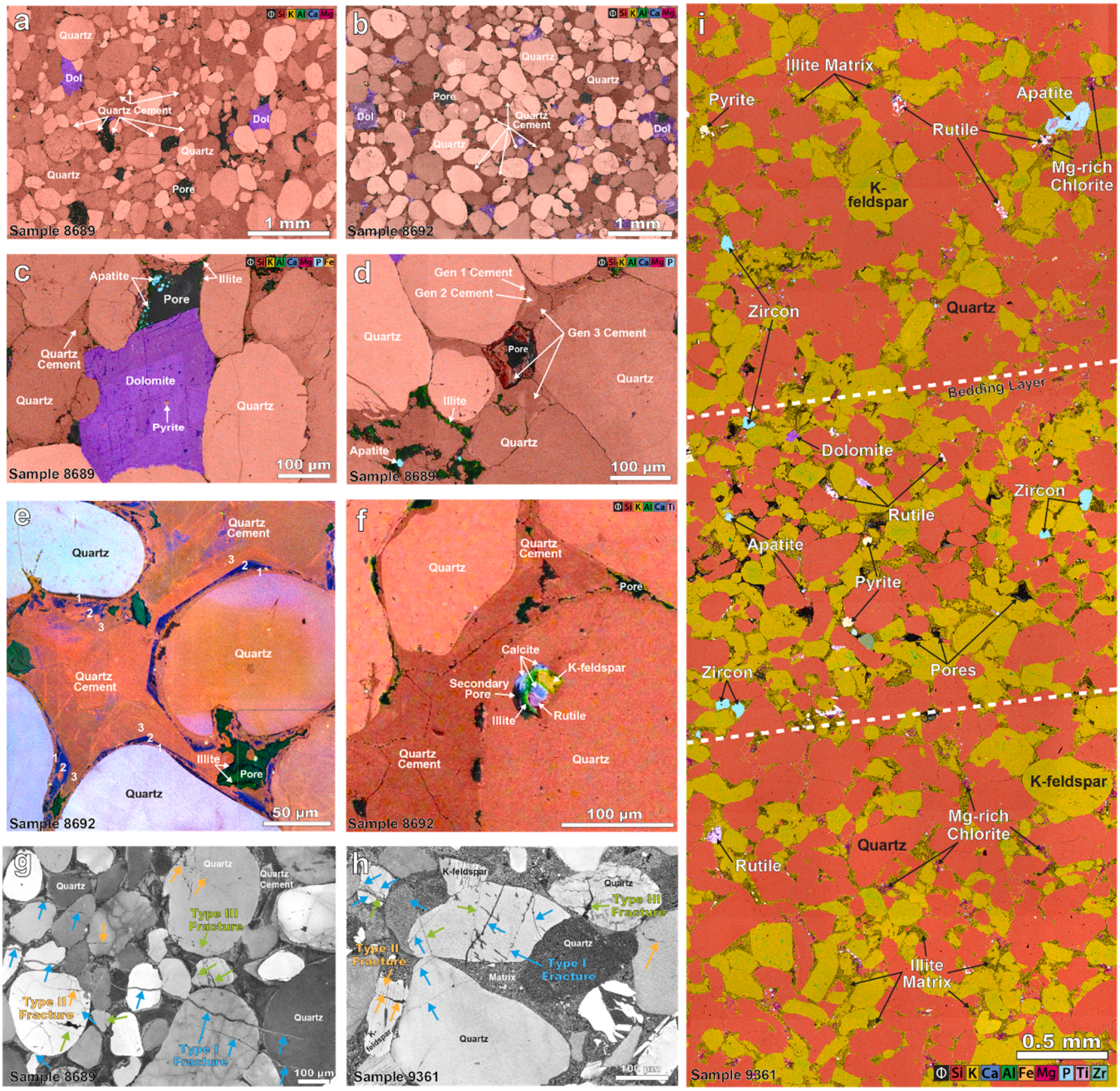

Fig. 10. Scanning electron microscope CL and EDS images of sandstone textures and mineralogy. a) Composite CL-EDS image from sample 8689 shows subrounded detrital quartz grains in a polygonal quartz cement with sparse dolomitized relicts of granular carbonate (Dol) and porosity (black). Some larger pores are most likely caused by grain plucking during thin sectioning. b) Composite CL-EDS image from sample 8692 showing subrounded detrital quartz grains and more abundant dolomite surrounded by quartz cement. c) Composite CL-EDS image of quartz sand grains, polygonal quartz cement, dolomite replacement of detrital carbonate with pyrite inclusion, and porosity containing accessory apatite and illite in sample 8689. d) Composite CL-EDS image of quartz sand grains, three generations of pore-filling quartz cement, and interstitial illite and apatite from sample 8689. e) RGB Color SEM-CL image from sample 8692 of subrounded quartz grains with three generations of quartz cement (1, 2, and 3) showing differing textures and luminescence colors. Illite precipitation (black) preserved scattered porosity (green). f) Composite CL-EDS image from sample 8692 showing secondary pore in detrital quartz infilled with illite, k-feldspar, rutile, and calcite. g) Panchromatic CL image of different microfracture morphologies (Types I, II, and III) in quartz cemented sample 8692. h) Panchromatic CL image of fracture morphological Types I, II, and III in fine-grained matrix of sample 9361. Note the smaller apertures and lengths of Type I transgranular microfractures in a matrix-dominated sample versus 8689 (g). i) EDS large area bedding-perpendicular mosaic from sample 9361 HR4 showing subangular to subrounded quartz and k-feldspar grains surrounded by an illite and Mg-rich chlorite matrix. Dashed lines, bedding contacts. Note the concentration of accessory minerals and increased porosity (black) in the middle bedding layer.

4.2. Sidewall core fracture attributes

4.2.1. Macroscopic fractures – basement sidewall cores

All basement sidewall cores have macroscopic fractures. Planar fractures in basement cores have low or high angles (2 to 88.4°) to the core axis and contain quartz, quartz-feldspar, and clay mineral fills (Fig. 8). Basement macroscopic fracture lengths range between 2- and 50-mm. Widths of filled macroscopic fractures vary from 0.215 to 3.3 mm. Linear subvertical and subhorizontal quartz-feldspar filled macroscopic fractures in sample 9505.5 crosscut mica foliation and biotite lineations (Fig. 9c). Brecciated macroscopic fracture patterns with quartz-K-feldspar fills are identified in sample 9459. These breccia-

patterned, filled fractures are crosscut by subvertical to intermediate dipping (~45°) fractures containing dark grey clay fills (Fig. 8). Boudinaged quartz-filled fractures are observed parallel to the core axis in sample 9459 (Fig. 8) and are displaced by late clay-filled intermediate dipping fractures.

4.2.2. Macroscopic fractures – Cambrian-Ordovician sidewall cores

Two partially open macroscopic fractures are identified within Galway Formation sandstone sidewall cores, with apertures of 0.115 to 0.265 mm (samples 8692 and 8699, respectively). The macroscopic fracture in sample 8692 is 32 mm long, subvertical, and has one fracture tip preserved in the core. This fracture strikes 93° and dips 81.9° and has visible open pore space and bridging quartz cement (Fig. 7a). Quartz bridge cements in the open fracture of sample 8692 have 20-200 μm repeating laminar crack and seal textures (Fig. 11). This subvertical fracture is also identified in the image log in the post-sidewall core FMI survey (Fig. 7c). Another macroscopic fracture in sample 8699 is a 5 mm long subhorizontal fracture dipping 5° SSE. This fracture is partly bridged by quartz.

Dolostone also displays filled fractures. For example, a subvertical carbonate filled macroscopic fracture with an aperture of 1.15 mm, which strikes 192° and dips 78.2°, occurs in Galway Formation dolostone sidewall core sample 8730 (Fig. 7b). The trace of this fracture crosscuts a bedding plane contact between dolostone and dolomitic sandstone (Fig. 7b) and was not identified in the FMI surveys.

4.2.3. Microfracture identification and classification

Thin sections of Potsdam Group and Galway Formation sidewall cores contain quartz-filled microfractures which, in a few cases, are visible under TL as steeply dipping fluid inclusion planes, but are mainly distinguishable using SEM-CL imaging. Two of the five Galway dolostone cores have common microfractures (Table 1), filled with various minerals including dolomite, calcite, and pyrite. Microfractures are common in three dolostones cores of the Tribes Hill Formation (Table 1), based on MXCT scans, including some that are open.

Microfractures were classified into three categories (I, II, and III) (Laubach, 1997) based on fracture trace morphology, crosscutting relationships with grains and cements, and grain displacement. Categorization of microfractures using these criteria aids distinguishing

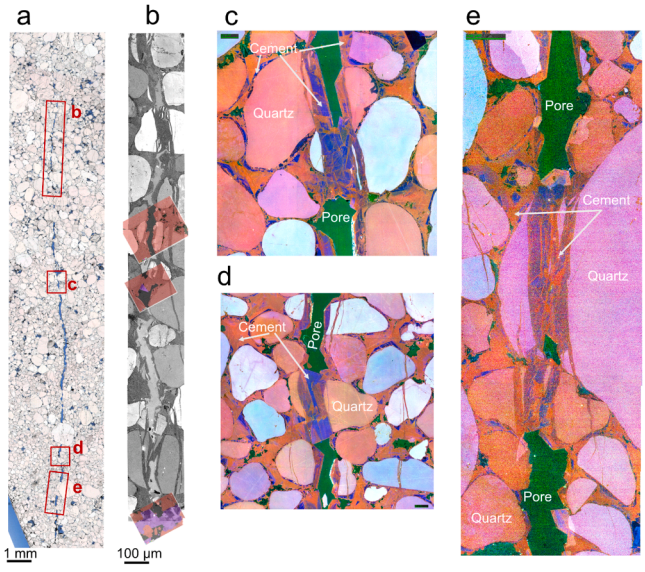

Fig. 11. Images of partially bridged subvertical macro-fracture in Galway Formation sample 8692 (see Fig. 7). a) Transmitted light image of subvertical fracture with SEM imaging areas outlined. Blue marks pore space. b) Panchromatic CL image of quartz-bridged fracture. c, d, e) Color CL images documenting bridged pore space within subvertical macrofracture.

microfracture sets that represent the small size fraction of regional macrofractures from microfractures of local or no structural significance caused by compaction, inheritance, or sample handling. Category I microfractures are defined as fractures with straight (linear) traces crosscutting multiple grain boundaries and interstitial cement. Orientations and geometries of Category I fractures occur without consistent relation to grain centers or grain contacts, indicating they post-date deposition and are most likely to have a genetic relationship with larger fractures (Laubach, 1997). Traces of Category I fractures in sidewall core samples that crosscut larger grains or grain contacts may form mildly curvilinear patterns and are further subclassified as Category Ia fractures.

Category II microfractures are confined within grains (intragranular) and have curvilinear to radiating wedge shapes. Some are at or near grain-to-grain contacts and are thus associated with local grain crushing or with faults. Category III fractures are filled and abruptly terminate at or within grain boundaries; these are inherited (Laubach, 1997). Category III fractures are not inventoried.

Category I fractures are potentially parts of fracture populations that include large fractures, and thus were the focus of microfracture analysis. Among sandstone sidewall cores analyzed using SEM-CL images (Table 4), Category I microfractures are the most pervasive type, totaling 1,078 fractures, and consist of sharp linear transgranular traces with jagged aperture variations (Fig. 10g,h). Lengths of Category I microfractures range from 20 μm to 3.6 mm and have minor intragranular en échelon geometries in large quartz grains. Subvertical Category I fracture traces show more curvilinear geometries near grain boundaries in bed-perpendicular thin sections than in bed-parallel thin sections of the same sample. The frequency of Category Ia fractures is significantly lower than Category I, accounting for approximately 37 fractures among all samples analyzed. Kinematic apertures of Category I microfractures range from 0.5 to 115 μm; however, the majority of the kinematic aperture widths are between 1 and 15 μm and are discussed in Section 4.2.6. Aspect ratios of Category I fractures average on order of 10^{-3} (Table 5) and can reach 10^{-4}.

Category I microfractures sharply crosscut both mineral grains and interstitial cement. Category I occurs in sets of different strike orientations, explained in Section 4.2.4. Grain displacement of all Category I fractures is perpendicular to the fracture walls. Translative or rotational displacement of fractured grains is not observed. Most Category I microfractures are filled with quartz. Among microfractures, a single subvertical microfracture in core 8689 is partially open, with a kinematic aperture of 28 μm. Concentric and laminar quartz cements with a 5-15 μm thickness line this fracture.

Category II microfractures in CUBO sidewall cores occur as wedge shaped openings, with rapidly tapering apertures that appear to split grains apart and have the shortest traceable fracture lengths (~10-50 μm) (Fig. 10g,h). Wedge fractures are mostly present in sample 9361 (Fig. 10h).

4.2.4. Microfracture orientation and set identification

Microfracture orientation in space (relative to north) relies on first orienting each bed-parallel SEM-CL map to its true azimuth, according to the oriented sidewall core axis (Table 1). Each SEM-CL map transects a portion of the prepared thin section forming a scanline. A total of four SEM-CL bed-parallel scanline maps were completed and analyzed for samples 8689 and 8692 as well as four bed-perpendicular scanlines for samples 8689 and 9361 (Table 2). Oriented SEM-CL maps were overlapped digitally, forming a 2D transect map for each thin section that allowed microfracture trace orientation comparison. Microfracture traces were then digitally traced and categorized (Section 4.2.3), after which strike orientations were measured. A range of Category I strikes was observed.

To define sets, evidence of preferred orientation and relative timing is needed. Evidence of relative timing comes from abutting and crossing relations, where the abutted or crosscut fracture is older. The number of

Table 5
Sidewall core scanline data with measured strain and aspect ratios for microfracture sets. For each scanline (L1, L2, L5, L6), the number of fractures and their spacing data (maximum, minimum, average, standard deviation, coefficient of variability, and Normalized Correlation Count type) are listed. For plots of cumulative frequency per mm to fracture aperture, fits of data to either an exponential or a power law curve are expressed by the corresponding coefficients and exponents, and goodness-of-fit by the R^2 value. The cumulative strain given by all fractures in each scanline and the aspect ratios of the mean fractures are listed.

							Spacing							Exponential		Power law				
Sample	Formation	Scanlines	Orientation	Scanline Length (mm)	Fracture Set	Number	Max (mm)	Min (mm)	Avg (mm)	Stdv	Cv	Cv'	NCC Type	Coefficient	Exponent	Coefficient	Exponent	R^2	Strain	Aspect Ratio
8689	Galway Formation	**L1**	Bed parallel	20.68	F1	123	1.104	0.001	0.16	0.186	0.88	0.79	12a	13.43	-1.74×10^3	-	-	0.9664	0.0058	6.4×10^{-3}
					F2	90	1.398	0.004	0.26	0.274	0.97	0.72	12a	-	-	1.59×10^{-7}	-2.3279	0.9225	0.0047	6.6×10^{-3}
					F3	107	0.779	0.002	0.18	0.166	1.11	0.63	12a	-	-	1.06×10^{-7}	-2.3581	0.9489	0.0043	7.0×10^{-3}
					F4	45	2.665	0.005	0.38	0.534	0.72	0.97	12a	-	-	1.44×10^{-6}	-1.9078	0.9078	0.0023	6.8×10^{-3}
		L2	Bed parallel	36.94	F1	107	2.069	0.002	0.36	0.380	0.95	0.73	12a	6.33	-1.32×10^3	-	-	0.9698	0.0039	7.7×10^{-3}
					F2	64	3.594	0.004	0.57	0.731	0.78	0.90	12a	5.59	-1.54×10^3	-	-	0.9704	0.0024	6.9×10^{-3}
					F3	73	4.257	0.002	0.63	0.767	0.83	0.84	12a	2.75	-1.24×10^3	-	-	0.9272	0.0021	7.6×10^{-3}
					F4	62	2.843	0.004	0.55	0.615	0.91	0.77	12a	4.08	-1.43×10^3	-	-	0.9853	0.0021	9.8×10^{-3}
8692		**L5**	Bed parallel	25.64	F1	25	4.060	0.087	0.90	0.710	1.00	0.55	12a	-	-	8.00×10^{-6}	-1.6490	0.8865	0.0010	5.2×10^{-3}
					F2	-	-	-	-	-	-	-	-	-	-	-	-	-	-	-
					F3	17	3.443	0.010	0.90	0.712	1.01	0.55	12g	-	-	1.09×10^{-5}	-1.5601	0.9702	0.0008	7.3×10^{-3}
					F4	31	3.806	0.010	0.73	0.859	0.82	0.81	12a	-	-	2.30×10^{-3}	-0.7418	0.9027	0.0034	1.1×10^{-2}
		L6	Bed parallel	37.66	F1	61	2.534	0.008	0.50	0.769	0.91	1.07	12a	-	-	1.03×10^{-5}	-1.6346	0.8660	0.0025	7.0×10^{-3}
					F2	-	-	-	-	-	-	-	-	-	-	-	-	-	-	-
					F3	20	6.754	0.019	1.85	0.757	0.94	0.28	12a	1.14	-1.11×10^3	-	-	0.9842	0.0008	6.1×10^{-3}
					F4	47	3.120	0.006	0.73	0.658	1.06	0.63	12a			3.51×10^{-3}	-0.7722	0.9510	0.0056	1.0×10^{-2}

clear cross-cutting relations among Category I microfractures is limited but a range of abutments and crosscuts are apparent. Traces of microfractures transecting other microfractures in bed-parallel scanlines exhibit both arrestment and continuations forming T and X nodes, respectively (Fig. 12a). Overprinting fracture fill quartz cement at nodal areas provides the primary relative timing data, given that neither shear sense nor consistent abutments occur. Therefore, the relative timing of microfracture orientation in bed-parallel scanlines was determined by cross-cutting relationships of fracture fill cements using SEM-CL images. Relative timing of microfracture orientations were systematically compared within the 2D transect maps for consistency.

Based on microfracture orientations and their relative timing, four fracture sets were identified in Galway Formation sandstones: F1 (NW-SE), F2 (NE-SW), F3 (N-S), and F4 (WSW-ENE) (Fig. 13). Fracture set 1 is the most abundant, having 316 fractures, and an average orientation 138.8° (Fig. 13). Standard deviation of F1 strike orientations (21.1) is the highest among the four fracture sets (Fig. 13). The F2 fracture set overprints the F1 set and shows an average strike orientation of 29.4°. F3 fractures crosscut the F2 fractures with an average strike of 183.4° and show the least orientation variance (Fig. 13). Fractures from set F4 average a strike at 256.9°, crosscut fracture sets F3, F2, and F1, and exhibit the longest fracture traces.

Apparent dip angles of microfractures were measured from sidewall core bed-perpendicular thin section scanlines in Galway Formation sandstone sample 8689 and Potsdam Group sample 9361 (Table 2; Fig. 14a). Microfracture apparent dips fall into three categories: subhorizontal (~ <20°), intermediate (20< x <70°), and subvertical (>70°). Category I and Ia subhorizontal microfracture dips are prevalent

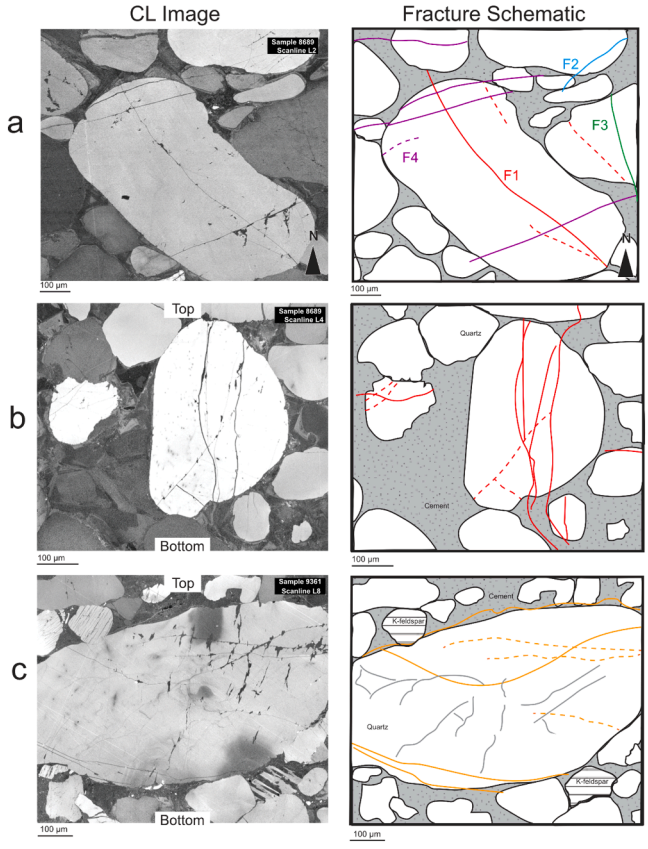

Fig. 12. Panchromatic CL images of fracture features (left) with corresponding fracture schematic tracings (right). a) Bed-parallel view of fracture sets in sample 8689 documents crosscutting relationships. Dotted lines indicate a fracture terminates within a grain. b) Bed-perpendicular image from sample 8689 shows subvertical dips. c) Bed-perpendicular image from sample 9361 showing bed-parallel fractures.

in sample 9361 (Fig. 12c). Microfractures of intermediate dips are the shortest in length and occur sparsely (28 fractures) (Fig. 14a); in sample 8689 these fractures dip to the north and south, whereas in sample 9361 the dips are easterly and westerly. Subvertical dipping fractures form the longest fractures and the largest population (136 fractures) as curvilinear traces overprinting intermediate and subhorizontal dipping fractures (Fig. 12b). Subhorizontal dipping fractures total 42 and have curvilinear traces transecting multiple grains (Fig. 12c).

4.2.5. *Microfracture spatial arrangements*

Fracture occurrence was measured in bed-parallel SEM-CL maps of Galway Formation sandstone samples. Average microfracture spacing per set along bed-parallel scanlines ranged from 0.16 and 1.85 mm (Table 5). The maximum fracture spacing coefficient of variation (C_V), where C_V is σ/μ, σ is the standard deviation of spacings and μ is the mean, ranges between 0.72 to 1.11, indicating low dispersion between the standard deviation and mean fracture spacing.

To analyze spatial arrangements, we used *CorrCount* software (Marrett et al., 2018) to calculate normalized fracture intensity (NFI) and normalized correlation count (NCC). NFI characterizes fracture intensity over the given scanline length and can show statistically anomalous intensities with respect to scanline position. NCC uses inter-fracture positions of all fractures in a scanline array, not just nearest neighbors, and can distinguish between periodic, random, and organized, complex and hierarchical arrangement patterns. NCC quantifies uncertainty, minimizing interpretation subjectivity in comparing patterns to random arrangements. Calculation of these parameters allows interpretation of whether fracture spatial arrangements are clustered or anticlustered (periodic) to a greater extent than a random distribution (Figs. 15 and 16).

Normalized fracture intensities are calculated for every microfracture set within each scanline (Fig. 14). Position interval lengths with normalized intensity values exceeding the upper 95% confidence limit are statistically distinct clusters. Length intervals of 0.1 to 3 mm exceed the upper confidence bound and are observed as spikes for most samples; however, these spikes are limited in both number (1-5 spikes) and intensity (Fig. 15). A systematic or repetitious spike pattern on the NFI plots is not apparent. For NCC analysis (Fig. 16), length scale intervals with NCC values exceeding the upper 95% confidence limit reveal distinct clusters whose spacings at these length scales are more common than for randomized spacings. In all microfracture sets, low intensity spikes occur below a length scale of approximately 0.1 mm. The occurrences of these low intensity spikes show only limited, mild clustering at short length scales.

4.2.6. *Opening displacement (kinematic aperture)*

Scanlines in bed-parallel SEM-CL maps of Galway Formation sandstone samples record opening displacement versus distance, allowing calculation of fracture strain and analysis of kinematic aperture size distributions. Opening displacement or kinematic aperture is the width of the fracture where crossed by the scanline irrespective of whether the fractures are open; in our case the microfractures are quartz sealed. One dimensional analysis of cumulative opening displacement versus original scanline length indicates a low overall fracture strain of less than 1.7% (Table 5). All four microfracture sets show mostly narrow microfractures, with slight variation (Fig. 17). Sets F1, F2, and F3 have generally similar aperture size distributions, with a median of 1 to 1.25 µm. Apertures sizes of set F4 average 2.72 µm but are more dispersed, with a wider distribution of larger apertures (Fig. 17). The F4 set also has the largest measured microfracture aperture with a 28 µm open, quartz-lined microfracture in sample 8689.

Size scaling analysis was performed using cumulative aperture frequency distributions normalized by scanline length for each fracture set (Fig. 18). Linear regressions of the cumulative frequency aperture distributions produced both power-law and exponential best-fit lines, with residual sum of squares (R^2) values ranging from 0.8660 to 0.9853

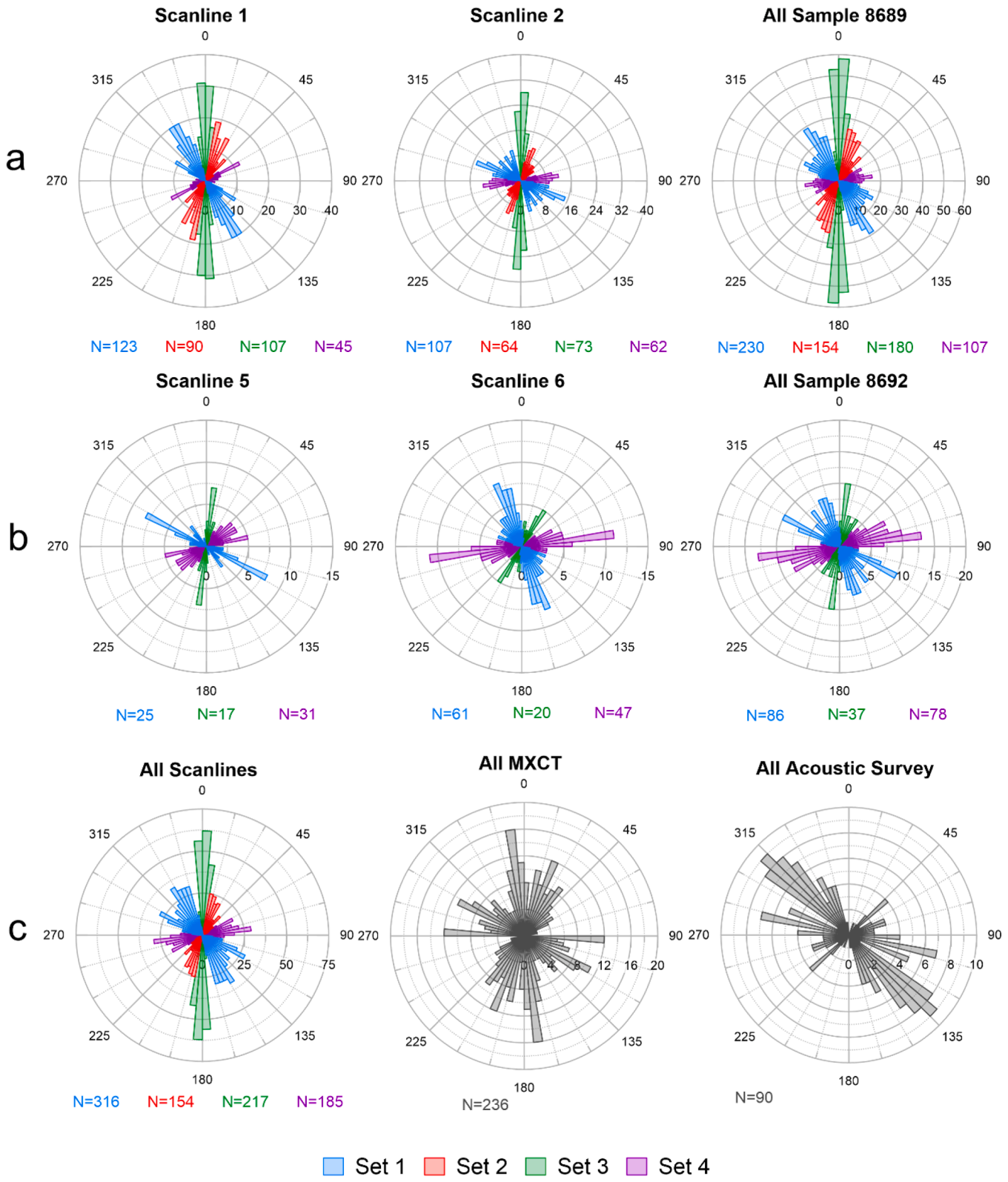

Fig. 13. Rose diagrams of fracture sets in samples 8689 (a) and 8692 (b) by scanline (left and center) and in total (right). c) Compiled fracture set orientations from all core microfractures (left) are compared to MXCT fracture (center) and acoustic survey far-field fracture (right) orientations from the Cambrian-Ordovician borehole section. MXCT fracture orientations are from sandstone samples 8685, 8689, 8692, 8699, 9360, and 9361. Fractures containing open porosity are limited to two subvertical fractures with apertures of 28 and 115 μm in samples 8689 and 8692, respectively.

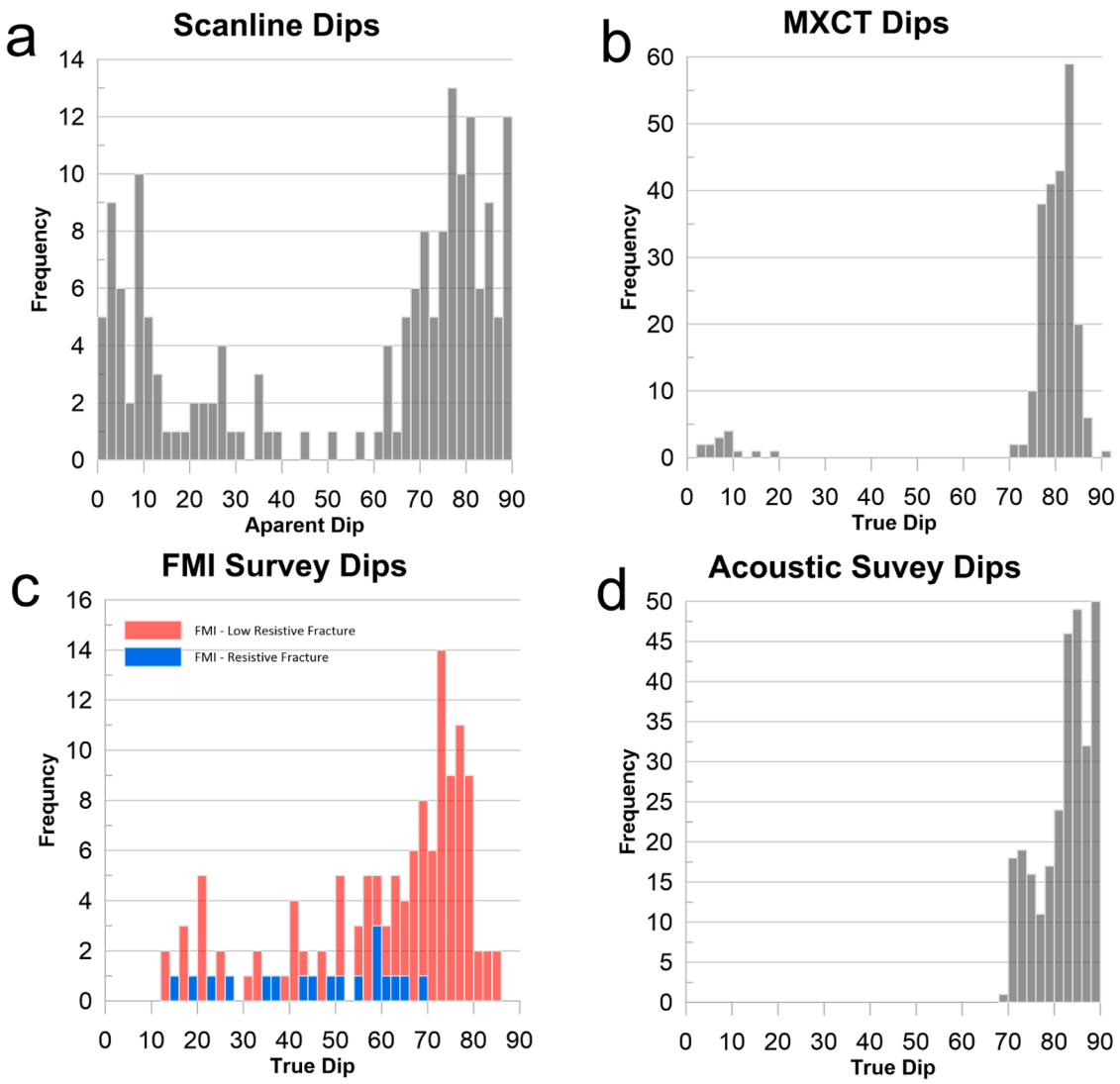

Fig. 14. Histograms of fracture dips from a) sidewall core scanline analysis, b) MXCT fracture sets F0 to F4, c) FMI surveys and d) acoustic surveys in the Cambrian-Ordovician open borehole section.

(Table 5; Fig. 18). In sample 8689, negative-slope exponential and power-law functions were the most common fits across fracture sets. In contrast, fracture sets in sample 8692 were generally best described by negative-slope power-law distributions, with the exception of fracture set F3 in scanline 6. Among the fracture sets in sample 8692, power-law distributions differed by approximately 0.9 orders of magnitude (Table 5).

4.3. Sidewall core fractures characterized from MXCT

Fractures in 3D density voxel models were identified as planar density contrasts overprinting sedimentary and mineralogic textures. MXCT fracture set identification was completed using crosscutting relationships of similarly oriented planar fractures forming fracture sets. Relative timings of each fracture set are not ascertained from cross-cutting relationships because cement overprints or abutments could not be observed in 2D images or 3D voxel models.

4.3.1. MXCT fractures – basement sidewall cores

MXCT analysis of four basement sidewall cores shows penetrative linear and brecciation fractures. Subvertical and linear fractures in samples 9493, 9496, and 9505.5 are traced through the extent of the 3D voxel model. Rectangular and discontinuous high-density contrasts, corresponding to biotite lineations, are observed throughout sample 9505.5 averaging a 110.7° rake and a plunge of 64.9°. Elongate density contrasts corresponding to pinitized pseudomorphs show layering and clustering with long axes oriented parallel to biotite lineations in sample 9496. Brecciation in sample 9459 is penetrative with complex anastomosing fracture fills. Open porosity was not detected in basement samples by MXCT analysis.

4.3.2. MXCT fractures – Cambrian-Ordovician sidewall cores

MXCT analysis reveals six sandstone cores contain narrow fractures (25 to 110 μm wide) that have semi-continuous planar density contrasts. Traces of these fractures are subvertical and subhorizontal relative to bedding planes (Fig. 19). Lengths range from 1.5 to 33 mm.

Strike orientations and dips of the fractures were identified by tracing and measuring the geometry of each fracture in 3D cut-away voxel models. Full scale and automated techniques to isolate or select fracture traces (e.g. thresholding and region of interest interpolation) could not be completed due to the small density gradient contrast of these features combined with the voxel resolution.

Four predominant subvertical fracture orientations occur: NW-SE (F1), NE-SW (F2), N-S (F3), and WNW-ESE (F4) dipping 70.4° to 90° (Fig. 19), categorized as fracture strike sets. Dip angles of subvertical fractures are commonly greater than 78° (Fig. 14b). A fracture strike set

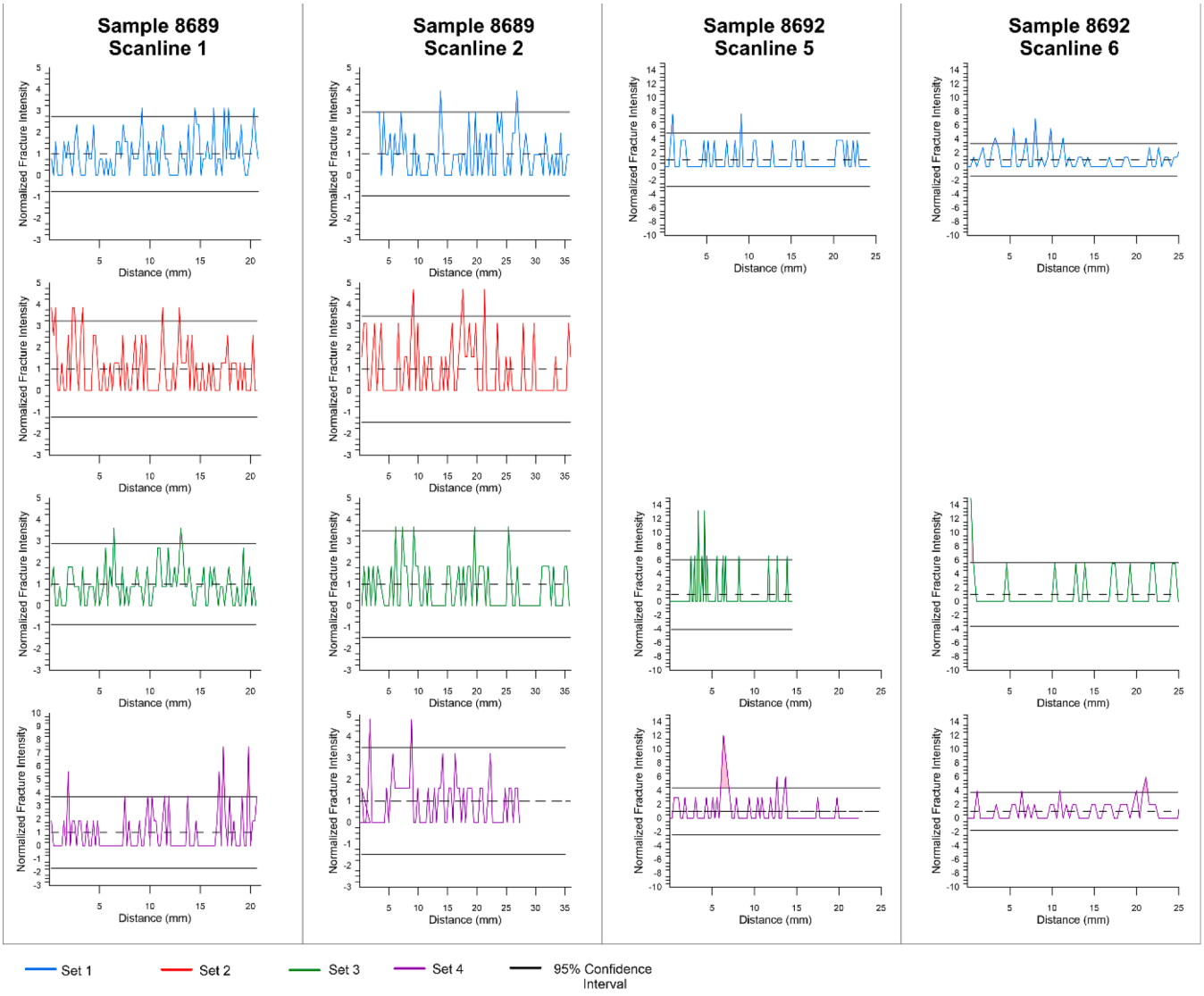

Fig. 15. From sidewall core analyses, plots documenting normalized fracture intensity (NFI) (vertical axes) as a function of position along a scanline (horizontal axes) for each microfracture set in bed-parallel scanlines.

with a subhorizontal to slight south dip, F0, occurs in sample 8689 (2648.4 m) (Fig. 19c). Generally, only two or three discernible sets of subvertical fractures are apparent per sample (Fig. 19c). Strike orientation dispersion of subvertical fracture sets range between 13.9° and 43.5° with Set F2 having the highest dispersion value.

4.4. BHI survey results

Structural feature analysis of BHI surveys focused on the linear and sinusoidal resistivity discontinuities in FMI surveys that crosscut primary sedimentary structures (Figs. 7c, 20a,b,c) in the Cambrian-Ordovician section and metamorphic textures in the basement (Fig. 20d). Within the basement complex, borehole breakouts occur throughout the open borehole section and account for more than 50% of coverage making identification of fractures related to structural deformation challenging. Image quality of the UBI survey improved in the basement section, allowing further fracture characterization analysis. Within the Cambrian-Ordovician section, the dominant primary sedimentary structures are horizontal planes across the full perimeter of the borehole, interpreted as bedding planes. Fracture sets categorized from BHI surveys were based on groupings of orientation. Fracture frequency, calculated on three-meter bins using BHI structural feature analysis data, is presented in Fig. 21 with associated stereonets in Fig. 22.

4.4.1. BHI survey results – basement

Low resistivity fractures in the basement complex are the most abundant type and form three sets: a moderately southeast dipping set (Fig. 22g), a NNW-SSE oriented subvertical set (Fig. 22h), and a fracture set consisting of crossing linear traces (Fig. 23). The set of southeast dipping planes shows partial sinusoidal traces covering 25-50% of the borehole circumference in all borehole quadrants of the FMI surveys and has an average dip of 50.9° (Figs. 22g and 23). The subvertical set generally strikes NW-SE and averages a dip of 85.3° (Fig. 22h) with a height range of 10 to 86 cm. Crossing partial linear traces occur in specific depth zones as 5 to 30 cm long traces oriented at variable angles throughout the circumferential borehole image (Fig. 20d). Low resistivity subvertical fractures are observed consistently throughout the basement complex while the moderately dipping set is concentrated in only a few depth zones (Fig. 21). Crossing linear traces are frequent in 1-to-10-meter zones (Figs. 20d, 23).

Mixed resistivity fractures in the basement open borehole section totaled 57 and have an average dip of 56.2° (Fig. 22j). Traces of mixed resistivity fractures show extents of 10 to 50% of the borehole circumference in FMI surveys. Resistive linear fractures in the basement

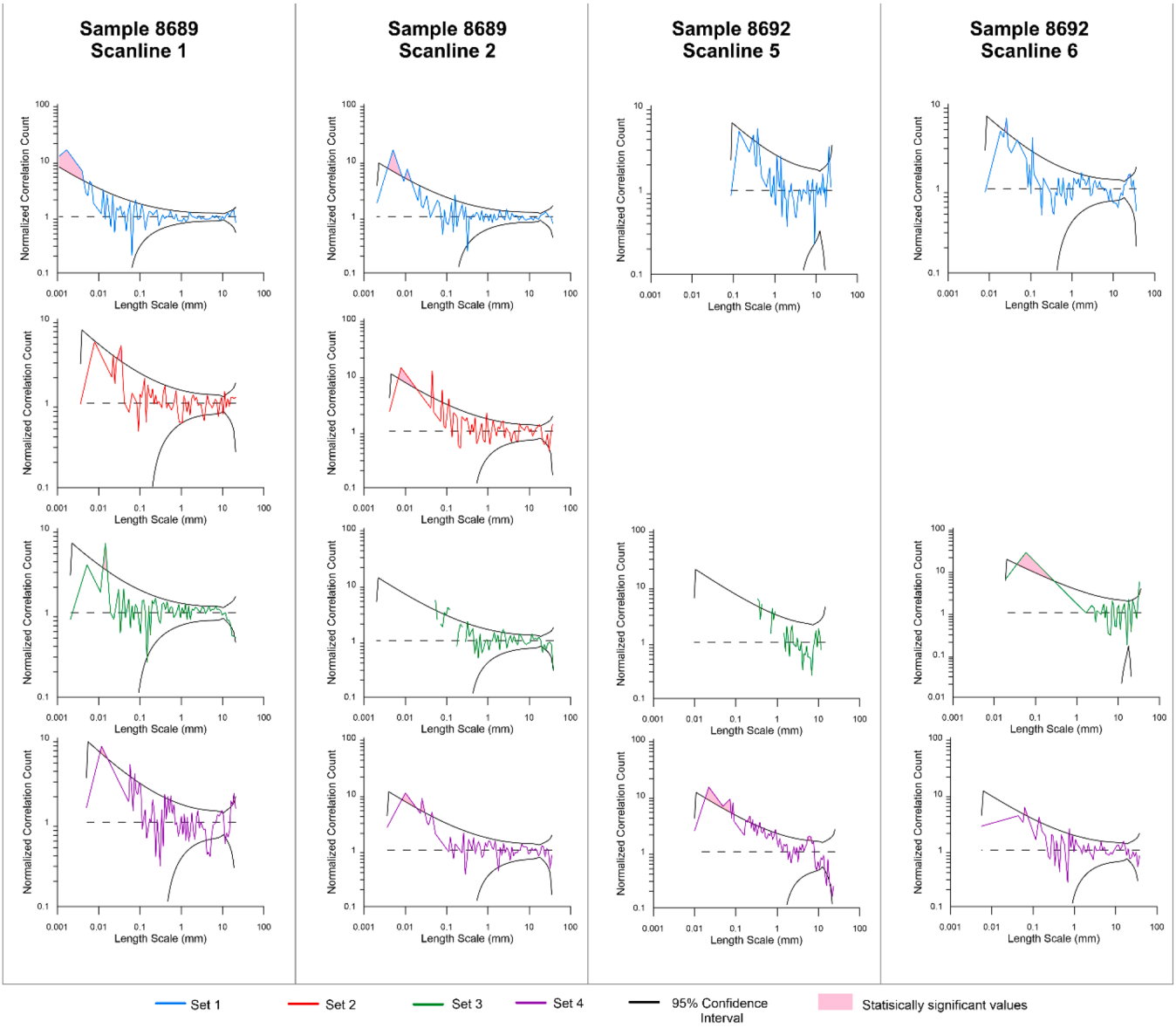

Fig. 16. NCC plots document the spatial arrangement of Normalized Correlation Count (vertical axes) relative to scanline length scale (horizontal axes). The observations in bed-parallel scanlines 1, 2, 5 and 6 are compared to smooth lines corresponding to random spacing. Filled areas mark parts of curve exceeding 95% confidence interval.

complex cover 25 to 50% of the borehole circumference and are subhorizontal dipping, between 8.5 to 21.2°. The average dip of resistive fractures in the basement open borehole sections was 10.7° (Fig. 22i).

UBI images intermittently improved in the basement section showing partial fracture traces of moderate to low acoustic wave amplitude (Fig. 23). The majority of fracture traces observed in the FMI surveys are not fully observed in UBI images (Fig. 23). For example, low resistivity fractures in the post-sidewall core survey are absent or appear as moderate amplitude traces – signifying a filled nature (Fig. 23).

Fracture frequency in the basement is higher than within the Cambrian-Ordovician open borehole section (Fig. 21). From the lower Potsdam Group contact and into the basement complex, fracture frequency increases significantly between 2,865 to 2,916 m. Fractures within this interval are predominantly moderately SE dipping or NNW-SSE oriented subvertical fractures.

4.4.2. BHI survey results – Cambrian-Ordovician

Within the Cambrian-Ordovician open borehole section, linear and sinusoidal traces cross-cutting sedimentary bedforms are interpreted as fractures and show low, mixed, and high resistivities in FMI surveys. Dips of low resistivity fractures range from shallow to steep (>70°) (Fig. 21a,b) throughout the open borehole section. Within the Cambrian-Ordovician section, low resistivity fractures form three sets: a moderately southeast dipping set, a NW-SE oriented subvertical set, and a E-W oriented subvertical set (Fig. 21a,b). The southeast dipping fractures manifest as partial sinusoidal traces covering less than 25% of the borehole circumference and isolated within the NE and SW quadrants, and have an average dip of 61.2° (Fig. 20b,c). Southeast dipping low resistivity fractures are commonly clustered and exhibit curved shapes with flattened apical geometries (ski-slope and saddle shaped traces) (Fig. 20b,c). NW-SE and E-W oriented sets of subvertical low resistivity fractures appear singularly as 30 to 200 cm high linear semicontinuous traces that cross-cut bedforms (Figs. 7c, 20c).

Mixed resistivity fractures show both low and high resistivity signatures along a sinusoidal or linear trace. Mixed resistivity fractures in the Cambrian-Ordovician section total seven and dip moderately (21.8 to 68.5°) to the southwest (Fig. 22d), covering 25-50% of the borehole.

High resistivity fractures are the least abundant type, with an

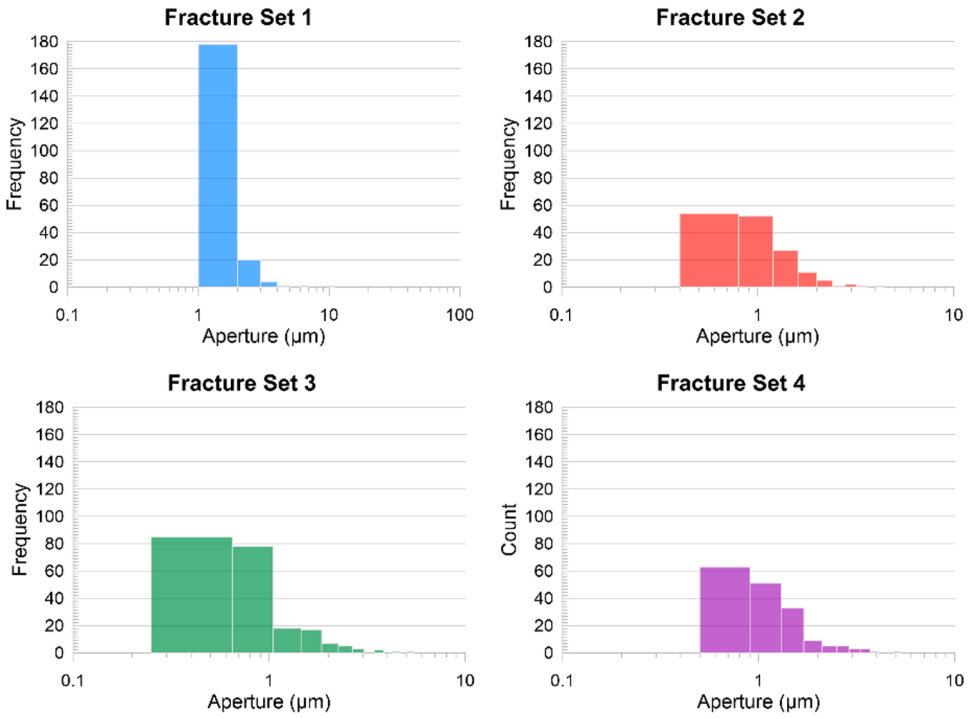

Fig. 17. Histograms of aperture frequency for each microfracture set measured in bed-parallel scanlines.

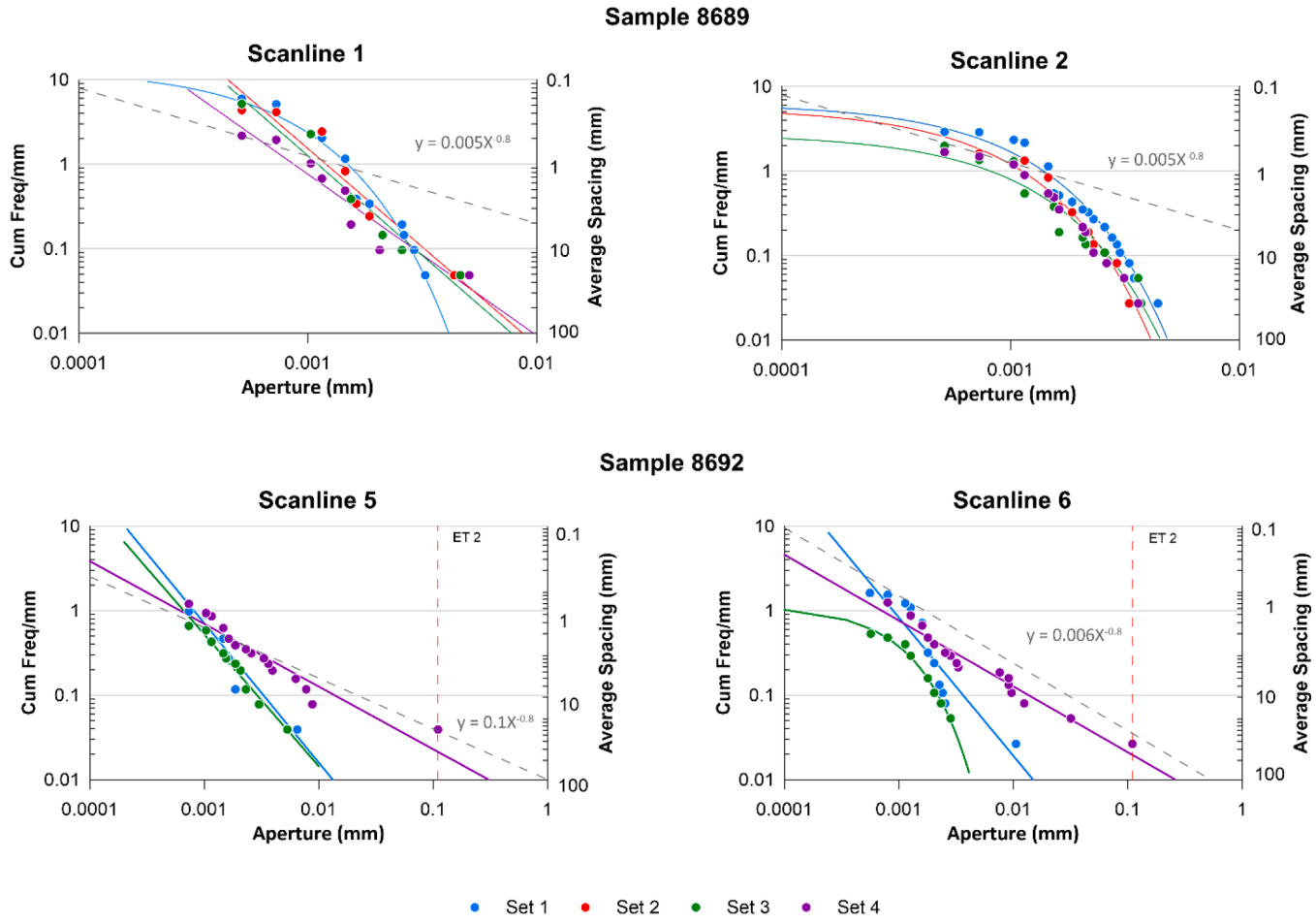

Fig. 18. Cumulative frequency plots for kinematic apertures of all microfractures per scanline, color coded into Sets F1 through F4. ET, emergent threshold, is plotted for the partially open macroscopic fracture. The grey dotted line represents a power slope regression to data of -0.8 slope (after Hooker et al., 2014).

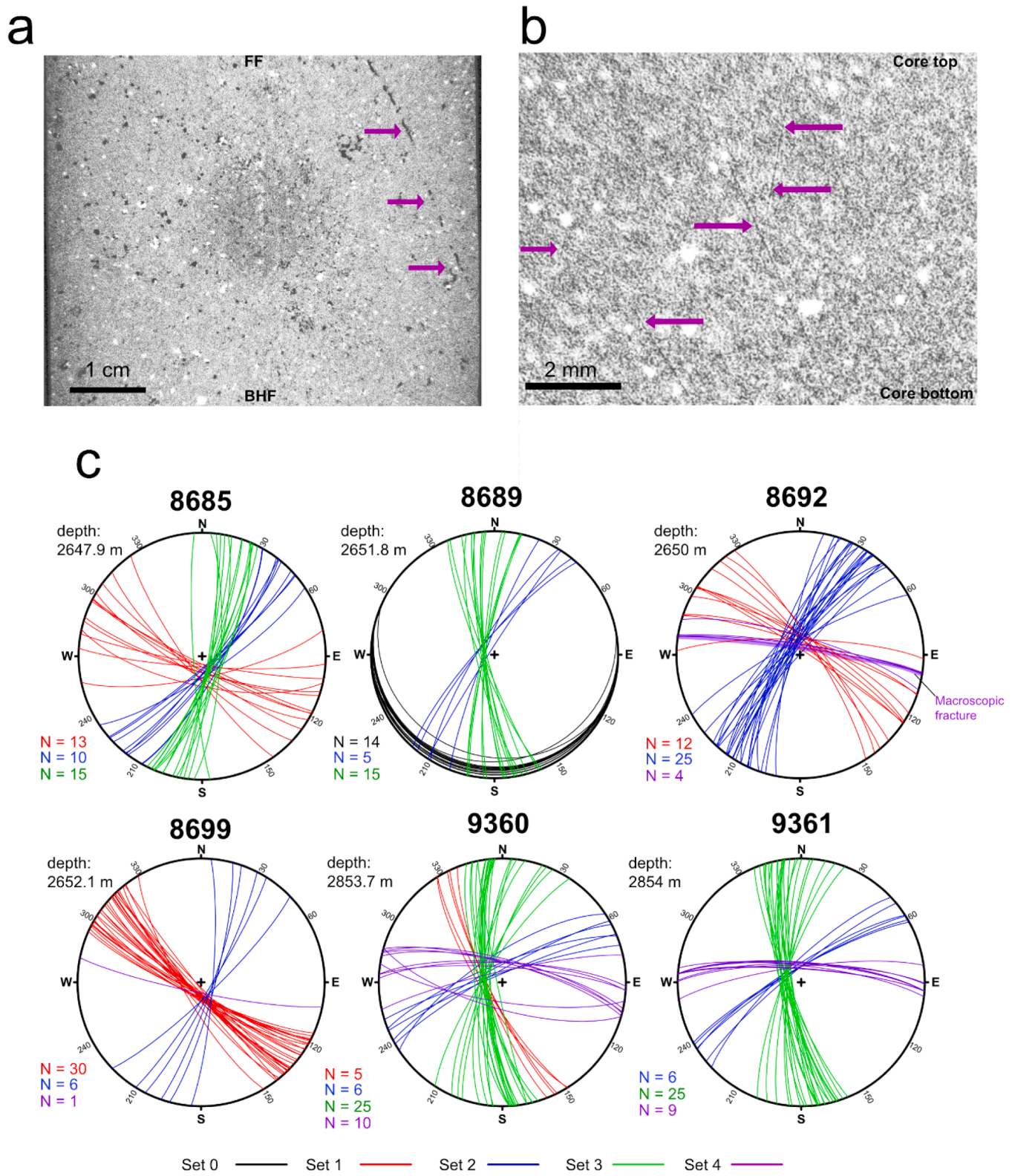

Fig. 19. MXCT images and stereonet diagrams of observed fractures in sidewall cores using Stereonet (Allmendinger et al., 2011). a) Bed parallel oriented image of sample 8692 showing intercepted bridged macroscopic fracture. b) High magnification MXCT image of selected fracture area in sample 8699 shows subvertical fracture traces. c) Stereonets of microfractures in six sidewall cores.

average dip of 46.2° in the Cambrian-Ordovician section (Fig. 22c). Traces of resistive fractures in the Cambrian-Ordovician section cover more than 50% of the borehole circumference; they appear thinner in overall aperture and show a tendency to cross-cut finer sedimentary bedding (Fig. 20a).

Increased fracture frequency occurs within 5 depth zones of the open borehole section (Fig. 21a,b). The first zone is the central part of the Tribes Hill Formation (2,400 m) where low and mixed resistivity

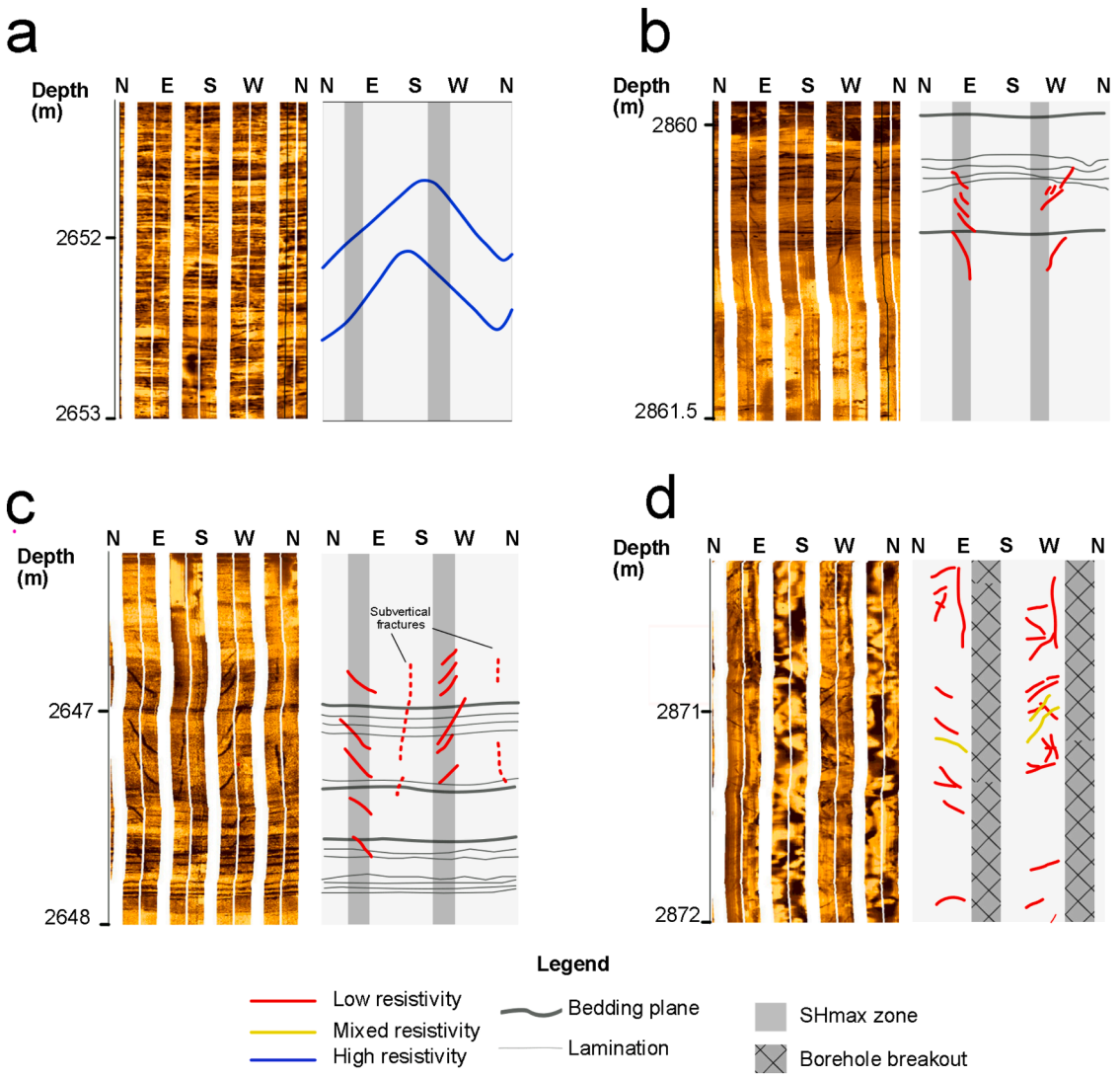

Fig. 20. Four depth intervals in the open borehole section of the CUBO borehole, FMI survey images (left) with traces of fractures (right). a) Shallow dipping resistive fractures in Galway Formation show full sinusoidal traces. b) Partial chatter-like low resistivity fracture traces in Potsdam Group. c) Subvertical low resistivity fractures and clustered moderately dipping saddle-shaped traces in Galway Formation. d) Partial low and mixed resistivity fractures in basement.

fractures are clustered in algal limestone beds. Frequency of low resistivity fractures increases within bedded sandy dolostone in the lower zone of the Little Falls Formation (2,560 to 2,570 m). The highest fracture frequency is at the top of the Galway Formation (2,652 m), consisting of a 12 m thick zone of low and high resistivity fractures hosted in a thinly bedded, medium-grained sandstone unit. Below 2,652 m, fractures are less frequent until a deeper zone of the Galway Formation at 2,773 m where low and mixed resistivity linear fractures are observed in fine and medium grained sandstones. Fracture frequency increases markedly in the Potsdam Group, where fractures are mainly the low resistivity type and crosscut laminated sandstone bedforms between 2,826 and 2,829 m. At the lower Potsdam contact, fractures are generally low resistivity and dip moderately to steeply (Fig. 21a).

4.5. Acoustic log results

Analysis of compression and shear wave forms acquired from the acoustic survey (Sonic Scanner) identified over 1,000 farfield reflectors (compliance anomalies) from both monopole and dipole signal sources within the open borehole section. From these compression and shear wave reflectors, 283 fractures were interpreted using 3D STC and SCANFAM analysis by SLB (Fig. 24). The basis for interpreting fractures is mainly the narrow aspect ratio and relatively straight traces of these anomalies.

Measured raw acoustic wave slowness was first corrected by completing wave path modelling using borehole geometries acquired from a multi-arm caliper survey. A mode dispersion compensation correction was then applied to the wave path model to account for differences between flexural mode phase velocity and formation shear velocity caused by borehole rugosity. Zones of the basement complex in the open borehole section were outside of corrected tolerance criteria (Appendix C3). As a general data qualification, interpreted acoustic far field fractures in the basement portion are considered to have a high degree of uncertainty. Corrected wave velocities were within tolerance of the inversion model fit in the Cambrian-Ordovician section of the open borehole.

For basement units, compression and shear wave analysis interpreted 127 (monopole) and 66 (dipole) subvertical fractures in various orientations, dipping between 70.2 and 89.9° (Fig. 22k,l). Radial distances to interpreted fractures ranged from 1.6 to 57.6 m. The fracture orientations do not display groupings but rather a high strike variability spanning 360° (Fig. 22k, l).

In the Cambrian-Ordovician section, compression and shear wave analysis of monopole signals identified 22 subvertical fractures in an

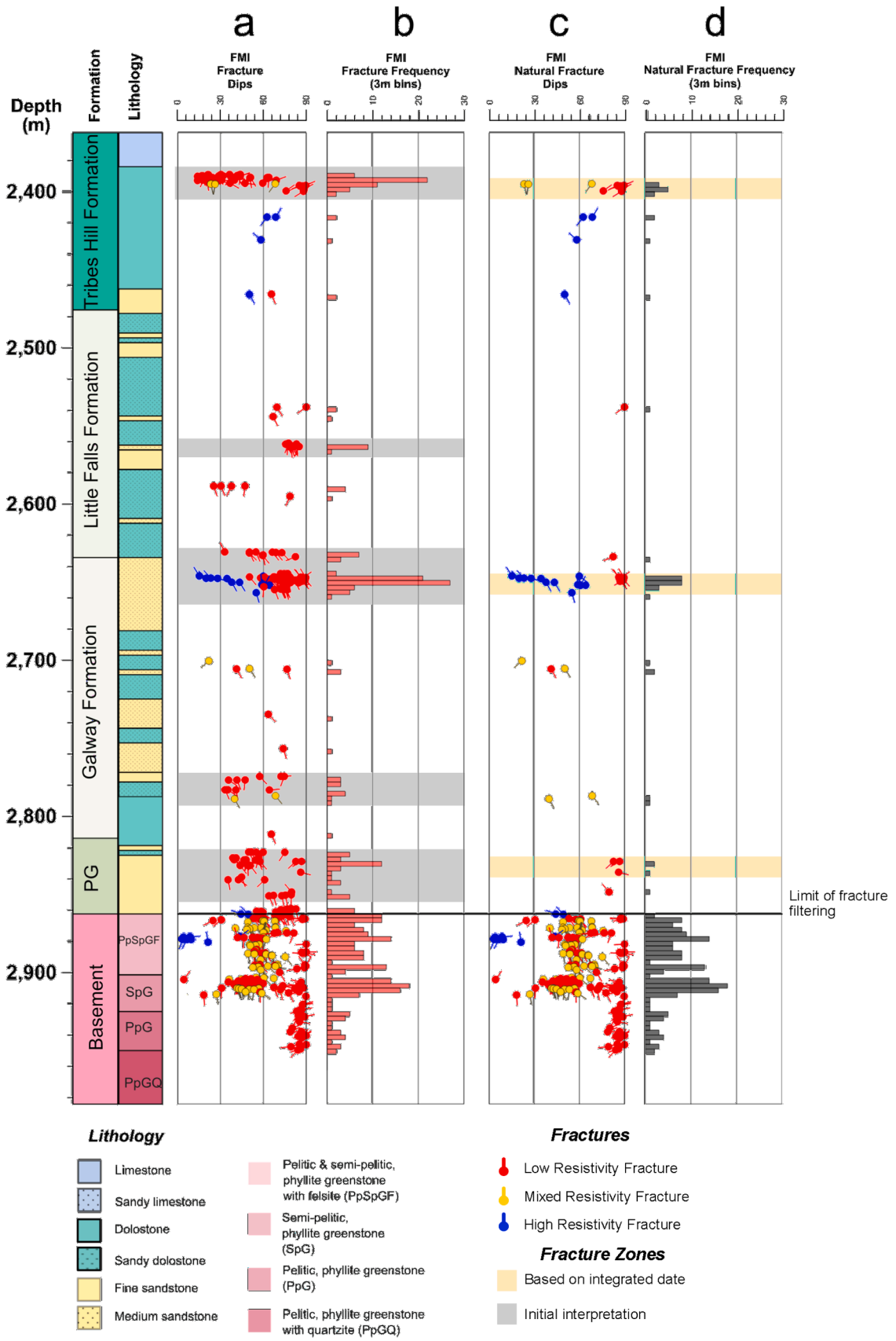

Fig. 21. Comparison of unfiltered (a,b) and filtered (c,d) fracture dips and fracture frequencies from FMI surveys. Fracture frequencies are plotted using 3-m bins. Filtered fracture picks (c,d) are based on sidewall core analysis.

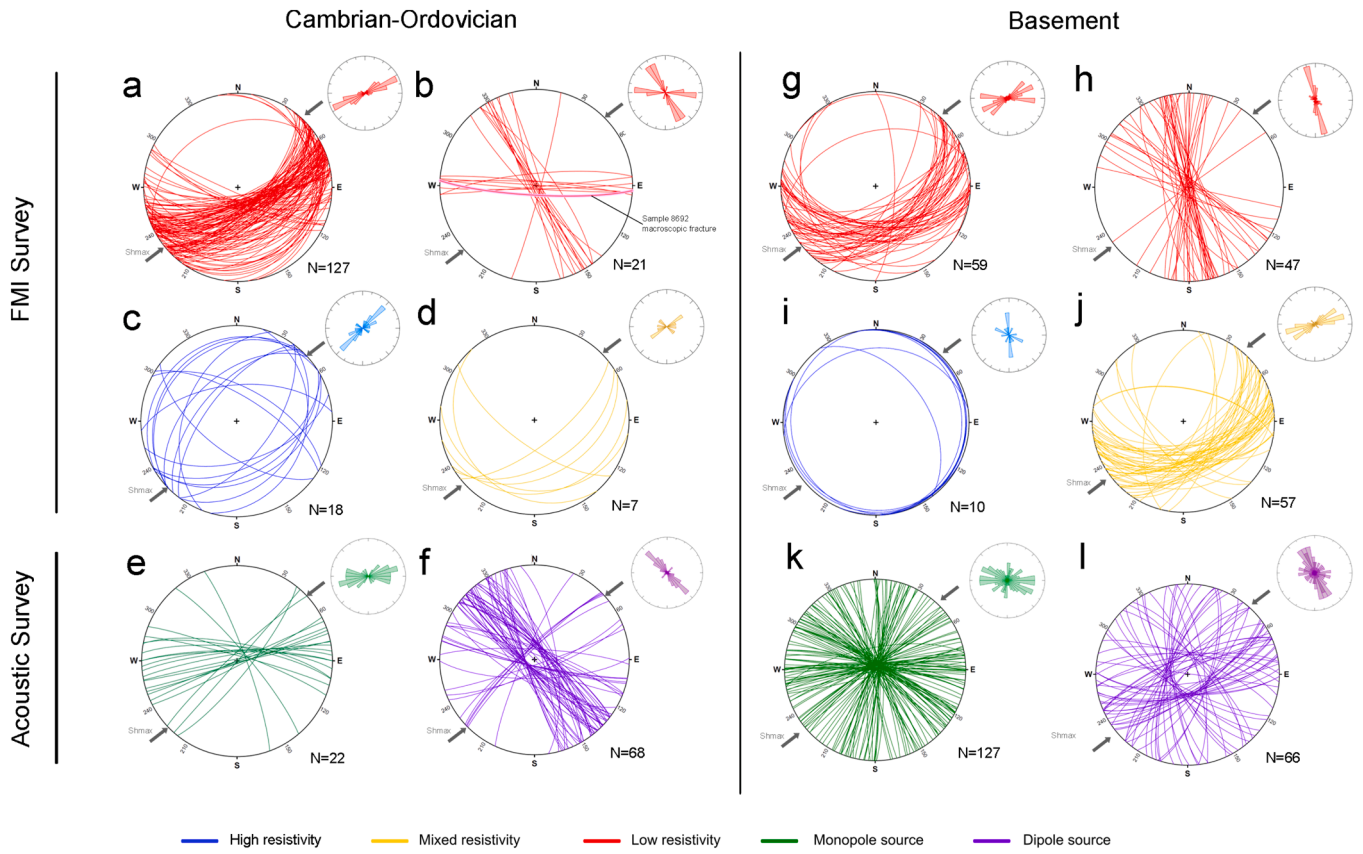

Fig. 22. Lower hemisphere equal area stereonets of fractures interpreted from FMI and acoustic surveys through the Cambrian-Ordovician section and the basement using Stereonet (Allmendinger et al., 2011). Bidirectional rose diagrams of strike values are adjacent. a) Low resistivity fractures dipping moderately to the southeast that are interpreted as drilling induced fractures. b) Subvertical fracture set exhibiting low resistivity. c) High resistivity fractures from FMI survey analysis. d) Fractures showing mixed resistivity. e, f) Fractures interpreted from the Sonic Scanner monopole and dipole surveys, respectively. g) Moderately dipping low resistivity fracture traces in basement. h) Low resistivity subvertical fractures from basement complex. i) Subhorizontal high resistivity fractures in basement complex. j) Fractures showing mixed resistivity in basement rocks. k, l) Fractures interpreted from the sonic scanner monopole and dipole surveys in basement rocks, respectively.

ENE-WSW orientation, between 75 and 89.6° (Fig. 22e). Analysis of compression and shear waves created from dipole transmitters identified 68 subvertical fractures (70.3 to 90°), among which fractures oriented NW-SE are more abundant than those oriented ENE-WSW (Fig. 22f). Radial distances from the borehole of interpreted fractures ranged from 2.9 to 67.6 m (Fig. 24).

The acoustic fracture frequency increase in the Potsdam Group and basement complex is concordant with fracture frequency increases observed in BHI surveys (Fig. 24). Below 2,865 m, fracture frequencies increase from both monopole and dipole signal sources (Fig. 24). Fractures are infrequent from 2,550 to 2,865 m (Little Falls and Galway Formation), averaging a fracture frequency of 0.17 fractures per meter of depth (f/m) (Fig. 24). The frequency of interpreted acoustic survey fractures is high between 2,388 and 2,402 m, within the Tribes Hill Formation (2,377 to 2,625 m), averaging a formation fracture frequency of 0.53 f/m (Fig. 24).

5. Discussion

In New York (e.g., Jordan et al., 2020; Fulcher et al., 2023) and elsewhere (e.g., Limberger et al., 2018; Stumpf et al., 2018), suitable temperatures for direct-use geothermal development occur within units that are about 3 km deep or deeper. Metamorphic rocks overall have low porosity and permeability (Wolff, 1982; Brace, 1980) due to recrystallization and mineral realignment reducing open pore space. Primary porosity and permeability of sandstones and carbonate rocks at these depths is typically low due to compaction and diagenesis (Ehrenberg et al., 2009). Diagenesis is highly sensitive to thermal exposure (i.e., the cumulative time at elevated temperature) (e.g., Taylor et al., 2022). For formerly deeply buried Paleozoic rocks in New York, host rock porosity is low as measured in sidewall cores and regionally (Kolkas and Friedman, 1999, 2007). Fluid flow in either metamorphic or compacted sedimentary rocks is likely fracture dominated.

Assessing EGS geothermal feasibility in the CUBO targets therefore depends in part on determining the preexisting natural fractures to target as natural flow conduits and to plan hydraulic stimulation. For effective targeting and facility design we need to glean from the limited available data knowledge of lithology and natural fracture sets and their attributes.

Fracture systems in metamorphic terranes may be complex due to protracted loading histories and brittle and ductile deformation causing anisotropic fabrics and structural inheritance (e.g., Gillespie et al., 2021) (e.g., Gillespie et al., 2021) but some old crystalline rocks have markedly simple and sparse fractures (e.g., Wang et al., 2019). In folded and faulted low grade metamorphic rocks some fractures may have systematic relations to folds (Hancock, 1985) and shear zones (Boullier and Robert, 1992), but in other cases fractures are superposed on metamorphic structures (Ji et al., 1997). EGS exploration and development in metamorphic terranes such as the Blue Mountain project (Fercho et al., 2023) and the Utah Forge project (Jones et al., 2024) demonstrate the value of empirical fracture system knowledge for reservoir targeting and developing reservoir stimulations.

Fractures in sandstones and carbonates often show systematic sets that exhibit orthogonal or en echelon patterns (e.g., Laubach and

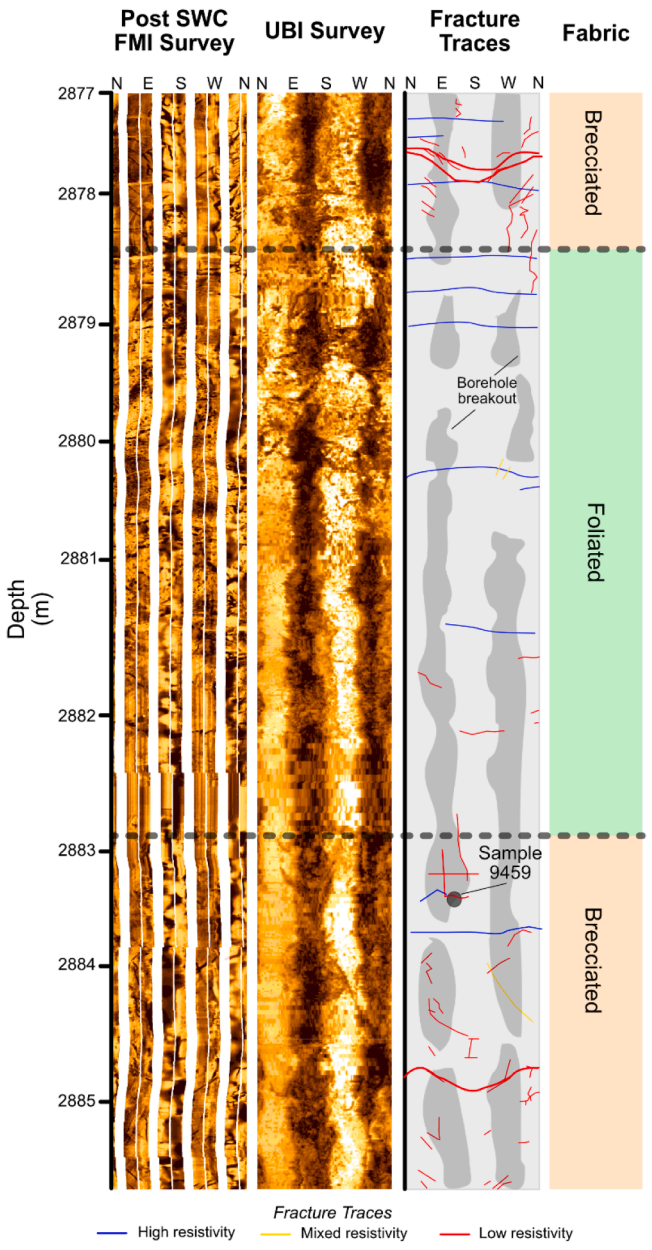

Fig. 23. Comparison of post sidewall core (SWC) FMI survey and UBI survey (dynamic image) in basement complex interval. Sample 9459 location marked with observed fracture traces. Zones of brecciation based on BHI data and sidewall core fractures are demarcated.

Diaz-Tushman, 2009; Hooker et al., 2013; Gutmanis et al., 2018; Elliott et al., 2025). Unlike metamorphic rocks, sedimentary units may have a relatively homogeneous composition thereby reducing mechanical heterogeneity at the granular level (Anders et al. 2014). In quartz-rich sandstones, mechanical heterogeneity is reduced enabling extensive micro- and macrofracture networks to form (e.g., Laubach and Tushman, 2009; Hooker et al., 2013; Hooker et al., 2018), where fracture propagation is often controlled by grain-to-grain contact and cement strength (Lloyd and Knipe, 1992).

In the following sections we show how sidewall cores enable primary lithologic characterization and evaluation of fracture parameters and ground truthing of intercepting BHI survey fractures, while also allowing comparison of the indirect fracture evidence from far-field acoustic interpretations. We further show the usefulness of incorporating sidewall core information and outcrop analog data to create conceptual subsurface fracture models of formation targets that can be used for planning future geothermal reservoir data collection and facility design.

5.1. Lithology, texture, and diagenesis from sidewall cores

5.1.1. Basement rock attributes

Basement sidewall cores (Cayuta Formation) document phyllites containing evidence of a sequence of polyphase deformation consisting of initial S1 foliation, an L1 lineation, and late fractures and breccia. The peak prograde metamorphic mineral assemblage is biotite-muscovite-quartz. Chlorite and pinite are retrograde minerals based on their relative alteration and overprinting textures and are consistent with evidence of greenschist facies rocks documented in drill cuttings by Valentino et al. (2024). L1 lineations hosting elongate biotite and quartz augens suggest extension following formation of the S1 foliation.

Sidewall core laboratory analysis confirms the porosity of phyllites in the CUBO well is low (0.45 to 5.1 %; Table 3), similar to other phyllites whose porosity and permeability is generally low to negligible (Meng and Li, 2013). Petrography found isolated microporosity in pinite pseudomorphs of core 9496. The anomalous ~5% porosity is likely a combination of the observed microporosity measurement artifacts due to small samples (20 mm) (Table 3). Porosity values provided by NPHI (Table 3) are not reliable in the basement rocks, because several of the common metamorphic minerals contain hydrogen.

5.1.2. Cambrian-Ordovician rock attributes

CUBO sidewall cores provide in situ mineralogy, texture, and porosity of buried Cambrian-Ordovician rock types of the Allegheny Plateau (Table 4). Galway Formation sidewall cores show quartz arenites have low porosity with three quartz cement types. Porosity averages 1.3% for the dolostones and 2.6% for the sandstones. Potsdam Group sandstones in sidewall core samples are highly compacted with the lowest average intergranular volume value of 11.9% (Table 4) while exhibiting grain crushing textures (Fig. 9h) and a single quartz cement type.

Galway Formation and Potsdam Group sidewall cores show low porosity (0.59 to 4.5%) due to compaction and progressive quartz cementation which is common for moderately to deeply buried sandstones throughout the continental U.S. (e.g., Dutton et al., 1993). Pore spaces in Galway Formation sandstones range in size from 5 to 20 μm and are consistent with median pore space sizes of 0.22 and 22.1 μm from regional core analyses by Kolkas and Friedman (2007). Large differences in porosity measurement between SEM imaging and MXCT analysis (Table 4) can be explained as censoring bias as pore spaces are consistently smaller than the minimum resolution of MXCT analysis (19 μm).

Pore spaces in the upper member of the Galway Formation appear semi-preserved by grain coats of illite, which we infer on textural grounds to have inhibited quartz cementation (Fig. 10c,e). The inhibition of quartz deposition by clay grain coats can lead to the preservation of higher sandstone porosities (Bloch et al., 2002; Ajdukiewicz and Larese, 2012), as in the Cambrian Mount Simon sandstone of Illinois (Freiburg et al., 2016; Freiburg et al., 2022). However, SEM-CL images in Galway Formation sandstones show illite grain coats are encapsulated by quartz cements (Fig. 10e) indicating quartz cementation commonly exceeded the inhibition capability of grain coatings. Another process that commonly causes locally anomalously high secondary porosity is feldspar and lithic grain dissolution (e.g., Dutton et al., 1993). Evidence for leaching has been reported from gas fields in the Galway Formation of western New York (Smith et al., 2010).

5.2. Insight from fractures in sidewall cores

5.2.1. Fracture morphologies – basement

Macroscopic opening mode fractures occur in all four basement phyllite cores, with censored lengths of 2 to 50 mm, widths of 0.14 to 3.3 mm, and variable strike orientations. Fracture patterns in basement

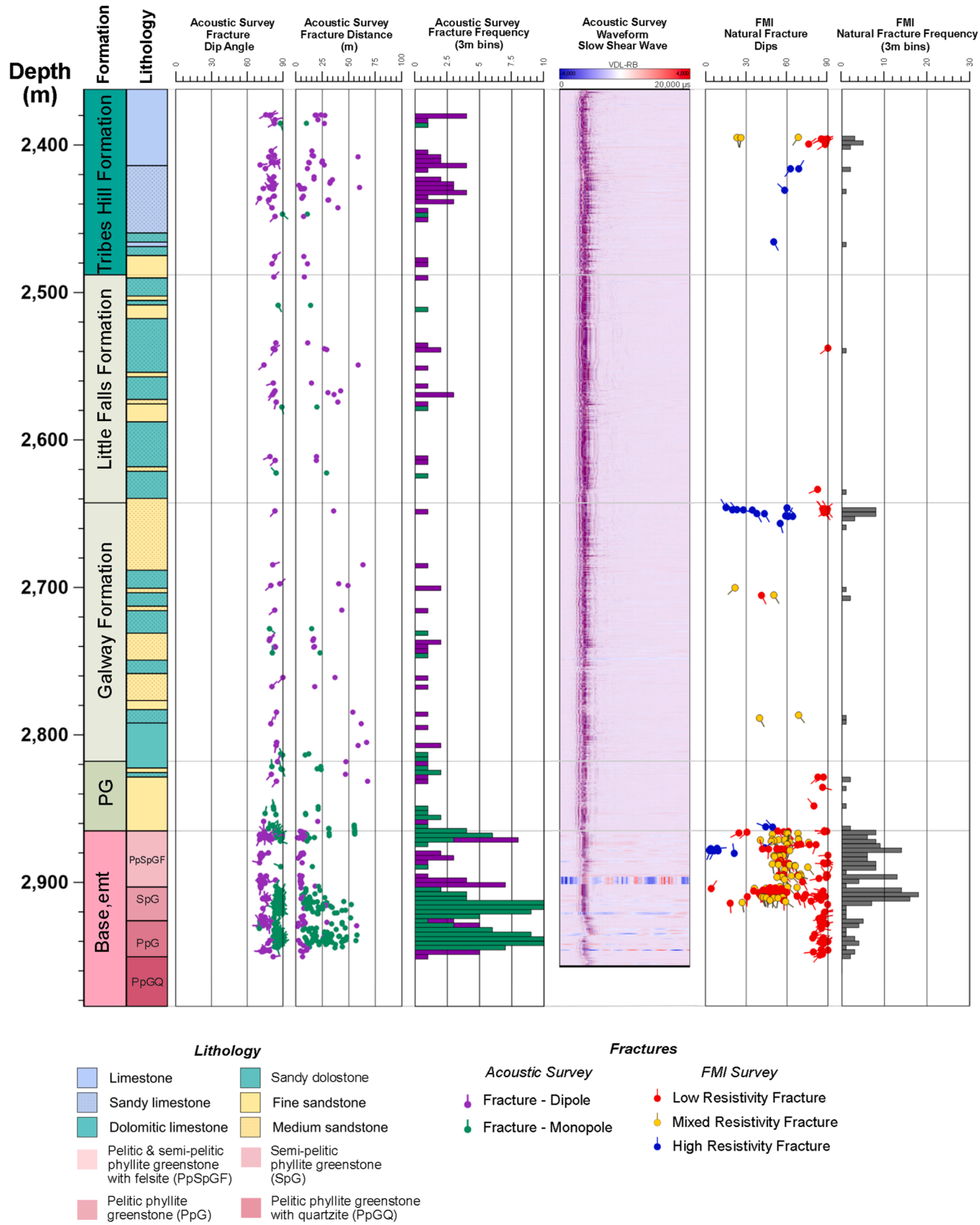

Fig. 24. Comparison of fractures picked from the FMI surveys and interpreted fractures from the acoustic survey in the open borehole section of CUBO. The slow shear waveform is included as a variable density log – receiver bank (VDL-RB). As in Fig. 21, the FMI fractures in Cambrian-Ordovician strata are filtered to represent only natural fractures. Fracture dips and frequencies are plotted for each data set, and distances of fractures from the borehole are plotted for the acoustic survey interpretation.

samples are unique to each sample. The wide range of strikes, lack of patterns in orientation or other attributes, and the absence of relative timing information mean that the fractures cannot be placed in sets or a relative time sequence. The textural evidence allows the following inferences.

In the Cayuta Formation, some fractures were filled with quartz and were later boundinaged. Quartz infill by itself does not reveal when fractures formed. Since boudinage textures are a form of brittle-ductile deformation, these quartz-filled fractures are likely not correlative with quartz-lined fractures in overlying Cambrian sandstones. Subsequently, the early fractures and boudins were displaced by fractures arranged in breccia patterns. The breccias are filled with quartz and potassium feldspar (Figs. 8, 9). Their timing is indeterminate. Breccia is further overprinted and displaced by intermediate and steeply dipping planar fractures filled by clay minerals. All the fractures we found in basement core are mineral filled and are likely hydraulically non-transmissive.

There is no sidewall core evidence to support the presence of large, open but unsampled fractures or to predict the patterns (if any) of these structures away from the wellbore. Nevertheless, the presence of some apparent late clay-mineral-filled fractures leaves open the possibility that elsewhere these fractures could be open. Our limited sampling of this hitherto unknown basement rock type provides few constraints.

5.2.2. *Fracture morphologies – Cambrian-Ordovician strata*

Sidewall core data provide several firm observations about open fractures in Cambrian-Ordovician strata and allow several plausible inferences about other fracture attributes. Three macroscopic fractures were found in oriented sidewall cores from the Cambrian-Ordovician section. The open sandstone fractures, both within the upper member of the Galway Formation, are linear, one subvertical and striking E-W and the other subhorizontal, with large apertures of 0.115 (ET2) and 0.265 μm (ET1), respectively. The 20-200 μm size bridges of non-euhedral quartz in the subvertical fracture (sample 8692; depth 2649.3 m) indicate this fracture aperture was open for a significant time period, given non-euhedral quartz overgrowth rates range between 1-15 μm per million years for the burial temperature range 100-150°C (Olson et al., 2009; Lander and Laubach, 2015). The subvertical macrofracture in a slightly deeper Galway dolostone trends in the F3 orientation (NNE-SSW), has a kinematic aperture of 1.15 mm and is entirely filled by dolomite. Although these are limited observations, they show that the lower Paleozoic sandstone and dolostone reservoir targets contain fractures, and that in the upper sandstone member of the Galway multiple fractures are open.

The macroscopic fracture in sample 8692 is the physical intercept of a low resistivity E-W striking subvertical fracture identified in the FMI survey analysis (Fig. 7c). Partial quartz-bridge fills authenticate its natural origin and provide a physical explanation for the semi-continuous nature of the E-W striking subvertical FMI fracture (Fig. 21b) where resistive material (quartz) truncates low resistivity fracture traces (Fig. 20c). This ground-truthing shows that linear, subvertical, low-resistivity features in FMI surveys are open fractures. The recurrence of a discontinuous pattern in the NW-SE striking subvertical fractures lends further confidence to their interpretation as natural features.

Morphologies of fractures observed in MXCT analyses of sidewall cores can be interpreted based on the continuity of their trace morphology and geometry (e.g. linearity and aspect ratio). The varying density intensity in MXCT fractures are interpreted as chiefly fills caused by spaced mineral bridges (Fig. 19b). MXCT subvertical fracture sets F1 to F4 show distinct average strike orientations of 138.8°, 29.4°, 183.1°, and 275°, respectively (Fig. 19). These are largely concordant with microfracture strike orientations defined in SEM-CL imaging (Fig. 13), differing for the F4 set from WNW-ESE (MXCT) to WSW-ENE (SEM-CL). In combination, the four subvertical microfracture sets F1, F2, F3, and F4 are oriented NW-SE, NE-SW, N-S, and WSW-ENE, respectively. These fracture sets occur in sidewall cores throughout the Galway Formation and the Potsdam Group (Fig. 19).

Given that in the modern maximum horizontal stress (SHmax) of the CUBO borehole is oriented N48E (Pinilla et al., 2023), the fracture sets orientations such as WSW-ENE (F4) and NW-SE (F1) might tend to close. The F2 set, oriented NE-SW, has the least favorable orientation for closure relative to SHmax. A pattern of open or closed fractures consistent with SHmax is not observed. The loading condition is one of all around compression, so the effect of different orientation is likely slight and similar open fractures have been found elsewhere at high angles to contemporary SHmax (Laubach et al., 2004). In the CUBO well open macroscopic fractures at high angles to SHmax could be due to the stiffening effect of quartz accumulation in the host rock and as well as quartz bridging between fracture walls, which tends to naturally prop fractures in an open position (Olson et al., 2007).

5.2.3. *Spatial arrangement, aperture size scaling, and average spacing*

Sparse sampling of macrofractures means the spatial arrangement and abundance of large fractures are not directly known. Populations of sandstone microfractures in the uppermost Galway are the only available data to investigate spatial patterns. Various approaches are applied to analyze the spatial arrangements of fractures, such as spacing distributions (Rives et al., 1992) and single-spacing averages (McGinnis et al., 2017). But these approaches typically assume that the averages are from populations where fracture size can be neglected (Ortega et al., 2006), an invalid assumption for a population containing macro- and microfractures. For CUBO microfractures, the Cv reaches values of approximately 1 (Table 5) for nearly all sets and is compatible with randomly spaced fractures (Hooker et al., 2023). Fracture spatial arrangement analysis based solely on spacing averages neglects specific locations of fractures. Application of NFI and NCC analysis (Marrett et al., 2018) with cumulative spacing statistics avoids these biases by interrogating arrangement data, so fractures of all sizes can be used. However, arrangement patterns are dominantly those of microfractures.

For the uppermost Galway sandstone sidewall cores, NFI patterns (Fig. 15) depict few low intensity fracture clusters at millimeter length intervals. NCC analysis (Fig. 16) shows that clustering at short length scales ($\leq$0.1 mm) is present but limited. Comparing microfracture arrangements to interpretative patterns of Marrett et al. (2018) shows all microfracture set spatial arrangements are indistinguishable from random but have patterns suggestive of hierarchical clustering. Microfracture populations may tend to be more clustered than macrofractures (Hooker et al., 2018). Spatial arrangements of macrofractures cannot be confidently extrapolated because of sparse fracture data sets and short scanline lengths causing truncation bias. Overall, the results are compatible with spatial arrangements of the various fracture populations being indistinguishable from random.

We used kinematic aperture population statistics to infer average spacing of fractures of a given size, an appropriate method because the spatial arrangement of fractures is indistinguishable from random (Ortega et al., 2006). Fracture spacing is derived from the inverse of the cumulative aperture distribution (Ortega et al., 2006). Measured kinematic apertures of microfracture sets F1 through F4 in uppermost Galway sandstone cores (Fig. 18) span one to two orders of magnitude and have exponential or power law distributions consistent with sandstone microfracture (Laubach and Gale, 2006; Hooker et al., 2011; Ukar et al., 2019) and macroscopic fractures elsewhere (Marrett et al., 1999; Ortega et al., 2006; Hooker et al., 2011). The F4 set, scanlines 5 and 6, containing the partially bridged macroscopic fracture (F4 set) (Fig. 7a), has an overall higher cumulative fracture intensity. Cumulative fracture intensity differences may reflect truncation bias as larger apertures of sets 1, 2, and 3 may be inadequately measured due to the limited sidewall core sample size (Laubach and Gale, 2006). However, in each uppermost Galway Formation sample, slopes of aperture size distributions are significantly higher than the -0.8 slope observed in some large sandstone fracture datasets (Hooker et al., 2014). This higher size-scaling slope of Galway Formation scanline fractures could indicate

a network consisting of a higher-than-common frequency of microfractures or it might represent a sampling artifact. Our number of transgranular Category I fractures is high compared to a range of other populations (Hooker et al., 2014), but expected with our selection of samples near large fractures imaged on logs.

In the CUBO fracture population consisting of sealed microfractures and open larger fractures, the size of particular interest is the spacing of fractures that are open; that is the emergent threshold size, because kinematic apertures of this size represents the smallest open fracture size (Laubach, 2003). Quartz-lined and partially bridged fractures in the uppermost Galway sandstone cores reveal open aperture sizes of 0.028 to 0.115 mm in the F4 macrofracture set (Fig. 18). Using our population statistics, we estimate the spacing of fractures of this size to be on the order of 0.1 m (10 cm) (Ortega et al., 2006). Fractures of this width correspond to a length of 1 m based on the length aspect ratio of 10^{-3}. Although not directly comparable, this intensity estimate seems high given that BHI surveys found only six subvertical fractures over 175 m in the Galway Formation. Applying the same calculation to the F4 cumulative aperture frequency in scanline 1 (sample 8689) results in an average spacing of fractures of this width on the order of 10 m.

5.3. Integration of sidewall core-derived attributes with BHI and acoustic fracture surveys

Integration of the CUBO sidewall cores with borehole image logs for >600 m of the borehole wall offers direct borehole image verification and ground truthing of textures and features at the same image scales and positions. Judicious inclusion of the acoustic fracture survey contributes to forming conceptual fracture models that predict basic attributes of fracture systems for tens of meters beyond the borehole walls.

5.3.1. Basement section

Although basement sidewall core fractures could not be organized into systematic fracture sets, cross-scale comparison of basement sidewall core fractures to FMI and acoustic analysis fractures leads to better understanding of fracture morphologies. Intersecting fractures filled with quartz and K-feldspar form breccias in sidewall core sample 9549 (Figs. 7, 8a), which are identified in the FMI surveys at the same depth as crossing patterns formed by low-resistivity partial linear traces of moderate dip. Vertical fracture geometries observed in sample 9505.5 are consistent with subvertical fractures observed in FMI surveys, leading to an interpretation that natural fractures of both subvertical and subhorizontal orientation are recorded by the FMI resistivity measurements. Low resistivity fractures observed in FMI surveys appear as moderate to high acoustic amplitudes and velocities in the UBI survey, indicating mineral fills (Fig. 22). Fracture fill resistivity contrasts in the basement units are more complex than the Cambrian-Ordovician section, as both low and high resistivity minerals (e.g., clay minerals and quartz) fill fractures (Fig. 7b). As a result of comparison among these data sets, we find little evidence from the borehole image surveys that the detected fractures in the basement are open.

5.3.2. Cambrian-Ordovician section

Cross-scale fracture analysis of six fracture-bearing CUBO sandstone sidewall cores, from the Cambrian-Ordovician borehole section, using stereoscopic, MXCT, and SEM-CL analysis techniques, identified four subvertical fracture sets (F1 through F4) and one subhorizontal fracture set (F0) (Figs. 13, 19). As described in Section 5.2.2, one cored macrofracture of the F4 set confirmed that a prominent, E-W trending, semicontinuous, low-resistivity FMI feature is an open fracture with quartz bridges. Therefore, we interpret E-W FMI low resistivity subvertical fractures to be partially opened. At other sandstone depths, NW-striking, subvertical, low resistivity fractures exhibit a similar semicontinuous nature and have a strike orientation consistent with the F1 microfracture set; we interpret these to be natural and partially quartz bridged.

Some dolostone cores are also fractured (Table 1). The available Galway macrofracture example is filled with carbonate cement (Fig. 7b), and a matching fracture is not identified on the FMI log. The lack of electrical resistivity contrast between the dolostone host rock and a carbonate fracture fill indicates that the FMI survey data likely do not distinguish other macrofractures infilled by the primary host mineral composition (i.e., quartz or dolomite). Without the benefit of a ground-truth example, we interpret that open fractures in dolostone should be readily detected as low resistivity FMI features in CUBO.

For sandstone intervals, low resistivity FMI survey fractures that are not subvertical (e.g., not sets F1 through F4) dip moderately to the southeast. These are interpreted as drilling-induced fractures (DIF) for several reasons. 1) Fracture traces in this population all form partial sinusoids in open petal and saddle geometries (Figs. 7c, 20b,c), consistent with DIFs (Kulander et al., 1990; Aadnoy and Bell, 1998; Chatterjee and Mukherjee, 2023). 2). Fracture traces of this population occur in pairs that occur in opposite quadrants of the borehole, repeating down the borehole length covering less than 25% of the borehole circumference (Figs. 7c, 20b,c) – a common characteristic of drilling induced tensile fractures (Nelson et al., 2005). 3) All fractures in this population are isolated in the NE and SW tensile stress quadrants of the borehole (Pinilla et al., 2023), also consistent with DIFs (Fernandez-Ibanez et al., 2018). 4) The moderate SE dips (30 - 70°) of these FMI low resistivity fractures (Fig. 22a) differ from dip distributions in both the sidewall cores (Figs. 13; 19) and in the acoustic borehole survey (Fig. 24), indicating localization to the borehole face. For these four reasons, the FMI fracture data set can be filtered to identify a natural fracture population (Figs. 21c,d; 24) by excluding SE dipping, low resistivity, and partial sinusoids for the Cambrian-Ordovician borehole section.

The interpreted natural fractures (subvertical) are much more sparsely distributed through the open borehole interval after filtering (Fig. 21c,d). Open macrofractures (low resistivity) are concentrated in the dolostone of the central Tribes Hill Formation, the sandstone at the top of the Galway Formation, and in the sandstone of the upper half of Potsdam Group (Fig. 21c,d). The common high resistivity FMI features in the middle Tribes Hill Formation and at the top of the Galway Formation are likely mineral-filled macrofractures. While the FMI method does not detect macrofractures at other depths, macrofractures whose diagenetic fill is the same mineral composition as the host rock may be common elsewhere in the dolostones of the Tribes Hill, Little Falls, and Galway Formations.

The acoustic fracture survey identified far-field fractures (2.9 to 67.6 m from borehole) but no open fractures intercepting the CUBO well bore (Fig. 23). Censoring may also be caused by the vertical resolution limit of the acoustic survey (60 cm), as most subvertical fractures of the borehole wall are at or near this limit.

The acoustic data organize into two principal fracture orientation clusters, NW-SE and WSW-ENE, plus a sparse set oriented NE-SW (Fig. 22e, f). Those sets are similar to microfracture sets F1, F4, and F2, respectively (Figs. 12, 21e, f). Far-field, near vertical fractures are common in the Tribes Hill Formation dolostone, especially in a ~50 m thick zone in the middle of the formation (Fig. 24). There are notably fewer and more laterally dispersed far-field fractures in the Little Falls, Galway and Potsdam units, a tendency similar to the frequency of the FMI fractures (Fig. 24).

Collectively, the CUBO data show that intervals in Cambrian-Ordovician sedimentary rocks contain open fractures. Filtered FMI surveys and acoustic surveys for both sandstone and dolostone document steeply dipping open fracture sets in several orientations with strikes of approximately E-W and NW-SE (Fig. 22b,e,f). Additionally, steeply dipping mineral-filled fractures occur in two other orientations, NE-SW and N-S (Fig. 13), providing systematic orientations to potential mechanical discontinuities. Intermediate dipping fractures appear isolated to parts of the Tribes Hill and upper Galway Formation and do not appear to compose the main fracture framework.

For the upper sandstone member of the Galway, WSW-ENE trending Set F4 core fractures display an emergent threshold of ~0.1 mm. Cement

fill stages reveal the time sequence for the fracture sets, with F4 last, suggesting that earlier formed fractures (sets F1, F2, F3) would have experienced conditions conducive to quartz cementation for a longer time than F4. Consequently, the emergent threshold values for sets F1, F2, and F3 are likely greater than 0.1 mm (that is, fractures of the same size would be more filled). Nevertheless, the FMI set of open fractures contains many examples trending NW-SE, like F1.

There is abundant independent evidence of high fracture frequency in the Galway Formation zone with the open F4 fracture (Fig. 21c,d). The normalized cumulative aperture frequency of the F4 microfractures suggests that open fractures (of the emergent threshold aperture size) may be spaced laterally as close as 10 cm although the lack of multiple macroscopic fractures at depth within the ~30 cm wide borehole suggests scanline scaling data (~10 cm) underestimates spacing distance. Moreover, the low frequency of FMI fractures at all other depths (Fig. 21c,d) indicates that the spacing of open fractures based on samples from the uppermost Galway should not be generalized beyond that 20-m-thick sandstone unit. In the absence of open connectivity however, even this close spacing does not imply high permeability.

Sandstone core microfractures reveal narrow connections (Figs. 10,12) and, at the macrofracture scale, a similar pattern is inferred from discontinuous FMI traces for some fractures (Fig. 20c). Consequently, we interpret quartz cement reduces connectivity along individual fractures and between crossing fractures, thereby diminishing fluid flow in these fractured rocks (Olson et al., 2009; Forstner and Laubach, 2022). Although open fracture sets in the dolostones have been detected by only FMI and acoustic data, without sidewall cores that reveal in detail their properties, we anticipate that carbonate fill of those fractures, which tends to follow similar precipitation rules, would have similar impacts on open fracture continuity and fluid flow.

5.3.3. *Models of fractures in prospective geothermal reservoirs*

Prior to data integration, single-method fracture data sets generated ambiguous results (Fig. 4; Fulcher et al., 2023) because of method-specific inherent biases, resolution limits, or data truncations. For example, the acoustic survey configuration precludes detecting subhorizontal fractures and the BHI surveys include many drilling-induced fractures. Now, following analysis of fractures in the sidewall cores, data and analysis justify conceptual models for several distinct depths within the sedimentary rock column, to express considerable, albeit incomplete, understanding of the fractures. Although fracture attributes in sedimentary rocks can vary markedly on a bed-by-bed basis (e.g., Laubach, 2003), our knowledge of fracture attributes within schematic model volumes provides a baseline for future work.

For the low-grade metasedimentary basement units, the sidewall core and BHI survey data sets provide limited spatial knowledge of the metamorphic compositions, fabrics, and fractures. Consequently, we cannot produce with confidence a conceptual site fracture model for any interval in the basement.

For the sedimentary rocks, data and fracture analysis best support a conceptual model for the sandstone at the top of the Galway Formation (Fig. 25a). Regionally, the uppermost Galway sandstone stands out in contrast to the other potential sedimentary reservoirs at the CUBO site in that it is a natural gas reservoir (Smith et al., 2010). Consequently, an upper Galway model is not likely to be fully representative of most of the sedimentary rocks in the target interval. While less completely documented, sidewall core, FMI, and acoustic logs also provide preliminary insight into fracture properties for two more zones, one in upper Galway Formation dolostone (Fig. 25b) and the other in lower Potsdam Group sandstone (Fig. 25c). A lateral dimension for these schematic diagrams (Fig. 25) of 10 m is selected, in part, to express the fracture data set dimensions. For example, the BHI and sidewall core together span 0.3 m horizontally while the acoustic survey fractures are at distances of 3 to 70 m. The vertical dimension of 5 m is selected to express fractures imaged by BHI that extend 0.5 m to 2 m and yet acknowledges that the acoustic survey does not document the vertical extents of open fractures.

For the upper Galway sandstone (Fig. 25a), microfracture scaling relations forecast some open fracture sets will be spaced on the order of 1 m apart without clustering. Microfracture data and BHI and acoustic fracture surveys indicate fracture sets F1 (NW-SE) and F4 (WSW-ENE) are most likely to be open (dash lines) and yet zones of narrower aperture are likely filled with quartz cement (solid lines) (Fig. 25a). Fracture data sets in this study also show the upper Galway sandstone contains two other sets of near-vertical macrofractures (F2, F3) that may be entirely filled with quartz cement. The FMI surveys show subvertical fractures cross-cut bed boundaries for >1 m, which leads to the depiction of some fractures with vertical extents of a few meters.

For the Galway dolostone (Fig. 25b), sparse core and FMI subvertical fractures strike dominantly ENE, N, and NW while the acoustic survey indicates F1 and F4 fracture orientations are open (Fig. 24). The FMI data likely underestimates the abundance of dolomite-filled fractures in dolostone host rock (Fig. 24) due to the low resistivity contrast between mineral infills and the host rock.

For the Potsdam sandstone model (Fig. 25c), mineral-filled subvertical fractures in all four sets occur and filled subhorizontal fractures are moderately abundant. Like the Galway sandstone, sets F1 and F4 are the ones that FMI analysis indicates to include open examples. Significant differences relative to the upper Galway Formation (Fig. 25a) are that Potsdam open fracture traces are less abundant in the borehole wall yet more abundant at tens-of-meter distances away from the wellbore, and there is no evidence of vertical continuity across bedding planes.

5.4. *Comparison of CUBO fracture characteristics to fractures at other sites*

This study characterizes and analyzes fractures within a column of rock roughly 150 m wide with the CUBO borehole at its center. Comprehensive EGS reservoir target evaluation requires a larger spatial fracture data set. Comparisons to other geologically comparable sites offer qualitative opportunities to assess fracture system properties at broader dimensions, whether from perspectives of fracture permeability changes with depth, the mineralogy of host rock and fracture fills, or structural context. Such comparisons can improve understanding of regional variations of porosity, permeability, and transmissivity.

One strategy to extend inferences about fracture attributes at broader dimensions is to consider distant (>1 km) boreholes intercepting the same formation or lithologic types with similar structures and fractures. Borehole to borehole comparisons allow for direct fracture comparison at depth, but spatial analysis of fracture systems is generally limited due to a finite number of boreholes, low frequency of available data, and artifacts caused by the drilling process (e.g., DIFs, geophysical surveying resolution, mechanical errors etc.).

Outcrop studies are another strategy for inferring fracture parameters, allowing multi-scale spatial analysis of fractures in 2- and 3-dimensional frameworks. Outcrop fracture analysis can provide fracture parameters not measurable in a borehole such as fracture connectivity (Sanderson and Nixon, 2015; Procter and Sanderson, 2018), length and height distributions (Ukar et al., 2019; Forstner and Laubach, 2022), and susceptibility to closure (stiffness) (Hillis, 1998). Outcrops relevant to fractured reservoir targets are those whose brittle structures are fundamentally similar (Sanderson David, 2016), and whose structural and diagenetic histories are demonstrably similar (Ukar et al., 2019).

For the Allegheny Plateau, given the small number of boreholes intercepting regional basement units and the inadequate understanding of natural fractures in the CUBO basement rocks, knowledge of fractures in appropriate outcrop analog systems would be of high value. Valentino et al. (2024) proposed that Neoproterozoic basins in southeastern Pennsylvania, New Jersey, and Virginia are analogs to low-grade metamorphic rocks at the CUBO site in Ithaca NY. However, outcrops of those rocks are unlikely to be appropriate analogues for the subsurface fracture system, given that the tectonic regimes of the CUBO site

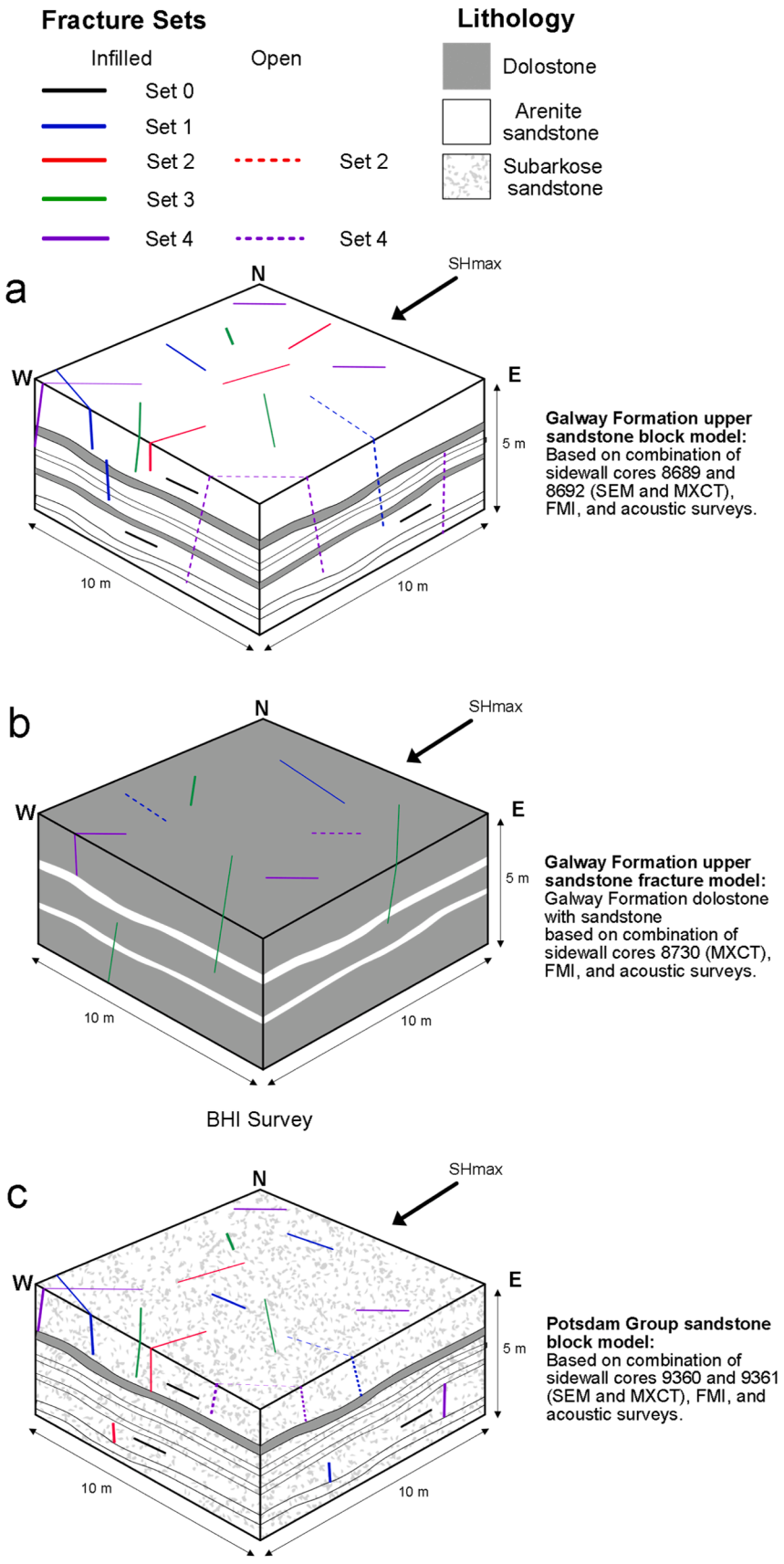

Fig. 25. Conceptual site fracture models (CSFM) based on integrated fracture data sets for sedimentary rocks of three depth intervals. a) Upper member of Cambrian Galway Formation, dominated by sandstone (white) with secondary dolostone (gray). b) Interval in upper Galway Formation dominated by dolostone with minor sandstones. c) Potsdam Formation sandstone with local dolostone beds.

and those sites have differed markedly throughout the last ~470 million years.

For the CUBO site, the Auburn Geothermal well located 56 km to the north provides the closest relevant subsurface data set (Fig. 1). The Auburn Well produced geothermal heat for several years from natural fracture flow in Cambrian formations at approximately 1,000 m shallower depth than similar CUBO reservoir targets. The acoustic borehole televiewer survey (e.g., UBI log) of the Auburn geothermal well provides the only available and comparable subsurface fracture data set for Cambrian target reservoir formations within 200 km distance of CUBO. Within the Auburn geothermal well, seven open subvertical ENE striking fractures averaging a dip of 71.5° are identified in the Little Falls Formation, Galway Formation, and Potsdam Group (Lynch and Castor, 1983; Plumb and Hickman, 1985). Four open, subhorizontal northerly dipping fractures (5°- 8°) are also identified. Subvertical fractures identified in the Auburn geothermal well are compatible with orientation of the CUBO F4 microfractures – signifying the F4 fracture set exists north of the CUBO site.

At a larger regional scale, Elliott et al. (2025) provides detailed knowledge of fracture and diagenetic attributes of Potsdam Group outcrops located 350 km northeast of the site near Altona, New York (Fig. 1). Orientation and sequence of CUBO sidewall core fracture sets F1, F2, and F4 are consistent with macroscopic Potsdam Group outcrop fracture sets A (NNW), B (NE), and D (ENE) described by Elliott et al. (2025). The four sets of Potsdam Group outcrop fractures are quartz lined and, for smaller aperture examples, quartz- filled, with an emergent threshold aperture of 0.05-0.1 mm (Elliott et al., 2025). These emergent threshold values are similar to those in the upper member of the Galway Formation intercepted by CUBO borehole. A caveat to use of this site as an analog is that it is inferred to not have been as deeply buried nor to have experienced temperatures as high as those at CUBO (Elliott et al., 2025). Moreover, the Potsdam Group in the Altona area is located within the Neoproterozoic to Mesozoic tectonic rift regime of the Ottawa embayment (O'Brien and van der Pluijm, 2012; Sasseville et al., 2012; Tremblay et al., 2013), hence it experienced conditions producing or altering fractures that did not occur at the central New York CUBO site.

Overlying the Silurian zone of structural decoupling are fractures in widespread Devonian outcrops of the Allegheny Plateau across central New York State, which have been extensively studied. Across central New York these abundant open subvertical fractures are categorized as regional joints (Fig. 5) (Sheldon, 1912; Parker, 1942; Engelder and Sbar, 1977; Engelder and Geiser, 1979, 1980; Lash and Engelder, 2009). Open subvertical fractures sets Ia (N-S), Ib (NW-SE), and II (ENE-WSW) in Devonian strata of the Finger Lakes area (Engelder and Geiser, 1980) (Fig. 5) are concordant with the CUBO fracture sets F3, F1, and F4 respectively (Fig. 25c). Only the NE-trending F2 set is not represented among the Devonian fractures.

Across central New York, some fractures are specifically considered to align with basement faults rather than be simple joints, and are oriented N-S and WSW-ENE as structural lineament bundles defined by Jacobi (2002). These structural lineament bundles show orientation agreement with fracture sets F3 and F4, respectively. Orientations of interpreted acoustic survey fractures agree with regional fracture sets Ib and II of Engelder and Geiser (1980) (Fig. 5). However, the dominance of WSW-ENE oriented fractures interpreted from the CUBO acoustic survey (Fig. 22f) is higher than intensities observed for local Devonian outcrops (Parker, 1942; Engelder and Geiser, 1979, 1980).

We assume that fractures in Devonian rocks developed at significantly lower temperatures compared to fractures in the deeper Cambrian targets (>2,000 m) based on temperature differences on the order of 50°C in the early Mesozoic (e.g., 200-300°C for Cambrian units and 150-200°C for Devonian units Repetski et al., 2008; Shorten and Fitzgerald, 2019) and measured today (e.g., >74°C for Cambrian and; <30°C for Devonian; Fulton et al., 2024). As a result, fractures in Devonian rocks would have experienced quite different rates of mineral growth, which means that even for units of similar lithology (e.g., sandstone) there would be non-analogous apertures for open fractures and connectivities. Consequently, the Devonian rocks are not suitable reservoir analogues.

Agreement of CUBO fractures (micro to macroscopic) with macrofractures observed in overlying Devonian outcrops (F1, F3, and F4) and in Cambrian strata of the Auburn geothermal well (F0 and F4) suggests that systematic brittle deformation exists both below and above the Salina décollement over 150 km north of the Allegheny structural front. Despite the different thermal and burial conditions and given the extremely sparse fracture data for Cambrian-lowermost Ordovician strata except at CUBO, it may be a useful starting point to apply at other Allegheny Plateau DDU geothermal exploration sites some insight derived from the widely available Devonian fracture data.

6. Conclusions

In New York, previous knowledge of basement, Cambrian, and Ordovician units indicated these rocks have low porosity and permeability. Consequently, the Cornell University ESH project anticipated feasibility of DDU geothermal heat production would require natural or stimulated fracture flow, yet there existed almost no insight to fractures for these strata. Sidewall cores from the CUBO exploration well confirm potential reservoir targets have low porosity and, therefore, a successful DDU geothermal reservoir will require flow through connected fractures.

Five basement sidewall cores and 90 m of borehole image data document metamorphic fabrics and fractures in greenschist phyllites of the Cayuta Formation. Identified mineral-filled breccia fractures in sidewall cores may postdate metamorphism. The observed sidewall core metamorphic and structural features combined with features revealed by BHI surveys show that abundant mineral infilled macrofractures are superimposed on metamorphic fabrics. Core and image log data found no unambiguous evidence of open fractures in the Cayuta Formation of CUBO.

Nineteen oriented sidewall cores in Cambro-Ordovician strata provide mineral-filled microfractures and sparse macrofractures, whose preferred strike directions and crossing relations document multiple systematic sets of vertical fractures. Sidewall core interception of an FMI-imaged macroscopic fracture identified the FMI survey attributes that correspond to open fractures. This ground-truthed example underpins increased confidence in discrimination between natural fractures and drilling-induced fractures in borehole image logs. For the Cambrian-Ordovician open borehole section, integration of sidewall core fracture data with BHI and acoustic surveys led to recognition of a fracture system composed of subvertical and subhorizontal fractures.

Filtering of drilling-induced fractures for the full ~600 m thickness of sedimentary rocks identified three zones of abundant, open, vertical fractures. These occur within a thick interval of the Tribes Hill Formation dolostones, a 20-m-thick sandstone at the top of the Galway Formation, and a thin interval in the upper part of the Potsdam Group sandstones.

Conceptual fracture models emerge for three depths in the Cambrian-Ordovician section: the uppermost Galway sandstone, an interval of dolostone is the Galway Formation, and the middle Potsdam Group. In the uppermost sandstone member of the Cambrian Galway Formation, fractures are closely spaced and four intersecting sets of subvertical fractures also intersect numerous subhorizontal bedding planes. Among the natural fractures, the FMI and acoustic analysis indicate some fractures in sets F1 (WSW-ENE), F4 (WSW-ENE), and lesser F2 (NE-SW) are open distally from the open borehole section.

Microfracture orientations for Cambrian-Ordovician sandstones in and near CUBO agree well with previously identified regional surface (Devonian and Cambrian units) and subsurface (Cambrian-Ordovician units) fracture orientations from the Auburn Geothermal Well. This similarity implies the existence of fractures in Devonian strata of the

Allegheny Plateau are not strictly bounded by the Salina décollement and extend at depth to the base of the Cambrian. Among available choices with extensive data for fracture properties, outcrops of the Potsdam and Beekmantown Group around the margins of the Adirondack Mountains are the closest analog for a potential sandstone geothermal reservoir below Cornell University. Thus far no suitable outcrop analog for fracture characteristics of the Cayuta Formation metamorphic basement has been identified.

Our study shows that, for geothermal targets in sedimentary rocks, analysis of fracture orientation, number of sets, and abundance can be conducted with relatively inexpensive wireline sidewall core, complementing and calibrating BHI surveys and acoustic fracture analysis. Comparisons to outcrop analogs enhance understanding of potential reservoirs beyond the spatial limits of these data sets. Sidewall cores offer in-situ samples that in this example can substitute for conventional large diameter core and allow expedited data integration with BHI surveys. In future reservoir analyses with sidewall cores, incorporation of optimized MXCT analyses (e.g., higher pixel resolution, machine learning) with SEM image data could bridge observations of different spatial scales, leading potentially to evaluation within sidewall cores of fracture attributes that are usually only measured in outcrop (e.g., connectivity).

CRediT authorship contribution statement

Sean A. Fulcher: Writing – review & editing, Writing – original draft, Visualization, Methodology, Investigation, Formal analysis, Data curation, Conceptualization. **Teresa E. Jordan:** Writing – review & editing, Supervision, Investigation, Funding acquisition, Data curation. **Stephen E. Laubach:** Writing – review & editing, Supervision, Methodology, Funding acquisition, Conceptualization. **Sara J. Elliott:** Writing – review & editing, Formal analysis, Data curation. **Valeria Nogales Herrera:** Writing – review & editing, Formal analysis.

Declaration of competing interest

The authors declare the following financial interests/personal relationships which may be considered as potential competing interests:

Sean Alexander Fulcher reports financial support was provided by US Department of Energy. If there are other authors, they declare that they have no known competing financial interests or personal relationships that could have appeared to influence the work reported in this paper.

Acknowledgements

Sidewall core and log collection and analysis was supported by the U. S. Department of Energy's Office of Energy Efficiency and Renewable Energy (EERE) under Geothermal Technologies Office Award Number DE-EE0009255. Microstructural imaging and analysis were supported by grant DE-SC0022968 from Chemical Sciences, Geosciences and Biosciences Division, Office of Basic Energy Sciences, Office of Science, U.S. Department of Energy (DOE) (Laubach) and by Cornell University. We acknowledge additional support from the Fracture Research and Application Consortium (FRAC) and Albert W. & Alice M. Weeks Centennial Professorship in Geological Sciences (Laubach) and contributions from members of the Cornell Earth Source Heat project team. Special thanks to Edgar Velez Arteaga of SLB for providing insights and guidance with far-field acoustic fracture analysis and Richard A. Plumb for discussion and to Repsol Technology Lab for providing MXCT and geomechanical analyses. We are grateful to Pedro Vieira de Luca, Daniela Pinilla, and Burak Erdinc for image log, acoustic data analysis, and fracture interpretation. Special thanks is given to Lawrence Cathles for manuscript reviews.

Appendix A1. Stratigraphy and rock types at CUBO

The deepest sedimentary geothermal ESH reservoir target is the Potsdam Group (2,818 to 2,865 m), consisting of Cambrian transgressive siliciclastic units that unconformably overlie Precambrian basement (~550 Ma non-conformity) (Landing, 2007; Lowe et al., 2015; Lowe et al., 2017). The sandstone-dominated Potsdam Group regionally consists of three formations in ascending order; the Altona, Ausable, and Keeseville Formations. The Middle Cambrian Altona Formation locally comprises reddish mudstone with lesser carbonate beds of marine origin (Landing et al., 2009). The Ausable Formation, equivalent to the Covey Hill Formation in Ontario and Quebec (Sanford and Arnott, 2010), consists of light gray to pale pink medium- to coarse- sand and pebbly arkosic sandstone (Fisher, 1968). Thickness ranges from 300 to over 400 m southwest of Montreal (Sanford and Arnott, 2010), but at the CUBO site this unit is interpretated to be only 31 m thick.

The Keeseville Formation consists of buff to white silica-cemented super mature quartz arenite hosting $\leq$ 5% detrital feldspar. Quartzite clasts and cobble-boulder conglomerates with a quartz arenite matrix are present locally with lesser mudstone and dolostone (Sanford and Arnott, 2010; Lowe et al., 2017). The Keeseville Formation unconformably overlies the Ausable Formation in northern New York, but also locally overlies Precambrian basement in the Ottawa Embayment (Nepean Formation) and Quebec Basin which is called Cairnside Formation. The Keeseville is interpreted as 10 meters thick in the CUBO well.

Situated conformably above the Potsdam Group is the Upper Cambrian to lower Ordovician Beekmantown Group comprising Galway, Little Falls, and Tribes Hill Formations. Cambrian-age Galway Formation is regionally 10-500 m thick with interbedded dolostones and sandstones (Smith et al., 2010). Galway Formation subdivisions for the south-central Finger Lakes region includes three members in ascending order: Vespa, Yellowjacket, and the Rose Run (Al Aswad, 2019). The lowest quartz rich ('clean') sandstones of the Vespa Member are overlain by interbedded dolomite and sandstones of the Yellowjacket Member (Smith et al., 2010). An 18-to-76-m thick arenite, known as the Rose Run Member, locally forms the top of the Galway Formation and has a 9-meter intercept in the CUBO well. This unit is equivalent to the Rose Run Formation in Ohio (Smith et al., 2010). The remaining 166 meters of Galway Formation intercept in the CUBO well contain Vespa and Yellowjacket members.

Overlying the Galway Formation is the Cambrian Little Falls Formation. Regionally, this is a 125-m thick succession of interbedded sandstones and dolostone that hosts algal stromatolites. A 155 m thick interval of fine-grained sandstone and sandy dolomite comprise the Little Falls Formation in the CUBO well (Fig. 3). The Little Falls Formation intercept in the CUBO site is equivalent to Unit B in the type section by Zenger (1976), Fulcher et al. (2023).

The shallowest sedimentary geothermal target is the Tribes Hill Formation, a Lower Ordovician dolostone-limestone deposited in a shallow marine environment defined regionally by four members in ascending order: the Fort Johnson, Palatine Bridge, Wolf Hollow, and Fonda. Within the CUBO well, a 138 m thick interval containing a shaley limestone unit overlies a sandy dolomitic limestone. We interpret this interval to correlate with the Palatine Bridge and the Fort Johnson Members of the Tribes Hill Formation (Fig. 3) (Fulcher et al., 2023).

Appendix B2. Core orientation and petrography

B2.1 Sidewall sampling

Sidewall core depth locations were selected after reviewing initial BHI surveys to target specific lithological and structural features (e.g., textural changes, bedforms, and fractures). Coring location selection benefited from having two image log collections. If only one is planned, cores need to be collected *before* the log run so the core holes can be imaged. Sample names (e.g., '9459") correspond to depths in feet, the unit of wireline log measurement.

The nominal core length is based on the dimension of the XL-Rock tool core barrel sample receptacle (63.5 mm), but the recovered cores lengths vary depending on formation and drilling conditions. Sidewall core recovery length percentages ranged from 66 to 107% (Table 1) except for sample 9503, which was rubble and is excluded from this study. The lithology with the highest core recovery (core length) is quartz arenite. Of these cores, a subset that contains visible fractures was selected for microfracture analysis (Table 1). The visibility of macroscopic fractures was based on core inspection and MXCT evaluation. We took this step of high-grading the samples to reduce the number subject to image analysis—a cost saving—and to obtain results in a rapid time frame (c. weeks) to allow use in wellsite decision making.

During a sidewall core sampling, each core is extracted from the formation by breaking off the core by tilting the core barrel. Drilling and tilting the core barrel creates a distinctive feature plane on the formation side of the core. Identifying core top or 'up' orientation depends on observing the drilled borehole face end (BHF) and broken off formation face end (FF) of sidewall cores (Laubach and Doherty, 1999). The BHF end preserves part of the wellbore wall that can be used to identify the angle of the core axis relative to the wellbore wall and thus refine the core azimuth. The FF preserves delicate features caused by core breakage, similar to features on the end of a broke stick of chalk and thus specifies core tops. It is imperative to ensure the core ends are preserved and not cut off as these are the primary features for orientation. More common uses of sidewall cores, such as geomechanical testing, require flat sidewall core ends and the normal procedure is to cut these ends off. Liaison with the core contractor is needed to prevent this from happening.

Owing to the need to preserve these core orientation features, we described sidewall cores in the field (well site) and packaged cores in protective sleeves to keep them intact during transport. Upon laboratory receipt, each sidewall core was inspected and cleaned using deionized water and fine nylon brushes to remove surficial drilling mud and to keep delicate core ends and fracture fills intact. During this process, each sidewall core sample was placed in a perforated cylindrical core holder to retain its physical integrity during additional cleaning, imaging, photographic documentation, orienting, and logging. This step was immediately followed by documenting core top and azimuth features.

B2.2 Sidewall core top and azimuth orientation

Core ends representing both the BHF and FF contain essential information about which direction in the core is 'up' (the top direction), which is required for correctly inferring fracture strike. The first sidewall core orientation indicator occurs in the wireline tool recovery receptacle, where sample identification tags are placed on top of the BHF, demarking the borehole wall. Both core ends need to be field-described to aid orientation accuracy.

A top indicator is the hyperbolic parabola shape of the borehole core end (e.g., saddle shape) caused by the cylindrical full diameter wellbore geometry intercepted by the sidewall core (Figs. 5b,d,f). The saddle shape has two opposed points that are the shortest dimension of the core; these mark the top-bottom axis but do not distinguish which end (sidewall core side) is the top or bottom. Uni-directional striping caused by the diamond sidewall coring bit can also help determine the borehole wall end of the sidewall core if the BHF is ambiguous.

Core tops and bottoms (i.e., vertical orientations) are identified using the FF side where a break angle during core extraction is caused by the SLB XL-Rock wireline tool cleaving the core as the tool is tilted in a top-down direction to form a cured fracture dipping ~60-70° to the core axis. The apical trace of the induced fracture marks the core top (Fig. 5c). Delicate and easily damaged cleaved ends are best described prior to other core processing. Orientations of top and bottom of the core can in some cases be determined by comparing sedimentary and structural features in core with formation features imaged in the FMI and UBI surveys. Any sedimentary top indicators should also be noted.

Azimuthal core orientations are obtained by measuring the centerline of the sidewall borehole imaged by a post-coring FMI survey. Although inspection of the image log may suffice, for greater precision we obtained the azimuth using AspenTech Geolog software. The resulting core azimuth orientations are about as accurate as the image log (±2°) (Schlumberger, 2004).

B2.3 Petrography/SEM CL

For host-rock composition analysis, mineral point counts were completed using scanning electron microscope images that combine SEM-CL and energy dispersive spectrometry (EDS) (semi-quantitative composition maps) and transmitted light images to discriminate grain and cement abundances. Large-area (>5 mm^2) automated mosaics were constructed of selected areas of carbon-coated (15 nm), oriented, polished thin sections. The mosaicked images were produced by a Zeiss Sigma Field Emission Scanning Electron Microscope with Gatan MonoCL4 cathodoluminescence detector, an Oxford X-max 50 Silicon Drift X-ray EDS detector, and a variable pressure secondary electron detector (VPSE) for charge-contrast imaging (CCI). SEM-CL analysis used 6 kV, a 120 μm aperture, and a 150 μs dwell time yielding images with spatial resolution of ~100-350 nm per pixel depending on magnification. EDS imaging used 10 kV and a 200 μs dwell time.

We documented composition using conventional transmitted light methods and correlative image stacks (SEM-CL and EDS) in JMicrovision® using a grid pattern, where varying image layer transparency allowed quantitative determination of mineral composition or porosity at each grid point at sub-micron scale. A minimum of 700 points per imaged area produces 99% confidence that all mineral constituents were counted within 95% of their true proportions.

Image mosaics were designed to maximize sampling of subvertical fractures so at least one section was cut in the plane of bedding (~horizontal; plan view) (Gomez and Laubach, 2006). Microfracture orientation involved orienting each bed-parallel SEM-CL map to its true azimuth (Table 2). Each long, narrow SEM-CL map constitutes a scanline. Two SEM-CL bed-parallel scanline maps were completed and analyzed for samples 8689 and 8692 (Table 2). Oriented SEM-CL maps were overlapped digitally, forming a 2D transect map that allowed microfracture trace orientation comparison between multiple SEM-CL maps of each Galway Formation sample. Microfracture traces were digitally traced and categorized using classification criteria and strike orientations.

Microfracture populations were mapped in long, narrow image mosaics (1 × 30 mm) collected primarily using multiple rows of panchromatic SEM-CL images (gray-scale intensities) with magnifications ranging from 175 × to 250 × . Quartz luminescence intensities and colors from SEM-CL imaging reflect trace chemicals and mineral lattice structural defects (e.g., Götze et al., 2001), enabling identification of different quartz growth zones and generations. We classified microfractures according to their crosscutting relations with grains and cement (Laubach, 1997; Laubach and Gale, 2006) and measured and analyzed size-scaling statistics (Gomez and Laubach, 2006; Ortega et al., 2006) and spatial arrangement (Marrett et al., 2018)

using standard methods. Microfracture analysis using SEM techniques in this study focused on fracture-bearing sandstones from the Potsdam Group and Galway Formation to allow comparable mineralogical and deformation characteristics at different depths. Similarly, fracture and SEM analysis of limited basement samples were focused on lithology and fracture morphologies to validate BHI surveys.

Appendix C3. Acoustic fracture survey analysis

Acoustic waveform analysis for near and far-field factures is not without caveats and uncertainties. Overlapping effects from intersecting open fractures may occur and therefore complicate waveform fracture analysis for individual fractures or fracture sets. Moreover, borehole washouts, rugosity, casing irregularities, or heterogeneous fluids can distort wave propagation, creating artifacts unrelated to fractures (Kimball and Endo, 1998; Lehne et al., 1999).

Borehole breakouts were present throughout the open borehole section and most concentrated in the basement complex section (Pinilla et al., 2023). SLB applied corrections to wave slowness to reduce artifacts caused by borehole rugosity and eccentricity. The process involves first completing wave path modelling where the non-axial tool position and oblique wavefronts are determined and corrections to slowness are made based on actual wave travel paths. Additional frequency-dispersion corrections to account for differences between flexural mode phase velocity and formation velocity were also applied where applicable. The final step involves inversion modelling of the formation slowness that best fits observed data under the known borehole geometry. Inversion models of the original and corrected wave slowness are compared against tolerance criteria in Fig. C3-1. Track parameters descriptions and abbreviations are listed in Table C3-1. Differences between the measured (DTSH_FAST_R) and compensated shear slowness (DTSH_SLOW_DDBHC) were within tolerances in the Cambrian-Ordovician open borehole section (Fig. C3-1). Correction tolerances between measured and compensated shear slowness were exceeded in portions of the basement complex (Fig. C3-1). Moreover, slowness anisotropy (SLOANI) increased significantly in the basement complex leading to higher uncertainty of identifying natural fractures (Fig. C3-1). Therefore, interpreted fractures in the basement portion are considered to have a higher degree of uncertainty.

Table C3-1
List of measured or calculated sonic scanner parameters in the CUBO well as displayed in Fig. C3-1. Parameters with description, units, abbreviation, and track position are listed.

Parameter	Track	Abbreviation	Units
Cable tension	1	TENS	lbf
Measured depth	1	MD	ft
Delta maximum and minimum cross energy	1	XENE	unitless
Gamma Ray	2	GR_EDTC	gAPI
Memorized hole azimuth	2	HAZIM	deg
Memorized sonde deviation	2	SDEVM	deg
Bit size	3	BS	in
PPC1 hole diameter 1	3	HD1_PPC1	in
PPC1 hole diameter 2	3	HD2_PPC1	in
Fast shear azimuth (NAZ REF90) - overall - swapped	4	FSA_NAZ	deg
Fast shear azimuth error minus (NAZ REF90) - swapped	4	FSA_NAZ_ERRMINUS	deg
Fast shear azimuth error plus (NAZ REF90) - swapped	4	FSA_NAZ_ERRPLUS	deg
Fast shear azimuth in anisotropic zones	4	FSA_NAZ_IN	deg
Delta compressional slowness	6	DTCO_MF_R	us/ft
Delta fast shear slowness	6	DTSH_FAST_R	us/ft
Delta shear slowness compensated	6	DTSH_SLOW_DDBHC	us/ft
Slowness anisotropy	6	SLOANI	%
Time-based anisotropy	6	TIMANI	%
Poisson's ratio	7	PR_FAST	unitless
VP/VS ratio from fast shear	7	VPVS_FAST	unitless
Time window begin - packed	8	TW_B_L6	us
Time window end - packed	8	TW_E_L6	us
Slowness projection (SPR) from the monopole far-receiver array	9	SPR_MF_R	us/ft
Slowness projection (SPR) fast shear slowness	10	SPR_FAST_R	us/ft
Slowness-frequency analysis (SFA) fast shear slowness shear polarization	11	SFA_FAST_R	us/ft
Slowness projection (SPR) slow shear slowness receiver array	12	SPR_SLOW_R	us/ft
Slowness-frequency analysis (SFA) slow shear polarization	13	SFA_SLOW_R	us/ft

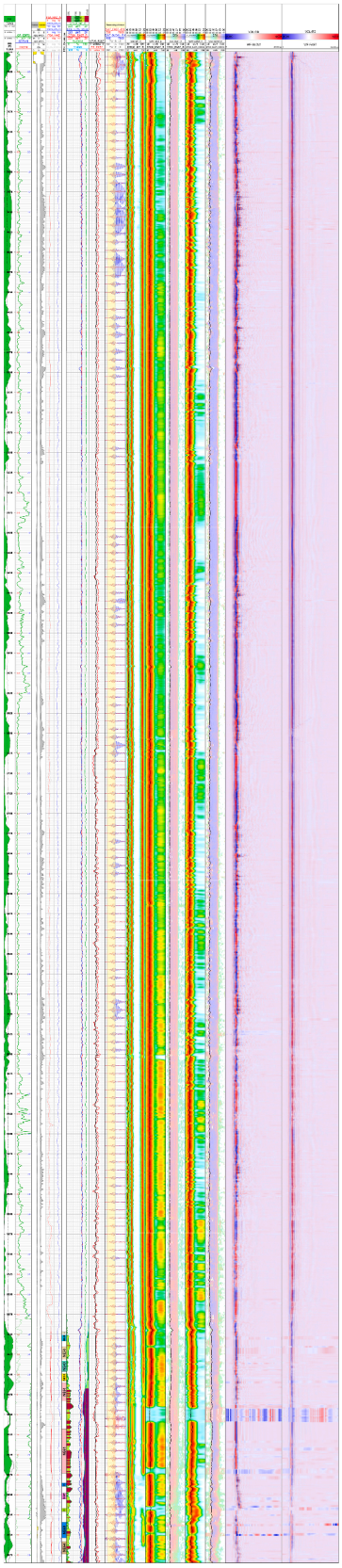

Fig. C3-1. Plot of measured compressional shear slowness with additional borehole data such as gamma ray, caliper, and cable tension. Waveforms of slow and fast shear are also shown (WF-SLOW and WF-FAST). Table C3-1 provides abbreviations of parameters shown on individual tracks.

Data availability

Microfracture data is provided. BHI and acoustic survey data will be archived in public databases.

References

Aadnoy, B.S., Bell, J.S., 1998. Classification of drilling-induced fractures and their relationship to in-situ stress directions. Log Anal. 39 (06), 27–42.

Ajdukiewicz, J.M., Larese, R.E., 2012. How clay grain coats inhibit quartz cement and preserve porosity in deeply buried sandstones: observations and experiments. AAPG Bull. 96 (11), 2091–2119. https://doi.org/10.1306/02211211075.

Al Aswad, J. A. A., 2019, A stratigraphic and petrophysical study of in-situ geothermal reservoir quality of the Canbro-Ordovician strata in the subsurface at Cornell University, Ithaca, New York [MSc.: Cornell University.

Allmendinger, R.W., Cardozo, N., Fisher, D.M., 2011. Structural Geology Algorithms: Vectors and Tensors. Cambridge University Press, Cambridge.

Anders, M.H., Laubach, S.E., Scholz, C.H., 2014. Microfractures: a review. J. Struct. Geol. 69, 377–394. https://doi.org/10.1016/j.jsg.2014.05.011.

Barton, C.A., Zoback, M.D., 2002. Discrimination of natural fractures from drilling-induced wellbore failures in wellbore image data—implications for reservoir permeability. SPE Reserv. Eval. Eng. 5 (03), 249–254. https://doi.org/10.2118/78599-PA.

Bennett, N.N., 2019. 3D slowness time coherence for sonic imaging. Geophysics 84 (5), D179–D189. https://doi.org/10.1190/geo2018-0077.1.

Biot, M.A., 1956a. Theory of propagation of elastic waves in a fluid-saturated porous solid. II. Higher frequency range. J. Acoust. Soc. Am. 28 (2), 179–191. https://doi.org/10.1121/1.1908241.

Biot, M.A., 1956b. Theory of propagation of elastic waves in a fluid-saturated porous solid. I. low-frequency range. J. Acoust. Soc. Am. 28 (2), 168–178. https://doi.org/10.1121/1.1908239.

Blackwell, D., Richards, M., Frone, Z., Batir, J., Ruzo, A., Dingwall, R., Williams, M., 2011. Temperature-at-depth maps for the conterminous US and geothermal resource estimates. Res. Counc. Trans 35, 1545–1550.

Bloch, S., Lander, R.H., Bonnell, L.M., 2002. Anomalously high porosity and permeability in deeply buried sandstone reservoirs: origin and predictability. AAPG Bull. 86, 301–328.

Bolshakov, A., Patterson, D., Lan, C., 2011. Deep fracture imaging around the wellbore using dipole acoustic logging. In: SPE Annual Technical Conference and Exhibition p. SPE-146769-MS.

Boullier, A.-M., Robert, F., 1992. Palaeoseismic events recorded in Archaean gold-quartz vein networks, Val d'Or, Abitibi, Quebec, Canada. J. Struct. Geol. 14 (2), 161–179. https://doi.org/10.1016/0191-8141(92)90054-Z.

Brace, W.F., 1980. Permeability of crystalline and argillaceous rocks. Int. J. Rock Mech. Min. Sci. Geomech. Abstr. 17 (5), 241–251. https://doi.org/10.1016/0148-9062(80)90807-4.

Cao, M., Hirose, S., Sharma, M.M., 2022. Factors controlling the formation of complex fracture networks in naturally fractured geothermal reservoirs. J. Pet. Sci. Eng. 208, 109642. https://doi.org/10.1016/j.petrol.2021.109642.

Chatterjee, S., Mukherjee, S., 2023. Review on drilling-induced fractures in drill cores. Mar. Pet. Geol. 151, 106089. https://doi.org/10.1016/j.marpetgeo.2022.106089.

Dutton, S. P., Clift, S. J., Hamilton, D. S., Hamlin, H. S., Hentz, T. F., Howard, W. E., Akhter, M. S., and Laubach, S. E., 1993, Major low-permeability-sandstone gas reservoirs in the continental United States: The University of Texas at Austin, Bureau of Economic Geology, Report of Investigations No. 211. p. 221.

Ehrenberg, S.N., Nadeau, P.H., Steen, Ø., 2009. Petroleum reservoir porosity versus depth: influence of geological age. AAPG Bull. 93 (10), 1281–1296. https://doi.org/10.1306/06120908163.

Elliott, S.J., Forstner, S.R., Wang, Q., Corrêa, R., Shakiba, M., Fulcher, S.A., Hebel, N.J., Lee, B.T., Tirmizi, S.T., Hooker, J.N., Fall, A., Olson, J.E., Laubach, S.E., 2025. Diagenesis is key to unlocking outcrop fracture data suitable for quantitative extrapolation to geothermal targets. Front. Earth Sci. 13, 1–38. https://doi.org/10.3389/feart.2025.1545052.

Engelder, T., 1985. Loading paths to joint propagation during a tectonic cycle: an example from the Appalachian Plateau, U.S.A. J. Struct. Geol. 7 (3), 459–476. https://doi.org/10.1016/0191-8141(85)90049-5.

Engelder, T., Geiser, P., 1979. The relationship between pencil cleavage and lateral shortening within the Devonian section of the Appalachian Plateau, New York. Geology 7 (9), 460–464. https://doi.org/10.1130/0091-7613(1979)7<460:TRBPCA>2.0.CO;2.

Engelder, T., Geiser, P., 1980. On the use of regional joint sets as trajectories of paleostress fields during the development of the Appalachian Plateau, New York. J. Geophys. Res.: Solid Earth 85 (B11), 6319–6341. https://doi.org/10.1029/JB085iB11p06319.

Engelder, T., Sbar, M.L., 1977. The relationship between in-situ strain relaxation and outcrop fractures in the Potsdam Sandstone, Alexandria Bay, New York. Pure Appl. Geophys. 115 (1), 41–55. https://doi.org/10.1007/BF01637096.

Fercho, S., Matson, G., McConville, E., Rhodes, G., Jordan, R., Norbeck, J., 2023. Geology, state of stress, and heat in place for a horizontal well geothermal development project at Blue Mountain, Nevada. In: Proceedings, 48th Workshop on Geothermal Reservoir Engineering, Volume SGP-TR-224, p. 16.

Fernandez-Ibanez, F., DeGraff, J.M., Ibrayev, F., 2018. Integrating borehole image logs with core; a method to enhance subsurface fracture characterization. AAPG Bull. 102 (6), 1067–1090. https://doi.org/10.1306/0726171609317002.

Fisher, D.W., 1968. Geology of the Plattsburgh and Rouses Point. Vermont Geological Survey, New York - Vermont, quadrangles, p. 51.

Forstner, S.R., Corrêa, R., Wang, Q., Laubach, S.E., 2024. Fracture length data for geothermal applications. In: Gill, C.E., Goffey, G., Underhill, J.R. (Eds.), Powering the Energy Transition Through Subsurface Collaboration, 1. Geological Society of London, Energy Geoscience Conference Series. https://doi.org/10.1144/egc1-2024-17.

Forstner, S.R., Laubach, S.E., 2022. Scale-dependent fracture networks. J. Struct. Geol. 165, 104748. https://doi.org/10.1016/j.jsg.2022.104748.

Freiburg, J.T., Amer, M., Henkel, K., Wemmer, K., Grathoff, G.H., 2022. Illitization in the Mt. Simon Sandstone, Illinois Basin, USA: implications for carbon dioxide storage. Mar. Pet. Geol. 146, 105963. https://doi.org/10.1016/j.marpetgeo.2022.105963.

Freiburg, J.T., Ritzi, R.W., Kehoe, K.S., 2016. Depositional and diagenetic controls on anomalously high porosity within a deeply buried CO2 storage reservoir—the Cambrian Mt. Simon Sandstone, Illinois Basin, USA. Int. J. Greenh. Gas Control 55, 42–54. https://doi.org/10.1016/j.ijggc.2016.11.005.

Fulcher, S.A., Pinilla, D., Jordan, T.E., Fulton, P.M., Henrique Viera de Luca, P., 2023. Fracture network characterization and permeability for direct-use geothermal energy – Cornell University Borehole Observatory ESH No. 1. In: Proceedings, 48th Workshop on Geothermal Reservoir Engineering, Volume SGP -TR-224. Stanford CA, Stanford University, p. 13.

Fulton, P., Clairmont, R., Fulcher, S., Pinilla, D., Purwamaska, I., Fresonke, M., Puthur, R., Torres, J., Heaton, T., Beckers, K., Beyers, S., Bezner-Kerr, W., Bland, R., Erdinc, B., Gustafson, O., Jordan, T., Tester, J., 2024. Subsurface insights from the Cornell University Borehole Observatory (CUBO): a 3km deep exploratory well for advancing Earth Source Heat deep direct-use geothermal for district heating. In: Proceedings, 49th Workshop on Geothermal Reservoir Engineering Volume SGP-TR-227. Stanford University, Stanford, California, Stanford University, p. 12.

Gale, J.F.W., Elliott, S.J., Rysak, B.G., Laubach, S.E., 2023. The Critical Role of Core in Understanding Hydraulic Fracturing, Core Values: the Role of Core in Twenty-first Century Reservoir Characterization. Geological Society of London, pp. 317–332.

Gale, J.F.W., Gomez, L.A., 2007. Late opening-mode fractures in karst-brecciated dolostones of the Lower Ordovician Ellenburger Group, west Texas: recognition, characterization, and implications for fluid flow. AAPG Bull. 91 (7), 1005–1023. https://doi.org/10.1306/03130706066.

Gee, B., Gracie, R., Dusseault, M.B., 2021. Multiscale short-circuiting mechanisms in multiple fracture enhanced geothermal systems. Geothermics 94, 102094. https://doi.org/10.1016/j.geothermics.2021.102094.

Ghassemi, A., 2012. A review of some rock mechanics issues in geothermal reservoir development. Geotech. Geol. Eng. 30 (3), 647–664. https://doi.org/10.1007/s10706-012-9508-3.

Gillespie, P.A., Holdsworth, R.E., Long, D., Williams, A., Gutmanis, J.C., 2021. Introduction: geology of fractured reservoirs. J. Geol. Soc. 178 (2). https://doi.org/10.1144/jgs2020-197 jgs2020-2197.

Gomez, L., Gale, J., Laubach, S., Cumella, S., 2003. Chapter 6, Quantifying Fracture Intensity: an Example from the Piceance Basin: Piceance Basin 2003 Guidebook, pp. 96–113.

Gomez, L.A., Laubach, S.E., 2006. Rapid digital quantification of microfracture populations. J. Struct. Geol. 28 (3), 408–420. https://doi.org/10.1016/J.JSG.2005.12.006.

Götze, J., Plötze, M., Habermann, D., 2001. Cathodoluminescence (CL) of quartz: origin, spectral characteristics and practical applications. Miner. Pet.: Mineral. Petrol. 71, 225–250. https://doi.org/10.1007/s007100170040.

Gutmanis, J., Ardèvol i Oró, L., Díez-Canseco, D., Chebbihi, L., Awdal, A., Cook, A., 2018. Fracture analysis of outcrop analogues to support modelling of the subseismic domain in carbonate reservoirs, south-central Pyrenees. Geol. Soc. Lond. 459 (1), 139–156. https://doi.org/10.1144/SP459.2. Special Publications.

Hancock, P.L., 1985. Brittle microtectonics: principles and practice. J. Struct. Geol. 7 (3), 437–457. https://doi.org/10.1016/0191-8141(85)90048-3.

Hansen, D. K., and Enderlin, M. B., 1991, Petrophysical significance of oriented sidewall cores for improved reservoir characterization: advances in core evaluation II-reservoir appraisal, p. 135-144.

Hati, S., Chawla, H., Ghosh, A., Guru, U., Guru, R., 2021. Identifying producing horizons in fractured reservoirs a far field acoustic approach. In: SPE Middle East Oil & Gas Show and Conference. D021S011R007.

Heidbach, O., Rajabi, M., Reiter, K., Ziegler, M.O., 2019. World Stress Map. In: Sorkhabi, R. (Ed.), Encyclopedia of Petroleum Geoscience. Springer International Publishing, Cham, pp. 1–8.

Hickman, S.H., Healy, J.H., Zoback, M.D., 1985. In situ stress, natural fracture distribution, and borehole elongation in the Auburn Geothermal Well, Auburn, New York. J. Geophys. Res.: Solid Earth 90 (B7), 5497–5512. https://doi.org/10.1029/JB090iB07p05497.

Hillis, R.R., 1998. The influence of fracture stiffness and the in situ stress field on the closure of natural fractures. Pet. Geosci. 4 (1), 57–65. https://doi.org/10.1144/petgeo.4.1.57.

Holdsworth, R.E., Trice, R., Hardman, K., McCaffrey, K.J.W., Morton, A., Frei, D., Dempsey, E., Bird, A., Rogers, S., 2020. The nature and age of basement host rocks and fissure fills in the Lancaster field fractured reservoir, West of Shetland. J. Geol. Soc. 177 (5), 1057–1073. https://doi.org/10.1144/jgs2019-142.

Hooker, J.N., Gale, J.F.W., Gomez, L.A., Laubach, S.E., Marrett, R., Reed, R.M., 2009. Aperture-size scaling variations in a low-strain opening-mode fracture set, Cozzette Sandstone, Colorado. J. Struct. Geol. 31 (7), 707–718. https://doi.org/10.1016/j.jsg.2009.04.001.

Hooker, J.N., Laubach, S.E., Gomez, L., Marrett, R., Eichhubl, P., Diaz-Tushman, K., Pinzon, E., 2011. Fracture size, frequency, and strain in the Cambrian Eriboll

Formation sandstones, NW Scotland. Scott. J. Geol. 47 (1), 45–56. https://doi.org/10.1144/0036-9276/01-420.
Hooker, J.N., Laubach, S.E., Marrett, R., 2013. Fracture-aperture size—frequency, spatial distribution, and growth processes in strata-bounded and non-strata-bounded fractures, Cambrian Mesón Group. NW Argent.: J. Struct. Geol. 54, 54–71. https://doi.org/10.1016/j.jsg.2013.06.011.
Hooker, J.N., Laubach, S.E., Marrett, R., 2014. A universal power-law scaling exponent for fracture apertures in sandstones. GSA Bull. 126 (9-10), 1340–1362. https://doi.org/10.1130/B30945.1.
Hooker, J.N., Laubach, S.E., Marrett, R., 2018. Microfracture spacing distributions and the evolution of fracture patterns in sandstones. J. Struct. Geol. 108, 66–79. https://doi.org/10.1016/j.jsg.2017.04.001.
Hooker, J.N., Marrett, R., Wang, Q., 2023. Rigorizing the use of the coefficient of variation to diagnose fracture periodicity and clustering. J. Struct. Geol. 168, 104830. https://doi.org/10.1016/j.jsg.2023.104830.
Hornby, B.E., Luthi, S.M., Plumb, R.A., 1992. Comparison of fracture apertures computed from electrical borehole scans and reflected Stoneley waves: an integrated interpretation. Log Anal. 33 (01).
Horton, J. D., San Juan, C. A., and Stoeser, D. B., 2017, The state geologic map compilation (SGMC) geodatabase of the conterminous United States, 1052. p. 56-56.
Hsu, K., Brie, A., Plumb, R.A., 1987. A new method for fracture identification using array sonic tools. J. Pet. Technol. 39 (06), 677–683. https://doi.org/10.2118/14397-PA.
Isachsen, Y., Landing, E., Lauber, J., Rickard, L., Rogers, W., 2000. Geology of New York. A Simplified Account, Second Edition.
Jacobi, R.D., 2002. Basement faults and seismicity in the Appalachian Basin of New York State. Tectonophysics 353 (1), 75–113. https://doi.org/10.1016/S0040-1951(02)00278-0.
Ji, S., Zhao, P., Saruwatari, K., 1997. Fracturing of garnet crystals in anisotropic metamorphic rocks during uplift. J. Struct. Geol. 19 (5), 603–620. https://doi.org/10.1016/S0191-8141(97)00006-0.
Jin, G., Ning, Y., Gale, M., Simmons, J., Tura, A., 2024. Impact of natural fractures on hydraulic fracture propagation in Denver-Julesburg Basin: Insights from a decade of research. Lead. Edge 43 (12), 806–814. https://doi.org/10.1190/tle43120806.1.
Jones, C., Simmons, S., Moore, J., 2024. Geology of the Utah Frontier Observatory for Research in Geothermal Energy (FORGE) Enhanced Geothermal System (EGS) site. Geothermics 122, 103054. https://doi.org/10.1016/j.geothermics.2024.103054.
Jordan, T., Camp, E., Smith, J., Whealton, C., Horowitz, F.G., Stedinger, J.R., Tester, J. W., Richards, M., Frone, Z., Bolat, R., Hornbach, M., Chickering Pace, C., Magnani, B., Anderson, B., He, X., Welcker, K., 2016. Low-temperature geothermal play fairway analysis for the Appalachian Basin. In: Proceedings, 41st Workshop on Geothermal Reservoir Engineering, Volume SGP-TR-209. Stanford Univeristy.
Jordan, T., Fulton, P., Tester, J., Bruhn, D., Asanuma, H., Harms, U., Wang, C., Schmitt, D., Vardon, P.J., Hofmann, H., Pasquini, T., Smith, J., the workshop, p., 2020. Borehole research in New York State can advance utilization of low-enthalpy geothermal energy, management of potential risks, and understanding of deep sedimentary and crystalline geologic systems. Sci. Dril. 28, 75–91. https://doi.org/10.5194/sd-28-75-2020.
Kimball, C.V., Endo, T., 1998. Quantitative Stoneley mobility inversion. In: 1998 SEG Annual Meeting. SEG-1998-0252.
Koepf, E.H., Granberry, R.J., 1961. The use of sidewall core analysis in formation evaluation. J. Pet. Technol. 13 (05), 419–424. https://doi.org/10.2118/1635-G-PA.
Kolkas, M.M., Friedman, G.M., 1999. Regional stratigraphy, facies distribution, and depositional environments of the Beekmantown Group (Sauk Sequence of Central and Western New York. Northeast. Geol. Environ. Sci. 21 (4), 247–260.
Kolkas, M.M., Friedman, G.M., 2007. Brine disposal in deep geologic formations of the Cambro-Ordovician (Sauk Sequence) of New York: implications for new salt-caverngas-storage reservoirs. Northeast. Geol. Environ. Sci. 29 (2), 122–136.
Kostek, S., Johnson, D.L., Randall, C.J., 1998. The interaction of tube waves with borehole fractures, Part I: numerical models. Geophysics 63 (3), 800–808. https://doi.org/10.1190/1.1444391.
Kulander, B.R., Dean, S.L., Ward, B.J., 1990. Fractured Core Analysis: Interpretation, Logging, and Use of Natural and Induced Fractures in Core. American Association of Petroleum Geologists.
Lander, R.H., Laubach, S.E., 2015. Insights into rates of fracture growth and sealing from a model for quartz cementation in fractured sandstones. GSA Bull. 127 (3-4), 516–538. https://doi.org/10.1130/B31092.1.
Landing, E., 2007. Ediacaran–Ordovician of east Laurentia—geologic setting and controls on deposition along the New York promontory region. In: Landing, E. (Ed.), New York State Museum Bulletin 510. New York State Museum, pp. 5–24.
Landing, E., Amati, L., Franzi, D.A., 2009. Epeirogenic transgression near a triple junction: the oldest (latest early–middle Cambrian) marine onlap of cratonic New York and Quebec. Geol. Mag. 146 (4), 552–566. https://doi.org/10.1017/S0016756809006013.
Lash, G.G., Engelder, T., 2009. Tracking the burial and tectonic history of Devonian shale of the Appalachian Basin by analysis of joint intersection style. GSA Bull. 121 (1-2), 265–277. https://doi.org/10.1130/B26287.1.
Laubach, S., 2003. Practical approaches to identifying sealed and open fractures. AAPG Bull. 87, 561–579. https://doi.org/10.1306/11060201106.
Laubach, S., Marrett, R., Olson, J., 2000. New directions in fracture characterization. Lead. Edge 19 (7), 704–711. https://doi.org/10.1190/1.1438694.
Laubach, S.E., 1997. A method to detect natural fracture strike in sandstones. AAPG Bull. 81 (4), 604–623. https://doi.org/10.1306/522B43E3-1727-11D7-8645000102C1865D.
Laubach, S.E., Diaz-Tushman, K., 2009. Laurentian palaeostress trajectories and ephemeral fracture permeability, Cambrian Eriboll Formation sandstones west of the Moine Thrust Zone, NW Scotland. J. Geol. Soc. 166 (2), 349–362. https://doi.org/10.1144/0016-76492008-061.
Laubach, S.E., Doherty, E., 1999. Oriented drilled sidewall cores for natural fracture evaluation. In: SPE Annual Technical Conference and Exhibition, SPE-56801-MS.
Laubach, S.E., Gale, J.F.W., 2006. Obtaining fracture information for low permeability (tight) gas sandstones from sidewall cores. J. Pet. Geol. 29 (2), 147–158. https://doi.org/10.1111/j.1747-5457.2006.00147.x.
Laubach, S.E., Lander, R.H., Criscenti, L.J., Anovitz, L.M., Urai, J.L., Pollyea, R.M., Hooker, J.N., Narr, W., Evans, M.A., Kerisit, S.N., Olson, J.E., Dewers, T., Fisher, D., Bodnar, R., Evans, B., Dove, P., Bonnell, L.M., Marder, M.P., Pyrak-Nolte, L., 2019. The role of chemistry in fracture pattern development and opportunities to advance interpretations of geological materials. Rev. Geophys. 57 (3), 1065–1111. https://doi.org/10.1029/2019RG000671.
Laubach, S.E., Olson, J.E., Gale, J.F.W., 2004. Are open fractures necessarily aligned with maximum horizontal stress? Earth Planet. Sci. Lett. 222 (1), 191–195. https://doi.org/10.1016/j.epsl.2004.02.019.
Laubach, S.E., Reed, R.M., Gale, J.F., Ortega, O.J., Doherty, E.H., 2002. Fracture Characterization Based on Microfracture Surrogates. Gulf Coast Association of Geological Societies Transactions, Pottsville Sandstone, Black Warrior basin, Alabama, pp. 585–596, 52.
Lehne, K.A., Altunbay, M., Kelder, O., Geerits, T.W., Tang, X.M., 1999. Comparison between Stoneley, NMR and core-derived permeabilities. In: SPWLA 40th Annual Logging Symposium. SPWLA-1999-TT.
Li, L., Ji, S., 2021. A new interpretation for formation of orthogonal joints in quartz sandstone. J. Rock Mech. Geotech. Eng. 13 (2), 289–299. https://doi.org/10.1016/J.JRMGE.2020.08.003.
Limberger, J., Boxem, T., Pluymaekers, M., Bruhn, D., Manzella, A., Calcagno, P., Beekman, F., Cloetingh, S., van Wees, J.-D., 2018. Geothermal energy in deep aquifers: A global assessment of the resource base for direct heat utilization. Renew. Sustain. Energy Rev. 82, 961–975. https://doi.org/10.1016/j.rser.2017.09.084.
Liu, Z., Wu, M., Zhou, H., Chen, L., Wang, X., 2024. Performance evaluation of enhanced geothermal systems with intermittent thermal extraction for sustainable energy production. J. Clean. Prod. 434, 139954. https://doi.org/10.1016/j.jclepro.2023.139954.
Lloyd, G.E., Knipe, R.J., 1992. Deformation mechanisms accommodating faulting of quartzite under upper crustal conditions. J. Struct. Geol. 14 (2), 127–143. https://doi.org/10.1016/0191-8141(92)90052-X.
Lowe, D., Brink, R., Mehrtens, C., 2015. Sedimentology and Stratigraphy of the Cambrian-Ordovician Potsdam Group (Altona, Ausable and Keeseville Formations). Northwestern NY (Field Trip D-2).
Lowe, D.G., Arnott, R.W.C., Nowlan, G.S., McCracken, A.D., 2017. Lithostratigraphic and allostratigraphic framework of the Cambrian–Ordovician Potsdam Group and correlations across Early Paleozoic southern Laurentia. Can. J. Earth Sci. 54 (5), 550–585. https://doi.org/10.1139/cjes-2016-0151.
Lynch, R. S., and Castor, T. P., 1983, Auburn low-temperature geothermal well. Volume 6. Final report.
Majoribanks, R., 2002. Handbook 5: Structural Logging of Drill Core. The Australian Institute of Geoscientists, Australia.
Marrett, R., Gale, J.F.W., Gómez, L.A., Laubach, S.E., 2018. Correlation analysis of fracture arrangement in space. J. Struct. Geol. 108, 16–33. https://doi.org/10.1016/J.JSG.2017.06.012.
Marrett, R., Ortega, O.J., Kelsey, C.M., 1999. Extent of power-law scaling for natural fractures in rock. Geology 27 (9), 799–802. https://doi.org/10.1130/0091-7613(1999)027<0799:EOPLSF>2.3.CO;2.
McGinnis, R.N., Ferrill, D.A., Morris, A.P., Smart, K.J., Lehrmann, D., 2017. Mechanical stratigraphic controls on natural fracture spacing and penetration. J. Struct. Geol. 95, 160–170. https://doi.org/10.1016/j.jsg.2017.01.001.
Meng, L., Li, T., 2013. Experimental study on the permeability of phyllite under unloading confining pressure and high temperature. Disaster Adv. 6 (2), 31–38.
Ministère des Ressources naturelles et des Forêts, 2024. In: SIGÉOM (Ed.), Bedrock Geology. Montreal, Quebec.
Morris, R.L., Grine, D.R., Arkfeld, T.E., 1964. Using compressional and chear acoustic amplitudes for the location of fractures. J. Pet. Technol. 16 (06), 623–632. https://doi.org/10.2118/723-PA.
Moska, R., Labus, K., Kasza, P., 2021. Hydraulic fracturing in enhanced geothermal systems—field, tectonic and rock mechanics conditions—a review. Energies 14 (18), 1–24. https://doi.org/10.3390/en14185725.
Mount, V.S., 2014. Structural style of the Appalachian Plateau fold belt, north-central Pennsylvania. J. Struct. Geol. 69, 284–303. https://doi.org/10.1016/j.jsg.2014.04.005.
Neal, A., James, A., Payne, D., Ashton, M., van den Beukel, N., Storer, D., 2023. Integrated borehole image and rotary sidewall core data to support infrastructure-led appraisal: Capercaillie Field, Central North Sea. Geol. Soc. Lond. Spec. Publ. 527 (1), 225–260. https://doi.org/10.1144/SP527-2022-184.
Nelson, E.J., Meyer, J.J., Hillis, R.R., Mildren, S.D., 2005. Transverse drilling-induced tensile fractures in the West Tuna area, Gippsland Basin, Australia: implications for the in situ stress regime. Int. J. Rock Mech. Min. Sci. 42 (3), 361–371. https://doi.org/10.1016/j.ijrmms.2004.12.001.
Nelson, R.A., 1982. An approach to evaluating fractured reservoirs. J. Pet. Technol. 34 (09), 2167–2170. https://doi.org/10.2118/10331-PA.
Nogales, V., 2024. Geochemical, Mineralogical, and Petrophysical Characterization of the Potsdam-Precambrian basement unconformity Intersected by the CUBO Geothermal Exploration Borehole [MSc. Monograph]. Cornell University, p. 179.
O'Brien, T.M., van der Pluijm, B.A., 2012. Timing of Iapetus Ocean rifting from Ar geochronology of pseudotachylytes in the St. Lawrence rift system of southern Quebec. Geology 40 (5), 443–446. https://doi.org/10.1130/G32691.1.

Olson, J.E., Laubach, S.E., Lander, R.H., 2007. Combining diagenesis and mechanics to quantify fracture aperture distributions and fracture pattern permeability. Geol. Soc. Lond. 270 (1), 101–116. https://doi.org/10.1144/GSL.SP.2007.270.01.08. Special Publications.

Olson, J.E., Laubach, S.E., Lander, R.H., 2009. Natural fracture characterization in tight gas sandstones: integrating mechanics and diagenesis. AAPG Bull. 93 (11), 1535–1549. https://doi.org/10.1306/08110909100.

Ontario Geological Survey, 2024. 1:250 000 Scale Bedrock Geology of Ontario in Survey, O. G., ed. Ontario, Canada, OGS.

Ortega, O.J., Marrett, R.A., Laubach, S.E., 2006. A scale-independent approach to fracture intensity and average spacing measurement. Am. Assoc. Pet. Geol. Bull. 90 (2), 193–208. https://doi.org/10.1306/08250505059.

Parker, J.M., 1942. Regional systematic jointing in slightly deformed sedimentary rocks. GSA Bull. 53 (3), 381–408. https://doi.org/10.1130/GSAB-53-381.

Pinilla, D., Fulton, P., Jordan, T., 2023. Preliminary determination of in-situ stress orientation and magnitude at the Cornell University Borehole Observatory (CUBO) geothermal well, Ithaca NY. In: Proceedings, 48th Workshop on Geothermal Reservoir Engineering, Volume SGP-TR-224. Stanford, California, pp. 1–9.

Plumb, R.A., Hickman, S.H., 1985. Stress-induced borehole elongation: a comparison between the four-arm dipmeter and the borehole televiewer in the Auburn Geothermal Well. J. Geophys. Res.: Solid Earth 90 (B7), 5513–5521. https://doi.org/10.1029/JB090iB07p05513.

Procter, A., Sanderson, D.J., 2018. Spatial and layer-controlled variability in fracture networks. J. Struct. Geol. 108, 52–65. https://doi.org/10.1016/j.jsg.2017.07.008.

Pyrak-Nolte, L.J., DePaolo, D.J., Pietraß, T., 2015. Controlling Subsurface Fractures and Fluid Flow: A Basic Research Agenda. U.S. DOE, p. 23.

Rangel-Jurado, N., Hawkins, A.J., Fulton, P.M., 2023. Influence of extreme fracture flow channels on the thermal performance of open-loop geothermal systems at commercial scale. Geotherm. Energy 11 (1), 19. https://doi.org/10.1186/s40517-023-00261-7.

Repetski, J., Ryder, R., Weary, D., Harris, A., and Trippi, M., 2008, Thermal maturity patterns (CAI and %Ro) in upper Ordovician and Devonian rocks of the Appalachian Basin: a major revision of USGS Map I-917-E using new subsurface collections.

Rives, T., Razack, M., Petit, J.P., Rawnsley, K.D., 1992. Joint spacing: analogue and numerical simulations. J. Struct. Geol. 14 (8), 925–937. https://doi.org/10.1016/0191-8141(92)90024-Q.

Robinson, P., Tucker, R.D., Bradley, D., Berry Iv, H.N., Osberg, P.H., 1998. Paleozoic orogens in New England, USA. GFF 120 (2), 119–148. https://doi.org/10.1080/11035899801202119.

Rourke, M., and Torne, J., 2011, A new wireline rotary coring tool: development overview and experience from the Middle East, SPE/DGS Saudi Arabia Section Technical Symposium and Exhibition, p. SPE-149128-MS.

Sanderson David, J., 2016. Field-based structural studies as analogues to sub-surface reservoirs. Geol. Soc. Lond. 436 (1), 207–217. https://doi.org/10.1144/SP436.5. Special Publications.

Sanderson, D.J., Nixon, C.W., 2015. The use of topology in fracture network characterization. J. Struct. Geol. 72, 55–66. https://doi.org/10.1016/j.jsg.2015.01.005.

Sanford, B.V., Arnott, R.W.C., 2010. Stratigraphic framework of the Potsdam Group in eastern Ontario, western Quebec, and northern New York State. Abstr. Vol. (Geol. Assoc. Can.) 34, 193–194.

Sasseville, C., Clauer, N., Tremblay, A., 2012. Timing of fault reactivation in the upper crust of the St. Lawrence rift system, Canada, by K–Ar dating of illite-rich fault rocks1GEOTOP Contribution 2012-0002. Can. J. Earth Sci. 49 (5), 637–652. https://doi.org/10.1139/e2012-008.

Saucier, D., Sincock, K., 2023. An operator view on trends in core acquisition. Geol. Soc. Lond. 527 (1), 17–42. https://doi.org/10.1144/SP527-2022-62. Special Publications.

Schlumberger, 2004. GPIT General Purpose Inclinometry Tool. Schlumberger, Houston, TX, Schlumberger, p. 2. Volume FE_04_022_0.

Scott, P.A., 1986. A Kinematic Analysis of Appalachian Plateau Deformation at Portland Point, Tompkins County, central New York [BSc. Cornell University, p. 36.

Sheldon, P., 1912. Some observations and experiments on joint planes. J. Geol. 20 (1), 53–79.

Shorten, C.M., Fitzgerald, P.G., 2019. Post-orogenic thermal history and exhumation of the northern Appalachian Basin: low-temperature thermochronologic constraints. Basin Res. 31 (6), 1017–1039. https://doi.org/10.1111/bre.12354.

Smith, J.D., 2019. Exploratory Spatial Data Analysis and Uncertainty Propagation for Geothermal Resource Assessment and Reservoir modelsPh.D.]. Cornell University, p. 276.

Smith, L., Nyahay, R., Slater, B., 2010. Integrated reservoir characterization of the subsurface Cambrian and Lower Ordovician Potsdam, Galway and Theresa Formations in New York. NYSERDA 69.

Stumpf, A., Damico, J., okwen, r., Stark, T., Elrick, S., Nelson, W.J., Lu, Y., Holcomb, F., Tinjum, J., Yang, F., Frailey, S., Lin, Y.-F., 2018. Sponsor Org.: USDOE Office of Energy Efficiency and Renewable Energy (EERE), Renewable Power Office. Geothermal Technologies Office, Feasibility of a deep direct-use geothermal system at the University of Illinois Urbana-Champaign. In: Proceedings GRC Transactions, United States. IL (United States), 13. Research Org.: Univ. of Illinois at Urbana-Champaign. Volume 42.

Taylor, T.R., Lander, R.H., Bonnell, L.M., 2022. Sandstone Petrography, Petrology, and Modeling. SEPM Society for Sedimentary Geology.

Tester, J., Gustafson, O., Fulton, P., Jordan, T., Beckers, K., Beyers, S., 2023. Geothermal direct use for decarbonization — progress towards demonstrating Earth Source Heat at Cornell. In: Proceedings, 48th Workshop on Geothermal Reservoir Engineering, Volume SGP-TR-224. Stanford University, p. 17.

Tremblay, A., Roden-Tice, M.K., Brandt, J.A., Megan, T.W., 2013. Mesozoic fault reactivation along the St. Lawrence rift system, eastern Canada: thermochronologic evidence from apatite fission-track dating. GSA Bull. 125 (5-6), 794–810. https://doi.org/10.1130/B30703.1.

Ukar, E., Laubach, S.E., Hooker, J.N., 2019. Outcrops as guides to subsurface natural fractures: example from the Nikanassin formation tight-gas sandstone, Grande Cache, Alberta foothills, Canada. Mar. Pet. Geol. 103, 255–275. https://doi.org/10.1016/j.marpetgeo.2019.01.039.

Valentino, D.W., Chiarenzelli, J.R., Jordan, T.E., Jacobi, R.D., Gates, A.E., 2024. Deep borehole discoveries beneath the Appalachian Basin: broad Rodinian rift and Neoproterozoic tectonothermal event. Terra Nova 37 (1), 1–7. https://doi.org/10.1111/ter.12741.

Volonté, G., Bersani, A., Berto, R., Cerri, R., Pinelli, F., 2023. Integrated workflow for rotary sidewall cores orientation: best practices and examples from planning to execution. In: E3S Web of Conferences, 366, 01012. https://doi.org/10.1051/e3sconf/202336601012.

Wang, Q., Laubach, S.E., Gale, J.F.W., Ramos, M.J., 2019. Quantified fracture (joint) clustering in Archean basement, Wyoming: application of the normalized correlation count method. Pet. Geosci. 25 (4), 415–428. https://doi.org/10.1144/PETGEO2018-146.

Wedel, A.A., 1932. Geologic structure of the Devonian strata of south-central New York. N. Y. State Mus. Bull. 294, 1–74.

Wennberg, O.P., De Oliveira Ramalho, F., Virgolino Mafia, M., Lapponi, F., Chandler, A. S., Gomis Cartesio, L.E., Hunt, D.W., 2023. The characteristics of natural open fractures in acoustic borehole image logs from the pre-salt Barra Velha formation, Santos Basin, Brazil. J. Struct. Geol. 167, 104794. https://doi.org/10.1016/j.jsg.2023.104794.

Wolff, R. G., 1982, Physical properties of rocks; porosity, permeability, distribution coefficients, and dispersivity, 82-166.

Zenger, D.H., 1976. Definition of type Little Falls dolostone (Late Cambrian), east-central New York: geologic notes. AAPG Bull. 60 (9), 1570–1575. https://doi.org/10.1306/c1ea38ac-16c9-11d7-8645000102c1865d.

Zhang, J., Lang, J., Standifird, W., 2009. Stress, porosity, and failure-dependent compressional and shear velocity ratio and its application to wellbore stability. J. Pet. Sci. Eng. 69 (3), 193–202. https://doi.org/10.1016/j.petrol.2009.08.012.